TWO DIMENSIONAL (SOLID PHASE) KINETIC ANALYSIS OF FÇ̣GAMMA RECEPTOR III (CD16) INTERACTION WITH IgG

A Dissertation
Presented To
The Academic Faculty

By

Scott Edward Chesla

In Partial Fulfillment
Of the Requirements for the Degree
Doctor of Philosophy in Mechanical Engineering

Georgia Institute of Technology

August, 2005

TWO DIMENSIONAL (SOLID PHASE) KINETIC ANALYSIS OF FÇGAMMA RECEPTOR III (CD16) INTERACTION WITH IgG

Approved by:

Dr. Cheng Zhu, Advisor
School of Bioengineering and Mechanical Engineering
Georgia Institute of Technology

Dr. Periasamy Selvaraj
School of Medicine
Emory University

Dr. Robert Nerem
School of Mechanical Engineering
Georgia Institute of Technology

Dr. Raymond Vito
School of Mechanical Engineering
Georgia Institute of Technology

Dr. Timothy Wick
School of Chemical Engineering
Georgia Institute of Technology

Dr. Lyle Sinor
Immucor, Inc.

Date Approved: January 26, 2005

If you can’t model it, you don’t understand it.

For E.J. Chesla, Jr. and I. C. Chesla

ACKNOWLEDGEMENTS

I would like to thank all my lab coworkers, my advisors, Dr. Zhu, Dr. Selvaraj, everyone at the Georgia Tech Woodruff School of Mechanical Engineering and Coulter Department of Bioengineering, and everyone at the Emory School of Medicine for their advise, understanding, patience and encouragement.

TABLE OF CONTENTS

LIST OF TABLES

LIST OF FIGURES

LIST OF ABREVIATIONS

CCD	charge coupled device
CD16	FcγRIII
CD32	FcγRII;
CD64	FcγRI
CD16a-γ	CD16a γ subunit chimera;
CD16a-ζ	CD16a ζ subunit chimera
CHO	Chinese hamster ovary
CLBFcgran1	anti- CD16 antibody
DNP	2,4-dinitrophenyl
E	erythrocytes
EA	antibody- or IgG-opsonized erythrocytes
ELISA	enzyme-linked immunosorbent assay
FBS	fetal bovine serum
Fε RI	Fcε receptor
FcγR	Fcγ receptor
FcγRIII	Fc γ receptor III
FITC	fluorescein isothiocyanate
GPI	glycosyl phosphatidylinositol
h	human
HBSS	Hanks' balanced salt solution
IC	immune complex(es)
IgG	
mAb	monoclonal antibody
m	murine
NA	neutrophil alloantigen
NA1 and NA2,	neutrophil antigen 1 and 2
NK	natural killer
PAGE	polyacrylamide gel electrophoresis
PBS	phosphate-buffered saline
PIPLC	phosphatidylinositol-specific phospholipase C
Rb	rabbit
SE	sheep erythrocytes
TM	transmembrane
TNP	trinitrophenyl
X63	non-specific antibody
3G8	anti- CD16 antibody
IV.3	anti- CD32 antibody

SUMMARY

Cellular adhesion research has recently focused on the small scale at the level of individual receptor-ligand bonds. This trend in research is primarily due to experimental advances which allow such individual bond force measurements. Here, one of these techniques, micromanipulation, has been extended to not only determine the bond force of individual receptor-ligand pairs, but also the intrinsic kinetic rates of the interaction. Using transmembrane (TM) Fc gamma receptor III (CD16a-TM) and human IgG (hIgG), the dependence of adhesion probability on receptor-ligand expression densities, contract duration and contact area was quantitated. A probabilistic based theoretical formulation was developed and validated that relates the intrinsic molecular kinetic rates of the receptor–ligand interaction to the experimentally determined adhesion probability. This theoretical formulation describing individual receptor-ligand kinetics has also allowed direct evaluation of existing biophysical bond strength/kinetics paradigms at the extreme condition of single bonds. A force-displacement model was also developed to quantitate the force exerted on the RBC membrane transducer during the micropipette retraction process and found to be in agreement with previous work.

In addition to CD16a-TM, the kinetic rates of CD16a anchored via a glycosyl phosphatidylinositol (GPI) moiety (CD16a-GPI) and the two alleles of CD16b (NA1 and NA2) were determined for human, rabbit, and mouse IgG species. The binding affinity of these CD16 interactions to soluble IgG was also measured by traditional bulk chemistry approaches and compared to those measured via the micromanipulation protocol in which the IgG ligand is membrane bound in the solid phase. These data suggest that the membrane anchor itself can alter CD16 binding properties. This represents the first

reported effect of the anchor on an intrinsic receptor property, its kinetic rates and binding affinity.

This thesis presents two specific aims or goals. These goals were achieved and reported in this thesis. During the course of this research, I also explored other directions and gathered initial data. These directions were further explored by other researchers but the initial data is also presented here. The areas of this initial research include:

1. The elucidation of receptor / ligand orientation effects on solid phase affinity. The orientation of molecules on the surface was shown to affect the effective molecular densities and therefore the on-rate and affinity of the interaction.
2. Defining a method for the determination of detachment mode during bond decoupling. A bond can break either by up rooting of the receptor from the attached membrane or between the receptor and ligand pair. The defined method describes a procedure to quantify the portion of each mode of detachment.
3. The characterization of CD16a-TM and hIgG bond force histograms for evidence of stochastic or deterministic behavior.
4. The observation of CD16 mediated phagocytosis at the single cell level utilizing the micropipette system.

CHAPTER 1

GOALS, OBJECTIVES, SPECIFIC AIMS

The availability of isolated CD16 isoform cell lines and the micropipette experimental system for isolating cellular contact provide for the opportunistic exploration of small scale adhesion analysis. The availability of CD16 in the receptor / ligand model is fortunate. CD16 is natively expressed in three different isoforms. The effect of the different isoforms on binding is previously not known and with elucidation is directly relevant to biological processes. The CD16 ligand is the Fc portion of IgG. The use of IgG also permits the affinities of the adhesion components to be easily manipulated by altering the species of IgG used in the analysis. Using the CD16, IgG and micropipette system the specific goals and objectives of this work are as follows:

Develop A Method For The Determination Of Solid Phase Kinetic Properties Using The Micropipette Experimental System In Small Scale Adhesion.

Previous experiments utilizing micromanipulation with red blood cells (RBC) for the determination of bonding forces utilized antibody coated beads or crosslinking antibodies. The experiments reported here utilized a transfected Chinese Hamster Ovary (CHO) cell line expressing CD16 and a RBC expressing IgG. In order to examine small scale adhesion using the micropipette experimental system a theoretical framework must first be developed. Previous explorations into small scale adhesion focused mainly on the resolution of force. The determination of the solid phase kinetics of small scale binding will require a new model. This model will first be validated then it will be extended to predict the binding kinetics of CD16 to IgG and influence of different anchoring mechanisms employed by the receptor will be determined.

Explore The Differences In Solid Phase Kinetic Rates Of CD16 To Predict The Effect Of Anchoring Mechanism On These Extracellular Properties.

CD16 is one of only four eukaryotic receptors known to natively exist in both the transmembrane (TM, CD16a) and the glycosyl phosphatidylinositol (GPI, CD16b) isoforms. The biological significance of this anchor isoform coexistence is not clear. Here we report that kinetic rates vary with CD16 membrane isoforms with the differences being dependent on the IgG origin.

CHAPTER 2

BACKGROUND / LITERATURE

Agglutination Of Red Blood Cells

The forces that govern the cellular adhesion may be classified as nonspecific and specific. The nonspecific forces, colloidal forces, have been extensively studied by physicists. These forces include electrostatic, van der Waals, depletion, and hydration forces. In biology, an example of specific adhesion is the process of agglutination which describes the antibody mediated clumping of particles expressing a certain specific antigen. The clumping of red blood cells occurs because the antibody binds to the specific antigens presented on the membrane surface. The process of agglutination is chemical reaction that can be expressed in two steps. Step 1 involves the attachment of antibody to a cell surface. This is a solution based process (or 3 dimensional, 3D) because the unattached antibody is in solution before it attaches to the membrane bound antigen. The next step involves the solid phase process (or 2 dimensional, 2D) of binding both the membrane bound antibody (or receptor) with the membrane bound antigen (or ligand). Various factors affect both steps and can be manipulated to increase or decrease the rates of reaction.

Before agglutination can occur, the respective components must come together and form a suitable special relationship. As shown in Figure 2.1, the receptor and ligand must complement each other both structurally (stericly) and chemically. Forces that hold the receptor / ligand complex together are weak compared to a covalent bond and the complex is reversible, i.e., bonds are randomly forming and disassociating even after a state of equilibrium is achieved.

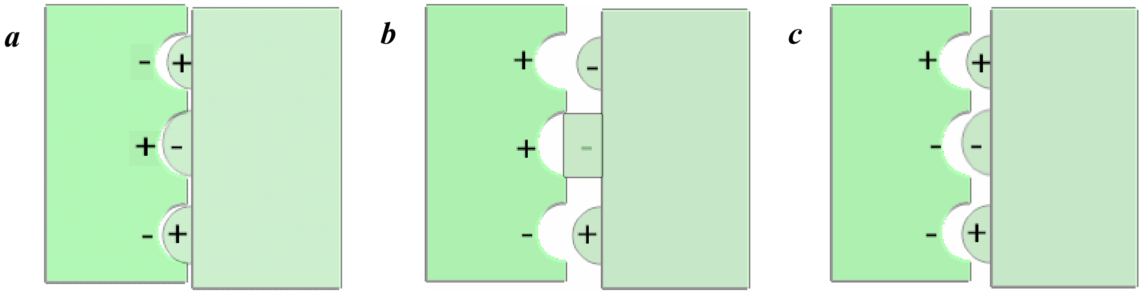

Figure 2.1: Receptor-Ligand goodness of fit. a) good structural fit with complimentary charge attraction, b) chemical groups are complementary but the structural fit is poor, c) good structural fit but the charge groupings are not attractive and may repel one another.

Mathematical models describing the phenomena of agglutination are usually derived as a combination of chemical kinetic and thermodynamic models. When receptor and ligand are brought into close proximity, the opportunity for bond formation between them (cell adhesion) is created. First, diffusion of the receptor and ligand must occur until both are within the range of interaction. Next, the receptor and ligand react to form a bond. This may be represented in the following two step reaction:

$$X+Y \underset{d-}{\overset{d+}{\rightleftarrows}} XY \underset{r-}{\overset{r+}{\rightleftarrows}} Z \tag{2-1}$$

where: X= receptor density

Y= ligand density

XY= receptor/ligand encounter complex

Z= bond density

$d_{+,-}$= rates of formation and dissolution of the complex

$r_{+,-}$= forward and reverse rate constants for bond formation

Under most occasions, the concentration of encounter complex is small and the condition $d[XY]/dt$ is satisfied, Bell (1978). The individual rates of complex and bond formation may then be combined into a single rate constant (then the overall affinity constant becomes $K_a = k_+ / k_-$)

The binding of specific receptors and ligands is the result of random collisions between the two that create binding opportunities. The physicochemical characteristics of simple receptor-ligand bonding are deterministically described by equation 2-1 assuming that there is one determinant per molecule (i.e. monomeric binding). When at least one of the molecules is in solution, the diffusional portion of the equation accounting for the formation of an encounter complex is so rapid that it is usually dropped from the relation. For a given concentration of receptor, the amount of complex formed will depend on the concentration of ligand and the strength of the binding interaction which is characterized by the reaction rate. Different parameters are known to affect the rate of binding interaction. The strength of the interaction is an intrinsic property of the receptor-ligand combination but is also a function of temperature and solvent conditions.

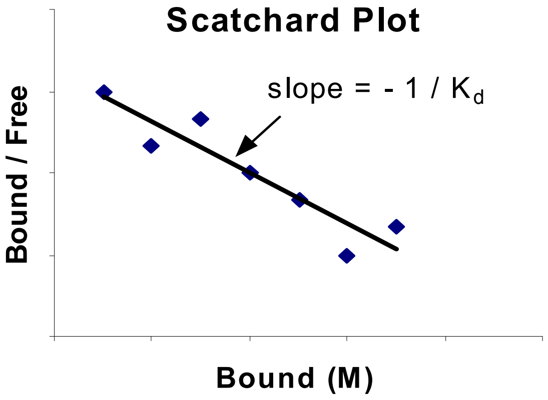

Figure 2.2: An example Scatchard plot.

At equilibrium the reaction can be characterized by the dissociation constant (K_d). The smaller the K_d, the greater the strength of molecular interaction and more complex is formed. The determination of binding affinity when one of the molecules is membrane bound is commonly measured using a Scatchard method. With this protocol, the free molecule is labeled with a quantifiable agent, usually ^{125}I. Cells expressing the receptor of interest are introduced to solute containing the labeled ligand and complex is formed on the cell surface. At equilibrium, the cells are isolated from the solute via centrifugation. The amount of quantifiable ligand on the cell surface is taken as the amount of complex formed and by titrating the concentration of free ligand in solution, a curve of complex versus complex / free ligand can be produced. For a bimolecular interaction, the slope of the linear fit of the data points is the negative reciprocal of the dissociation constant of the reaction as illustrated in Figure 2.2. Unfortunately, as the dissociation constant becomes large, the slope of the Scatchard plot approaches zero and an accurate determination of the reaction's binding affinity is difficult. Under this condition, an alternative protocol is usually utilized called competition binding. The protocols for competition binding are much less standardized than those of Scatchard analysis because the reaction is more complex. The particular form of competition binding utilized in this work is described in detail in the Materials And Methods section.

Macroscopic Models Of Cell Adhesion

The receptor-ligand properties that are significant in determining the strength of adhesion between two cells are the molecular density, the individual rate constants, the lateral mobility, and the mode of separation between a receptor and its ligand. The importance of these properties is easily rationalized by examination of the theoretical models of cell adhesion. Simple early models (Bell, (1979), Bell et al., (1984), Dembo et al., (1988), Dembo, (1994)) also predicted that cell adhesion strength is directly related to the number of bonds formed and in turn a function of receptor and ligand densities on the cell membranes. Accordingly, Evans (1985) proposed that adhesion strength is a direct function of the force required to break a single bond:

$$\frac{N_Z f_Z l_Z}{2} = \left(\frac{F_T}{A_C}\right)\frac{l_Z}{2} \tag{2-2}$$

where: N_Z is the bond density,

f_Z is the force required to break a single bond,

l_Z is the extent of stretch required to reach peak force,

F_T is the total force to complete cell separation, and

A_c is the contact area.

From equation (2-2), the greater the required force to break a single bond, the greater the total force to separate bound cells. Bell (1978) calculated the force to rapidly break a single CD16 - IgG type bond in the order of 1.2 pN per bond. Interestingly, the force calculated to uproot a receptor that is not anchored to the cytoskeleton was estimated at 1.0 pN per molecule which is the same order of magnitude.

The thermodynamic equilibrium model also serves to theoretically quantify which and how specific receptor properties effect adhesion strength. The thermodynamic model predicts the reversible adhesion energy density is dependent upon the natural logarithm of the binding affinity (Dembo, (1988)):

$$\gamma = k_B \theta N_X \ln\left\{1 + \frac{N_Y}{K_D}\right\} \tag{2-3}$$

where: k_B is Boltzmann's constant,

γ is the adhesion density (a measure of adhesion strength),

θ is the absolute temperature,

N is the number of receptors (X) or ligands (Y), and

K_D is the dissociation constant ($1/K_a$).

From equation 2-3, with a smaller the disassociation constant, a greater adhesion density can be expected. Bell (1978) predicted that the force to rapidly break a single bond could be calculated from the equation:

$$f_Z = 1.6 \, E_O / r_o \qquad (2\text{-}4)$$

where: r_o is the minimum interaction range (nm),

f_Z is the force to break a single bond (pN per bond), and

E_O is the free energy change on binding (eV).

For a typical CD16 - IgG bond, letting $E_o \sim 0.37$ eV ($K^s \sim 10^6\,M^{-1}$) and $r_o \sim 1$ nm, results in a force, f_Z, of 1.2 pN per bond. For a covalent bond a similar approach results in a force of 30 pN per bond. The force to uproot a receptor that is not anchored to the cytoskeleton is estimated at 1 pN per molecule. It is of interest to note again that the theoretical force to uproot a receptor and that to rapidly break a single bond are on the same order of magnitude.

Small Scale Probability Based Theories Of Cell Adhesion

Despite the obvious importance of kinetic rate constants to our understanding of various cell adhesion processes, not until recently have they been directly determinable experimentally. Although there are many methods of measuring receptor-ligand binding kinetics when at least one of the molecular species is in solution (i.e., three-dimensional kinetics or solution phase), none of these methods can be applied when the two molecules are bound to two apposed surfaces, as in the case of solid phase adhesion (i.e., two-dimensional kinetics or solid phase kinetics).

This inapplicability of these methods is due to the fact that they all require quantification of the concentration changes of the bound and free ligands with time. However, in cell adhesion assays one usually measures only the fraction of adherent or detached cells. Although there is no adhesive bond associated with a detached cell, the number of bonds on an adherent cell can vary from one up. The only published method for measuring the bond density using fluorescent labeling requires a 30-min incubation to allow lateral diffusion of the unbound molecules inside and outside of the contact area to reach the steady state, which is far longer than the kinetic transient time of many receptor-ligand interactions, including the ones studied in the present work. Therefore, only 2D binding affinity, not kinetic rates, can be measured by the method of Dustin et al. (1996). To the best of our knowledge, no other published method exists that allows direct measurement of the changes in the density of bonds with time when the receptor-ligand bonds are localized inside the contact area spanning a narrow gap between two cells or between a cell and a substrate surface.

Because of the inability to directly measure the time course of bond density, the kinetics of receptor-ligand binding has to be inferred from the changes in the fraction of adherent cells with time and its relation to the distribution of bonds among these cells. Kaplanski et al. (1993) were the first to employ this idea to measure adhesion kinetics. Previously, most of the published work on adhesion kinetics measurements used flow techniques. In the flow chamber, the kinetic rates were estimated by analyzing the probabilities of forming a durable adhesion per unit length of travel between a cell and the surface and of the duration of these adhesions. A problem inherent to the flow chamber method is the lack of ability to control the adhesion event. It is difficult to determine (let alone control) from a top view observation whether a moving cell is in transient contact (i.e., colliding) with the surface until it is arrested. Therefore, the measured adhesion probability per unit displacement is a lumped parameter. It depends not only on the fraction of contacts that yield adhesion (adhesion probability per contact), but also on the number of contacts per unit length of travel (collision frequency), as well as on the duration and area of each contact. None of these can be measured separately and independently in the flow chamber system. Moreover, the formation of the first bond (which requires capture of the rapidly moving cell from the flow) is very different from that of the subsequent bonds (which involves receptor-ligand binding between two surfaces with much less relative motion). In addition, the size of the contact area, the duration of the contact, and the force exerted on the contact cannot be controlled by the experimenter, and they are all variable rather than constant in the flow chamber system. These make the estimate of the forward rate constant from the measured adhesion probability per unit distance difficult. Determination of the reverse rate constant, in contrast, is much simpler, because it involves only measurements of the lifetime of durable adhesions.

Evans et. Al. (1991) introduced the idea of studying small scale adhesion using the micropipette system. In his experimental system, the process of bond assembly led to the formation of only a small number of discrete attachments as he controlled the density of the agglutinin (which he did not quantitate) and the contact area. He proposed, as others had before, that even for a single bond the probability of survival attenuates with the duration of the load and that bond survival time decreases as the load increases. In his work the failure of even one bond was treated as a continuous stochastic process dependent on the magnitude and duration of the applied separation force. The dissociation rate of the bond was proposed to be strongly dependent upon the mechanical force imposed on the bond. This was first proposed by Bell (1978) in the form:

$$k_r = k_r^O \exp\left(a F_T / k_B TC\right) \tag{2-5}$$

where k_r = the reverse rate constant and

the "o" superscript references the solution based determination,

a = the molecular range of interaction,

F_T = the total force exerted on the bonds,

k_B = the Boltzman constant,

T = temperature and

C = the number of receptor/ligand complexes.

While Evans ideas were not new, the concept of applying these adhesion principles to a small number of bonds or even a single bond using the micropipette system was fresh. The concept that the kinetics of a small number of bonds would obey Poisson statistics was also reiterated from Bell.

Pierres (1996) explored the concept of the determination of a lower limit to the rate of association between antibody coated spheres and antigen coated surfaces in a flow chamber environment. The lower limit for the association rate was speculated to be the contact duration time between the coated sphere and the antigen coated surface. This limit was in the order of 0.001 seconds. This work was an experimental continuation of the work of Cozens-Roberts et al. (1990).

Commercial Application Of Antibody Mediated Red Cell Adhesion

An application to any theoretical work is always desirable. The following describes a commercial test that utilizes red cell binding mediated by antibody-antigen binding. In fact, the purpose of the test is to determine whether specific antibody-antigen binding is present. In solid-phase indirect microplate techniques, a red cell coating across the bottom of a reaction well is created. The test serum containing possible anti-RBC IgG antibodies is added to the wells and allowed to react with the red cell monolayer. After which the wells are washed free of the unbound proteins (unbound antibody). The indicator for attached antibody is a centrifuged suspension of anti-IgG-coated red cells. The reaction is positive if the indicator cells adhere across the sides of the well, Figure 2.3. If they settle to the bottom, it demonstrates that no antigen-antibody reaction has occurred. This system represents a commercial product which depends heavily on solid phase IgG mediated red cell to red cell adhesion. The model of cellular adhesion presented in this work is applicable to this commercial test system with slight modification. This will be addressed in the recommendations for future work section.

a

Reaction Grades **Well Photographs**

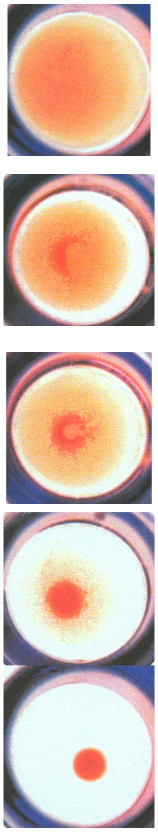

b

Procedure

Step 1: The solid phase antibody detection system described is based upon an antigen opsonized 96 well plate.

Step 2: A test sample is added to the well along with a binding potentiator.

Step 3: After an incubation period, the sample is washed from the well.

Step 4: An indicator cell sensitized with an anti-IgG antibody is added to the well and centrifuged.

Step 5: The indicator cell reaction is graded according the scale to the left.

Figure 2.3: The solid phase indirect antibody detection test is comprised of red blood cells which selectively express a desired antigen and are dried to the bottom of wells. Addition of a test sample allows for the formation of an antibody-antigen bond. After washing, adhered antibody is detected by the addition of anti-IgG coated red blood cells. These red cells are centrifuged to create a reaction pattern. (a) The possible reaction grades following centrifugation, ranging form strong positive to negative. (b) The solid phase testing procedure.

Antibody Molecules

IgG Structure

Isotypes of antibody are distinguished by certain effector functions and structural features including a unique heavy chain isotype. In man, the classes of antibodies are called IgA(α), IgD(δ), IgE(ε), IgG(γ), and IgM(μ). In some species, the immunoglobulin classes are further differentiated according to subclasses, adding another layer of complexity to antibody structure. In humans, for example, IgG antibodies comprise four IgG subclasses -- IgG1, IgG2, IgG3, and IgG4. A schematic of IgG structure is shown in Figure 2-4.

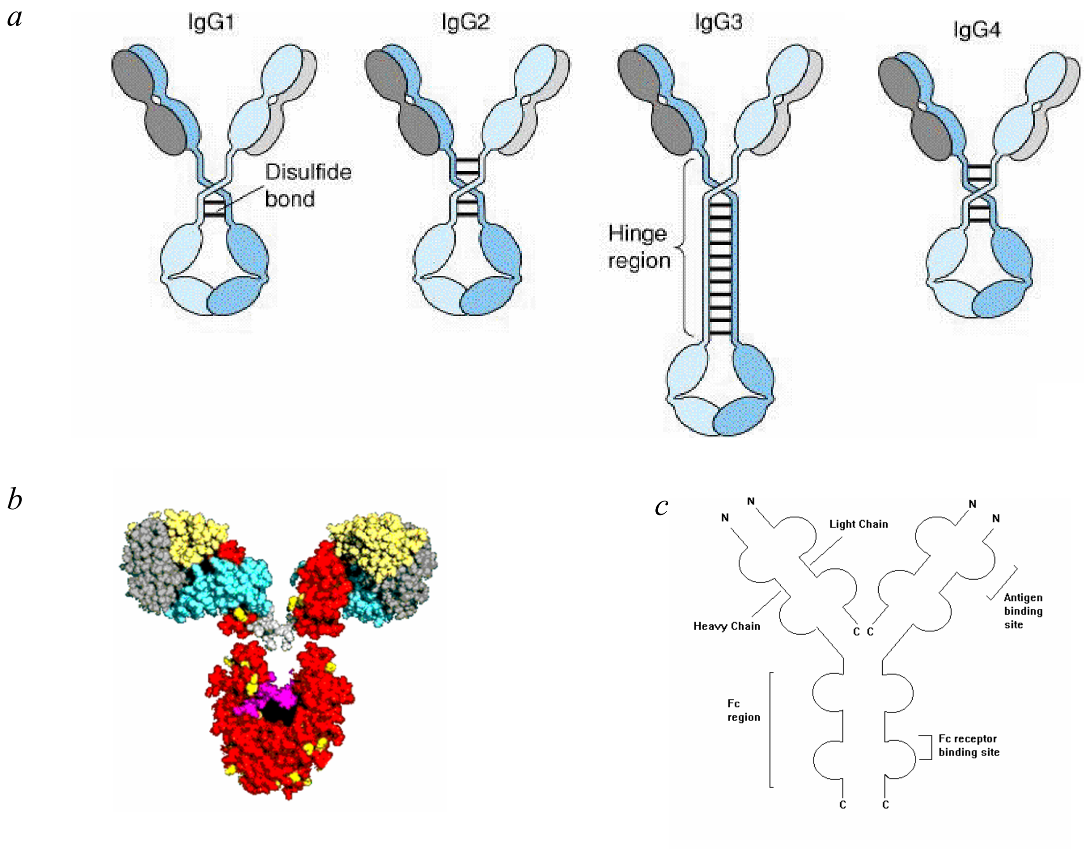

Figure 2.4: (*a*) The general structure of the four subclasses of human IgG. (*b*) The residues which differ between IgG1 and IgG3 are indicated in yellow (*c*) Schematic diagram of an IgG molecule.

Heavy chains (H) of all IgG isotypes are associatd with light (L) chains of two isotypes -- κ and λ. Thus, the basic H_2L_2 composition of an antibody can be specified in terms of its H and L isotypes; *e.g.,* $\varepsilon_2\kappa_2$, $(\mu_2\lambda_2)_5$, etc. The adhesion assays described here take advantage of the versatility afforded by using IgG. Purified IgG in many subtypes and species is inexpensive and readily available.

IgG activates and fixes complement, opsonizes bacteria, and mediates Antibody-Dependent Cellular Cytoxicity (ADCC). It is actively transported across the placenta and it a secondary response (3-5 days)

IgM Structure

Plasma IgM circulates as a pentamer comprised of five heavy chains---light chain pairs. The pentamer is held together by disulfide bonds, and at the center of the molecule is a single peptide called the J chain, which induces the joining of the monomers into the pentamer. The J chain is synthesized by the B lymphocyte (or plasma cell) that makes the IgM.

IgM activates and fixes complement and is the most efficient immunoglobulin at activating complement via the classic pathway. It is an antigen receptor for the B cell and a primary response (7-10 days) antibody.

FcγIII Receptors

The structural segments of cell surface receptors consist of distinct domains as follows: a glycosylated extracellular domain linked to either a transmembrane (TM) domain with a cytoplasmic tail or to a glycosylphosphatidylinositol (GPI) moiety without TM and cytoplasmic domains. The anchor can influence the function of a receptor. TM anchors of some receptors carry information for protein internalization and subunit association, whereas those of other receptors transduce signals. The GPI moiety consists of a glycan core sandwiched between ethanolamine and a lipid tail. Ethanolamine is covalently attached to the carboxyl terminus of the protein by an amide bond, whereas the lipid tail directly inserts into the outer leaflet of the membrane but does not cross the bilayer. The GPI anchor has been implicated in facilitating the lateral mobility of the protein on the cell surface and enhancing receptor-mediated cell adhesion.

There are four known eukaryotic receptors that naturally exist in both membrane anchor isoforms: neural cell adhesion molecule, lymphocyte function-associated antigen 3, vascular cell adhesion molecule 1, and Fcγ receptor III (FcγRIII or CD16). Neural cell adhesion molecule mediates Ca^{2+}-independent homophilic adhesion during the development of neurons with the GPI-anchored isoform being expressed later in development than the TM-anchored isoform. Lymphocyte function-associated antigen 3 is expressed on human erythrocytes as a GPI-anchored protein but on all nucleated cells as both membrane anchor isoforms. Vascular cell adhesion molecule 1 has been found with both anchors in murine but not in human cells. The TM anchored FcγRIIIa (CD16a) is expressed on macrophages, natural killer (NK) cells, and subsets of monocytes and T cells. The GPI-anchored FcγRIIIb (CD16b) is only expressed on neutrophils. The physiological significance of this coexistence of two distinct membrane anchor isoforms for the same receptor is not clear.

CD16 is a 50-80-kDa highly glycosylated cell surface receptor for monomeric IgG. CD16b is polymorphic with the two alleles being termed neutrophil alloantigen 1 (NA1) and 2 (NA2). CD16a and CD16b are products of two highly homologous genes, and their 191 amino acid extracellular domains differ by only 6 amino acids (Figure. 2.5). CD16b lacks the 20-amino acid TM segment as well as the 25-amino acid cytoplasmic domain of CD16a. In addition, the surface expression of CD16a requires associated subunits, the γ chain of the Fc receptor or the ζ chain of the T cell receptor, which form a homo- (γ -γ or ζ- ζ) or hereto (γ -ζ)-dimer in complex with CD16a (Figure 2.5). Binding of antigen-constrained IgGs brings about cross-linking of CD16, which can trigger a variety of immune functions, including immune complex clearance, phagocytosis, antibody-dependent cellular cytotoxicity, release of inflammatory mediators, and enhancement of antigen presentation.

Ligand binding of CD16 can be influenced by a number of factors. CD16a on NK cells binds monomeric human IgG (hIgG) with higher affinity than CD16b on neutrophils. It is not known, however, to what degree this differing affinity is due to the differences in the extracellular domain, in the membrane anchor, or in the cellular background of the two membrane isoforms. The two alleles of CD16b, which differ by four amino acids and two glycosylation sites in the ectodomain (Figure 2.5), have the same affinity for hIgG1 complex but different affinities for hIgG3 complex. NK cell CD16a has a higher affinity for hIgG than monocyte CD16a despite the fact that the two proteins have an identical polypeptide core, suggesting that glycosylation can influence CD16a's affinity for the ligand. Miller *et al.* reported higher affinity for murine IgG2a (mIgG2a) of CD16a than of CD16a-GPI, a molecule created by replacing the TM and cytoplasmic domains of CD16a with a GPI anchor. These authors suggested an affinity-enhancing role for the associated γ chain of CD16a. The second specific goal of this thesis is to determine whether the binding differences observed between the different CD16 isoforms are a result of the different anchor mechanisms.

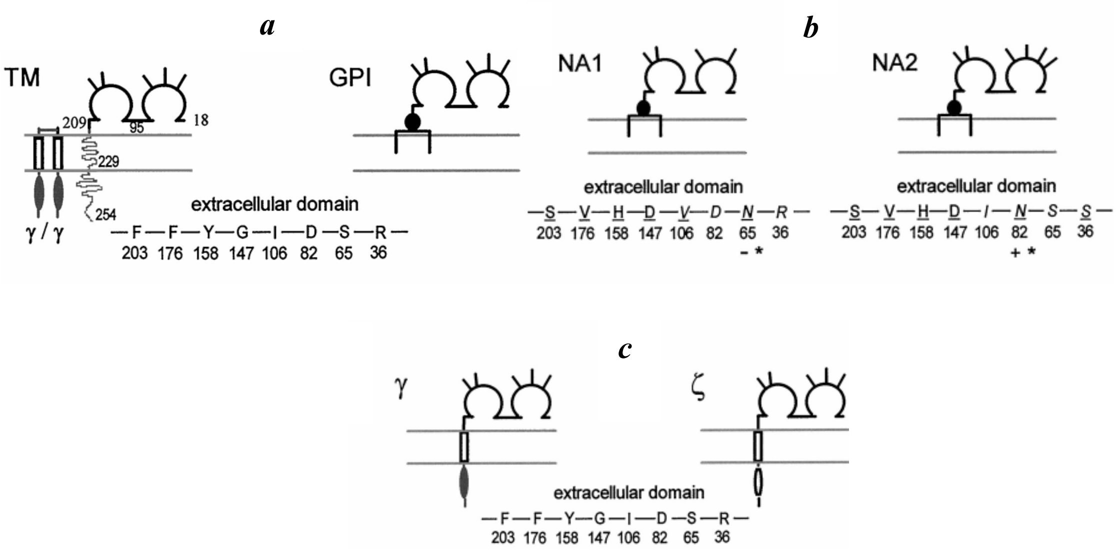

Figure 2.5: Schematic of receptor and CD16 isoforms. (*a*) two CD16a membrane anchor isoforms. (*b*) two CD16b alleles. (*c*) two CD16a-subunit chimeras. The extracellular domains, which begin at amino acid 18, are depicted as two Ig-like globules with the glycosylation sites shown as sticks. The amino acids in the ectodomain that differ among the various molecules are listed. Comparing to those in CD16a, the different amino acids in CD16b are underlined, and the differences between the two CD16b alleles are shown in italics. The lost glycosylation site in CD16b^{NA1} due to the change Ser-65 → Asn-65 is indicated by −*, whereas the gained glycosylation site in CD16b^{NA2} due to the change Asp-82 → Asn-82 is indicated by +*. The CD16a-TM and the two CD16a-subunit chimeras differ by the TM and cytoplasmic domains but have the same ectodomain and anchor to the cell surface via the same TM mechanism. By comparison, the CD16a-GPI and the two CD16b alleles use a lipid tail to insert into the outer leaflet of the bilayer but do not cross the membrane. The GPI moiety is of similar size to an Ig globule. Hence it may extend the membrane-proximal ligand-binding Ig domain further above the membrane. It may also alter the orientation and/or conformation of the molecule.

CHAPTER 3

MATERIALS AND METHODS

cDNA Constructs

The cDNAs encoding human CD16A-TM in a pSVL vector and CD16a-GPI in a pCDM8 vector were provided by Dr. J. Ravetch (Sloan-Kettering Institute for Cancer Research, New York). The CD16a-TM cDNA was further subcloned into the PCR3uni vector (Invitrogen, San Diego, CA), see reference. The cDNAs encoding the two human CD16b alleles, the γ subunit of rat FcϵRI, the two chimeric CD16a-γ and CD16b-ζ, and the hygromycin or neomycin resistance genes have been described (Nagarjan et al. (1995)).

Cells And Antibodies

Our CHO cells transfected to express human CD16a have previously been described (Nagarjan et al., 1995). The control CHO cells (untransfected, K1 and transfected to express $\alpha_{IIb}\beta_3$, A5) were generous gifts from Dr. Mark H. Ginsberg (Scripps Research Institute, La Jolla, CA). CHO cells were cultured in Roswell Park Memorial Institute (RPMI) 1640 media (Sigma, St. Louis, MO) supplemented with 2 mM L-glutamine (Sigma), and 10% fetal bovine serum (FBS) (Gibco BRL, Grand Island, NY). For the CD16a transfectants, 400 μg/ml geneticin (Life Technologies, Gaithersburg, MD) was included in the culture media as a selection antibiotic to suppress the nontransfected cells. The expression of CD16a was periodically checked via flow cytometry. Because the micropipette is a single-cell assay and cell-to-cell variations contribute significantly to experimental deviation, a homogeneous cell population expressing a uniform level of CD16a is desirable. To obtain homogeneous populations of cells expressing different receptor densities, CHO cells were sorted through a FACSort (Becton Dickinson, San Jose, CA). The tight receptor expression distributions in the sorted populations lasted ~1 month before the cells returned to their original, more heterogeneous characteristics.

Observing approved NIH guidelines, fresh blood from healthy donors was collected by venipuncture into sterile vacutainers (Becton Dickinson) with EDTA as an anticoagulant. Tubes were refrigerated for 4 h to allow serum separation. The RBC fraction was collected, washed twice in RPMI 1640 with 5% FBS, and then stored at 5°C. These cells could be used for up to ~2 weeks, after which lysis of the RBCs became apparent.

Total human IgG (hIgG) (Lampire, Pipersville, PA) and rabbit IgG (RbIgG) (Sigma) were used as ligands for CD16a. The fluorescein isothiocyanate (FITC)-coupled goat polyclonal anti-human, anti-rabbit, and anti-mouse antibodies used in flow cytometry were purchased from Sigma. The monoclonal antibody (mAb) Leu-11b (mouse IgM) specifically directed against CD16 was purchased from Becton Dickinson. Another anti-CD16 mAb Fcgran1 CLB (mouse IgG2a) and the irrelevant control mAb X63 (mouse IgG1) were produced in house as previously described (Nagarjan et al., 1995). The fragmentation of CLB into Fc and Fab subunits was done by Lampire. The genetically engineered dimeric soluble form of CD16a (sCD16a) and the control soluble molecule B7 (sB7) were produced by our laboratory and will be described in detail elsewhere (Li et al. (2000)).

Coating Of Ligands

Ligand was coated onto RBCs by a standard chromium chloride ($CrCl_3$) coupling protocol (Gold and Fudenberg, 1967; Kofler and Wilk, 1977). Briefly, 10^8 RBCs were suspended in 250 µl saline (4% hematocrit). When ligand (hIgG, RbIgG, or a control protein bovine serum albumen (BSA); Sigma) in phosphate-free medium (typically at 10 µg/ml) was added along with 250 µl of 0.001% $CrCl_3$ solution in 0.02 M acetate buffer, pH 5.5, spontaneous coupling occurred. After 5 min the reaction was quenched with phosphate-buffered saline (PBS), 5 mM EDTA with 1% BSA. RBCs were used immediately after protein coating. This coupling reaction is accomplished almost immediately and is thought to involve the chemical bonding of protein carboxyl groups with membrane proteins on the RBC. The reaction is nonspecific, the orientation of the coated protein with respect to the membrane is most likely random, and the ligand density has to be determined for each reaction to circumvent variability in the coating. Nevertheless, the method is extremely efficient in terms of time, coating densities, and minimum alteration of RBC membrane characteristics.

Determination Of Receptor And Ligand Densities

The surface densities of receptors and ligands were determined primarily via flow cytometry analysis. Samples of RBCs used in the micropipette experiment were incubated with FITC-labeled goat anti-human or anti-rabbit antibodies, depending on the origin of the coated IgG ligands. For negative controls, the hIgG (or RbIgG)-coated RBCs were incubated with the FITC-labeled goat anti-rabbit (or anti-human) antibodies. CHO cell samples were first preincubated with the mouse anti-CD16 mAb Fcgran1 CLB (or without a primary antibody for control) and then with a FITC-labeled goat anti-mouse polyclonal secondary antibody. The fluorescent intensities of the cells were compared to standard calibration beads (Flow Cytometry Standards Corp., San Juan, PR) to determine the mean number of events per particle, which was directly converted into labeled protein per cell with manufacturer-provided software.

Receptor densities on different CHO cell populations were cross-checked by radioimmunoassay. Fab fragments of CLB were iodinated using Iodo-Gen (Pierce, Rockford, IL) (Selvaraj et al., 1988). CHO cells were incubated in titrated concentrations of CLB-Fab, and the bound fraction was determined with a gamma counter. Scatchard analysis (Scatchard, 1949) was employed to derive the (3D) affinity (of CD16a-CLB binding) and the (average) receptor number per cell, which was then divided by the apparent area of the spherical cell to convert to surface density. Determination of receptor density by Scatchard analysis was less desirable than that of flow cytometry because it required the constant availability of ^{125}I-CLBFcgran-1 (Fab fragment); however, the correlation between the two methods is good (R^2 ~90%) (Chesla et al. (1998)) and imparts more confidence on our surface protein density estimations. Radiolabeling of proteins was done by using IODO-GEN-coated tubes (Pierce) (Nagarajan et al. (1995)).

Three-Dimensional Binding Studies

The binding affinities of CLBFcgran-1 Fab for the two CD16a membrane anchor isoforms were determined by Scatchard analysis (Scatchard (1949)). The low affinity of monomeric IgG for CD16 makes direct measurement by the Scatchard method unreliable. To circumvent this difficulty, a competitive inhibition assay was used where the low affinity ligand IgG competes with the high affinity antibody CLBFcgran-1 for receptor binding (Horovitz et al. (1987)). Briefly, CHO cells were grown in flasks until near confluence. Cells were rinsed once in PBS and then removed from the flask using PBS/EDTA (containing 5 mM EDTA). After washing, they were resuspended at 1 × 10^6 cells/ml in PBS/EDTA, pH 7.5. Cells were then added to V-bottom 96-well plates at 100 µl per well. The wells were precoated with 1% IgG-free BSA (Sigma) in PBS by incubating at room temperature for 2 h. They were rinsed with PBS/EDTA and kept on ice until the cells were added. After adding cells, the plates were spun at 2000 rpm for 2 min. The supernatant was removed, and a solution of 50 µl of PBS/EDTA and titrated amounts of IgG was added to each well with mixing. Then, 50 µl of PBS/EDTA, 0.25-0.50 µg/ml ^{125}I-CLBFcgran-1 Fab was added to each well, followed by a 45-min incubation on a shaker at 5°C. After washing 3 times, the cell pellets were removed and counted in a gamma counter.

In the presence of increasing concentrations of the low affinity ligand (IgG, concentration c_l^l), the binding of the high affinity ligand (^{125}I-CLBFcgran-1 Fab, concentration c_l^h) to the cell surface receptor (CD16) is gradually reduced or displaced. The displaced fraction (*F*), defined as the bound fraction (*f*) of CLBFcgran-1 normalized by the value when no IgG was present (f_0), can be expressed by Equation 3-1.

$$F \equiv \frac{f}{f_o} = \Big\{ \Big(c_r + c_l^h + c_l^l K_a^l \big/ K_a^h + 1 \big/ K_a^h \Big) - \Big(c_r + c_l^h + c_l^l K_a^l \big/ K_a^h + 1 \big/ K_a^h \Big)^2 - \tag{3-1}$$

$$4 c_r c_l^h \Big]^{1/2} \Big\} \Big/ 2 c_r$$

Since the affinity to CD16 of ^{125}I-CLBFcgran-1 Fab (K_a^h) and the receptor concentration (c_r) were predetermined from a separate experiment by Scatchard analysis, the only unknown in Equation 3-1 is the affinity of IgG (K_a^l). Therefore, K_a^l can be calculated from a single measurement of F without the experimental displacement curve to include data at the IC_{50} point. To increase the accuracy of the K_a^l value, however, the predicted displaced fraction (Equation 3-1) was nonlinearly fit to the entire F *versus* c_l^l data set.

The Micropipette System

The micropipette system used in this laboratory was designed, built, and calibrated in house; the majority of the components were purchased off the shelf (Delobel, 1992). It is similar to those established in other laboratories (Paul Sung, University of California at San Diego; Evan Evans, University of British Columbia; Robert Hochmuth, Duke University). The system consists of video-enhanced optical microscopy, micromanipulation, and pressure regulation subsystems.

The centerpiece of the microscopic system is a Zeiss inverted microscope (Axiovert 100; Oberkochan, Germany) with a 100× oil immersion, 1.25 N.A. objective. Diffraction is minimized with a green light (546-nm wavelength) band-pass (5-nm bandwidth) filter that also reduces any photochemical damage to the RBC. Additional magnification is obtained using a 5× relay lens, leading to a charge-coupled device (CCD) camera (model 72S; Dage-MTI, Michigan City, IN). A digital image processor (model DSP-2000; Dage-MTI) is used to enhance the image. The signal also passes through a digital voltage multiplexer (model 401; Vista Electronics, Ramona, CA), which allows video integration and display of a timer on screen. Recording is accomplished using a super VHS video cassette recorder (model AG-7355; Panasonic, Secaucus, NJ). A video monitor (Panasonic) displays the image at a final magnification of ~2500× as calibrated by a stage micrometer.

Micropipettes are made from borosilicate glass tubing (Richland Glass, Richland, NJ) with an outside diameter of 1 mm and an inside diameter of 0.7 mm. To guarantee clean pipettes, the original glass tubing is cleaned with acetone, cleaned a second time in a boiling solution of 50% ethanol for 1 h, and dried again. A two-step process is used with the first, utilizing a micropipette puller (model 700D; Kopf, Tujunga, CA). Next, a microforge (built in house, similar to commercial models, except that a glass bead is added to the filament, adapted from the laboratory of Robert M. Hochmuth, Duke University, Durham, NC) is used to break the micropipette with a flush tip at the desired diameter. The pipettes are connected to the pressure regulation system through stainless steel injection holders. Each pipette can be coarsely manipulated by a mechanical drive mounted on the microscope and finely positioned with a three-axis hydraulic micromanipulator (Narishige, Tokyo, Japan). In addition, one of the pipette holders is mounted on a piezo translator (Physik Instrumente, Waldbronne, Germany), the driver of which is controlled by a computer to achieve precise and repeatable movement of the pipette in an adhesion test cycle. To avoid vibration of the micropipettes during the experiment, the microscope, along with the micromanipulators, is seated on an air suspension table (Kinetics Systems, Boston, MA).

The pressure regulation subsystem is used to control suction during the experiment and is critical for tuning the sensitivity of the RBC picoforce transducer. A hydraulic line connects the micropipette holder to a fluid reservoir. The centerpiece of the design is a fine jack that allows the height of the reservoir to be precisely manipulated. A metric long-range dial indicator (Starrett, Athol, MA) was attached to the reservoir to measure its position and therefore the applied vacuum pressure in mm H_2O.

Micropipette Adhesion Test Cycle

CHO cells were removed from flasks with 5 mM EDTA/PBS, washed twice in RPMI, and then stored on ice until injection into the micropipette chamber. The chamber consists of two coverslips attached to a stainless steel holder on the top and bottom to allow optical imaging, while open on two sides to allow micropipette access. The solution used in the chamber during the experiment was half isotonic (1:1 distilled H_2O and Hanks' balanced salt solution (HBSS) without Ca^{+2} (Sigma) and 1% BSA), which caused the RBCs to swell to nearly spherical shape, but had no detectable effect on the CHO cells' viability, consistent with the report of a recent paper (Setiadi et al., 1998) that CHO cells have a high tolerance to variations in the ionic strength in the culture medium. After single CHO and RBC cells were captured and positioned with the apposing pipettes, the computer program for repeated adhesion test cycles was initiated, with the movement of the RBCs precisely driven by the piezo translator and the CHO cell held stationary (Fig. 3.1).

An adhesion test cycle consists of impinging the RBC into controlled contact (Fig. 3.1*a*), allowing the contact to continue for a predetermined incubation time, then retracting the RBC from the CHO cell at a predetermined rate and observing any adhesions. The contact area is managed by controlling the amount of RBC impingement on the CHO cell surface. Because the piezo-controlled RBC returns to the same location after every adhesion stroke attempt, impingement is controlled by manual adjustment of the CHO cell location. In this way, the contact area and location were held essentially constant.

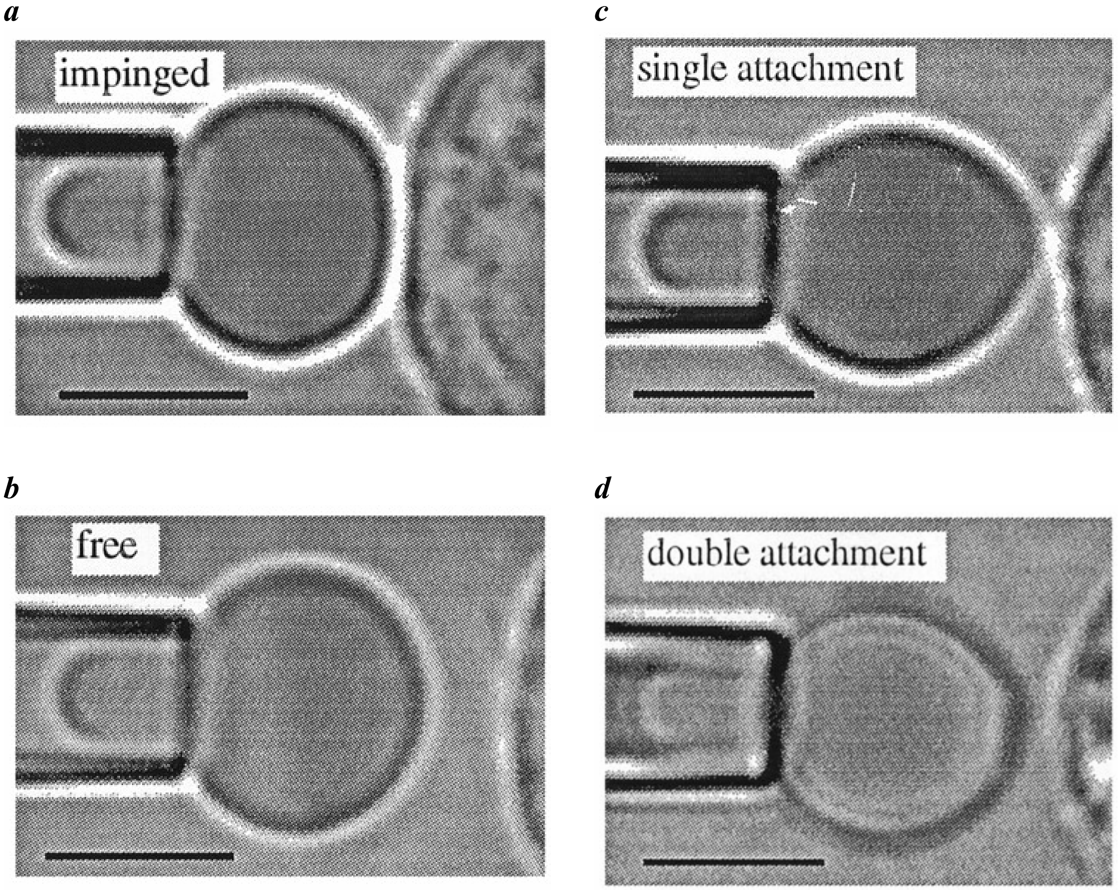

Figure 3.1: Photomicrographs of a typical adhesion test involving an IgG-coated RBC aspirated by a micropipette (left) and a CD16a-expressing CHO cell, aspirated by another micropipette (only partially shown, right). (*a*) The RBC was brought into contact with the CHO cell with an overall apparent contact diameter of ~2 µm. The contact area and time between the CHO and RBC cells were carefully controlled. (*b*) The unaspirated portion of the RBC is shown in its free, spherical shape. (*c*) A retracting RBC that was previously allowed to adhere to a CHO cell. The attachment site between the two cells appears as a single point in the microscopic image. (*d*) The retracting RBC adheres to the CBO cell to the CHO cell via two spatially distinctly separate point attachments.

Adhesions could easily be unambiguously distinguished from nonadhesions (Fig. 3.1*b*) by deflections in the RBC surface at the area of contact (Fig. 3.1*c* and *d*). Most observed adhesions were point attachments near the apex of the RBC (Fig. 3.1*c*). Multiple point attachments were also occasionally detected (Fig. 3.1*d*), especially at higher adhesion frequencies. The outcome of each test was scored as one if adhesion resulted, and as zero if not.

The adhesion test cycle was then repeated at the same contact area. Typically a sequence of 50-200 such repeated tests was performed with the same pair of cells. The binary adhesion scores were averaged up to the most recent test, and this running frequency of adhesion was plotted against the test cycle count for a given sequential test series. It is the analysis of this running frequency that yields an estimate of the adhesion probability per contact.

Data Analysis

The theoretical solutions were fitted to the experimental data by a numerical routine that employs the Levenberg-Marquart method to evaluate the parameters that minimize the sum of squared weighted (by the reciprocal standard deviations) errors (χ^2) between the data and the predictions (Press et al., 1989). The program also uses the spread and standard deviation of the data to estimate the standard deviations of the fitted parameters. To determine the most appropriate kinetic mechanism, the goodness of fit of various models as measured by the χ^2 values for the same data set were compared (Piper et al., 1998).

Probabilistic And Deterministic Kinetic Models

The experiment of the present method is designed to operate in such a way that adhesion appears as a random event, i.e., whether or not binding occurs in a particular adhesion test is nondeterministic, even when all conditions controllable by the experimenter, including the area (A_c) and duration (t) of contact between the two cells, as well as their respective surface densities of receptors (m_r) and ligands (m_l), are kept identical. It is hypothesized that such randomness is a manifestation of the stochastic nature inherent in the chemistry of receptor-ligand binding, which becomes significant when the number of bonds per cell is small. A single deterministic value (scalar) for the (averaged) surface density of bonds, $\langle n \rangle / A_c$, is no longer adequate for a complete description of the phenomenon, as the number of bonds that an adherent cell may have becomes a discrete, time-varying, random variable that fluctuates significantly. Instead, one considers a probability vector $\{p_0, p_1, ..., p_n, ..., p_{A_c m_{\min}}\}$ to describe the state of the system. In other words, the adhesion could be mediated by any number of bonds ranging from 0 to $A_c m_{\min}$, where $m_{\min} = \min(m_r, m_l)$. Each possible scenario, say adherent via n bonds, has a defined likelihood, given by p_n.

For the experiment in question, there is no bond at the instant when the two cells are just brought into contact with each other ($t = 0$), so

$$p_n(0) = \begin{cases} 1 & for\ n = 0 \\ 0 & for\ n \neq 0 \end{cases} \tag{3-2}$$

Upon contact, bonds start to form, so $p_n(t)$ ($n > 0$) increases with time t. For a single step reversible reaction of ν_r receptors (designated M_r) binding to ν_l ligands (designated M_l) to form ν_b bonds (designated M_b), as given by the chemical reaction equation

$$\nu_r M_r + \nu_l M_l \underset{k_r^0}{\overset{k_f^0}{\rightleftarrows}} \nu_b M_b,$$

the master equations that govern the rates of change of these $A_c m_{\min} + 1$ probability components can be written as

$$\begin{aligned}\frac{dp_n}{dt} = {} & (n+1)^{\nu_b}\frac{k_r^0}{A_c^{\nu_b-1}}p_{n+1} - [(A_c m_r - \frac{\nu_r}{\nu_b}n)^{\nu_r}(A_c m_l - \frac{\nu_l}{\nu_b}n)^{\nu_l}\frac{k_f^0}{A_c^{\nu_r+\nu_l-1}} + n^{\nu_b}\frac{k_r^0}{A_c^{\nu_b-1}}]p_n \\ & + [A_c m_r - \frac{\nu_r}{\nu_b}(n-1)]^{\nu_r}[A_c m_l - \frac{\nu_l}{\nu_b}(n-1)]^{\nu_l}\frac{k_f^0}{A_c^{\nu_r+\nu_l-1}}p_{n-1}\end{aligned} \tag{3-3}$$

where k_f^0 and k_r^0 are, respectively, the forward and reverse rate constants, of dimensions $[\text{area}]^{\nu_r+\nu_l-1}[\text{time}]^{-1}$ and $[\text{area}]^{\nu_b-1}[\text{time}]^{-1}$, respectively. The superscript 0 is used to indicate that these are rate constants measured under the condition that there is no external force applied to the bonds.

The above probabilistic master equations are generalization of the deterministic kinetic equation, as can be seen in the following derivation. Multiplying Eq. 3-3 by n/A_c and summing the resulting equation from 0 to $A_c m_{\min}$ yields

$$\frac{d}{dt}\left(\frac{<n>}{A_c}\right) = k_f^0[(m_r - \frac{\nu_r}{\nu_b}\frac{<n>}{A_c})^{\nu_r}(m_l - \frac{\nu_l}{\nu_b}\frac{<n>}{A_c})^{\nu_l} + \frac{\sigma_n^{(\nu_r+\nu_r)}}{A_c^{\nu_r+\nu_l}}] - k_r^0[\left(\frac{<n>}{A_c}\right)^{\nu_b} + \frac{\sigma_n^{(\nu_b)}}{A_c^{\nu_b}}] \tag{3-4 a}$$

where $\langle\ \rangle$ denotes averaging. $\langle n\rangle/A_c$ in Eq. 3-4a can readily be identified as corresponding to the deterministic density of bonds. The two measures of fluctuations in the bond number are

$$\sigma_n^{(\nu_r+\nu_l)} \equiv \sum_{i=0}^{\nu_r}\sum_{j=0}^{\nu_l}\binom{\nu_r}{i}\binom{\nu_l}{j}(A_c m_r)^{\nu_r-i}(A_c m_l)^{\nu_l-j}(-\frac{\nu_r}{\nu_b})^i(-\frac{\nu_l}{\nu_b})^j(<n^{i+j}> - <n>^{i+j}) \tag{3-4 b}$$

and

$$\sigma_n^{(\nu_b)} \equiv <n^{\nu_b}> - <n>^{\nu_b} \qquad (3\text{-}4\ c)$$

It can readily be shown that

$$\sigma_n^{(\nu_b)} = 0 \qquad \text{when } \nu_b = 1,$$

$$\sigma_n^{(\nu_r + \nu_l)} = 0 \quad \text{when } \nu_r + \nu_l = 1,$$

$$\sigma_n^{(\nu_b)} = \sigma_n^2 \qquad \text{when } \nu_b = 2, \text{ and}$$

$$\sigma_n^{(\nu_r + \nu_l)} = \sigma_n^2 \text{ when } \nu_r = \nu_l = 1,$$

where σ_n^2 is the variance of *n*. For large systems, the fluctuations are small. Dropping $\sigma_n^{(\nu_r + \nu_l)}$ and $\sigma_n^{(\nu_b)}$ from Eq. 3-4*a* reduces it to the familiar deterministic kinetic equation, as expected.

Closed-Form Transient And Steady-State Solutions

Two simplified versions of Eq. 3-3 have been discussed in the literature. The first case is when one of the molecular species excessively outnumbers the other. Under such a condition the number of the former species [density $m_{\max} = \max(m_r, m_l)$] in the free state can be approximated as constant in the contact area, as the reaction is limited by the availability of the latter species (density $m_{\min}$). The $\nu_r = \nu_l = \nu_b = 1$ case of such a simplified version of Eq. 3-3 was used by Cozens-Roberts et al. (1990) when they first applied the probabilistic kinetic formulation of McQuarrie (1963) to the analysis of receptor-ligand binding. The solution to the simplified version of Eq. 3-3 that satisfies the initial condition given by Eq. 3-2 is of the form of the binomial distribution (Chesla, Selvaraj, Zhu (1998)):

$$p_n(t) = \binom{A_c m_{\min}}{n} \left[p(t)\right]^n \left[1 - p(t)\right]^{A_c m_{\min} - n} \tag{3-5a}$$

where $p(t)$ is the probability of forming one bond, given by

$$p(t) = \frac{1 - \exp(-k\,t)}{1 + (m_{\max} K_a^0)^{-1}} \tag{3-5b}$$

The two parameters,

$K_a^0 = k_f^0 / k_r^0$ and

$k = m_{\max} k_f^0 + k_r^0$,

are the equilibrium association constant (binding affinity) and the overall rate (reciprocal time scale) of the reaction, respectively.

The second case is that in which the number of bonds that have nonvanishing probabilities is much smaller than the numbers of receptors and ligands. Under such a condition the formation of a small number of bonds will not significantly deplete the free receptors and ligands available in the contact area, so Eq. 3-3 can be approximated by one that neglects, respectively, n and $(n\text{-}1)$ in the $[A_c m_j - (\nu_j/\nu_b)n]$ and $[A_c m_j - (\nu_j/\nu_b)(n - 1)]$ (subscript $j = r$ or l) terms. Such simplified master equations (with variable kinetic rates) have been discussed by Long et al. The $\nu_b = 1$ case (with constant kinetic rates) was employed by Kaplanski et al. (1993), who solved the equations numerically. (Different notations, $k_+ = A_c m_r^{\nu_r} m_l^{\nu_l} k_f^0$ and $k_- = k_r^0$, were used by Kaplanski et al. (1993). The analytical solution (Chesla, Selvaraj, Zhu (1998)) is of the form of the Poisson distribution:

$$p_n(t) = \frac{<n>^n}{n!} \exp(-<n>) \tag{3-6a}$$

where $\langle n \rangle$ is the average number of bonds, given by

$$<n> = A_c m_r^{\nu r} m_l^{\nu l} K_a^0 [1 - \exp(-k_r^0 t)] \tag{3-6b}$$

These results are not surprising, as the assumptions on which Eq. 3-3 is based are equivalent to those underlying the binomial and Poisson distributions. Both distributions have been suggested to describe the formation of a small number of bonds (Capo et al., (1982); Chesla et al., (1995); Evans and Ritchie, (1994)). However, in contrast to the previous works that assumed p and $\langle n \rangle$ given a priori, closed-form solutions provide their explicit expressions, Eqs. 3-5*b* and 3-6*b*.

Although an explicit transient solution to Eq. 3-3 in the form similar to that of Eq. 3-5 or 6 for arbitrary ν_r, ν_l, and ν_b values has not been found, an implicit solution can be obtained by assuming $\{p_n(t)\} = \{A_n\}e^{rt}$ to convert the problem of solving $A_c m_{min} + 1$ coupled, first-order, constant coefficient, ordinary differential equations to one of finding the eigenvalues r and eigenvectors $\{A_n\}$ of the corresponding linear algebraic system (Boyce and DiPrima, (1977)).

At steady state, explicit exact solutions for Eq. 3-3 have been obtained for arbitrary stoichiometric coefficients (Zhu et al., (1998)). These steady-state solutions, derived by using mathematical induction (Piper, 1997), are, respectively:

$$p_n(\infty)=\begin{cases}\{\sum\limits_{m=0}^{A_c m_{\min}}(m!)^{\nu_r+\nu_l-\nu_b}\left[\begin{pmatrix}\frac{\nu_b}{\nu_r}A_c m_r\\ m\end{pmatrix}\right]^{\nu_r}\left[\begin{pmatrix}\frac{\nu_b}{\nu_l}A_c m_l\\ m\end{pmatrix}\right]^{\nu_l}\left[\left(\frac{\nu_r}{\nu_b}\right)^{\nu_r}\left(\frac{\nu_l}{\nu_b}\right)^{\nu_l}\frac{K_a^0}{A_c^{\nu_r+\nu_l-\nu_b}}\right]^m\}^{-1} & n=0\\ p_0(\infty)(n!)^{\nu_r+\nu_l-\nu_b}\left[\begin{pmatrix}\frac{\nu_b}{\nu_r}A_c m_r\\ n\end{pmatrix}\right]^{\nu_r}\left[\begin{pmatrix}\frac{\nu_b}{\nu_l}A_c m_l\\ n\end{pmatrix}\right]^{\nu_l}\left[\left(\frac{\nu_r}{\nu_b}\right)^{\nu_r}\left(\frac{\nu_l}{\nu_b}\right)^{\nu_l}\frac{K_a^0}{A_c^{\nu_r+\nu_l-\nu_b}}\right]^n & n>0\end{cases}\qquad(3\text{-}7)$$

$$p_n(\infty)=\begin{cases}\{\sum\limits_{m=0}^{A_c m_{\min}}(m!)^{\nu_i-\nu_b}\left[\begin{pmatrix}\frac{\nu_b}{\nu_i}A_c m_{\min}\\ m\end{pmatrix}\right]^{\nu_i}\left[\left(\frac{\nu_i}{\nu_b}\right)^{\nu_i}\frac{m_{\max}^{\nu_a}K_a^0}{A_c^{\nu_i-\nu_b}}\right]^m\}^{-1} & n=0\\ p_0(\infty)(n!)^{\nu_i-\nu_b}\left[\begin{pmatrix}\frac{\nu_b}{\nu_i}A_c m_{\min}\\ n\end{pmatrix}\right]^{\nu_i}\left[\left(\frac{\nu_i}{\nu_b}\right)^{\nu_i}\frac{m_{\max}^{\nu_a}K_a^0}{A_c^{\nu_i-\nu_b}}\right]^n & n>0\end{cases}\qquad(3\text{-}8)$$

$$p_n(\infty)=\begin{cases}[\sum\limits_{m=0}^{\infty}\frac{(A_c^{\nu_b}m_r^{\nu_r}m_l^{\nu_l}K_a^0)^m}{(m!)^{\nu_b}}]^{-1} & n=0\\ p_0(\infty)\frac{(A_c^{\nu_b}m_r^{\nu_r}m_l^{\nu_l}K_a^0)^n}{(n!)^{\nu_b}} & n>0\end{cases}\qquad(3\text{-}9)$$

where $\nu_a = \nu_r$ and

$\nu_I = \nu_l$ if $m_{\max} = m_r$, but

$\nu_a = \nu_l$ and $\nu_I = \nu_r$ when $m_{\max} = m_l$.

Note that as $t \rightarrow \infty$, Eqs. 3-5 and 3-6 approach, respectively, the $\nu_r = \nu_l = \nu_b = 1$ case of Eq. 3-8 and the $\nu_b = 1$ case of Eq. 3-9, as expected.

These explicit exact steady-state solutions, Eqs. 3-7 through 3-9, are of interest because they greatly facilitate the test of the validity of the binomial and Poisson solutions, Eqs. 3-5 and 3-6. As one might expect from physical intuition, the discrepancies between the binomial and Poisson approximate solutions and the solution to the original master equations, Eq. 3-3, are at maximum at steady state because this is when the average bond number reaches maximum. Thus the discrepancies between the steady-state solutions, Eqs. 3-7 and 8 (or Eqs. 3-7 and 3-9), represent the worse-case scenario for all time-dependent solutions. The results of the validity test are shown in Figure 3.2, in which the $p_0(\infty)$ ratio of the solution to the simplified version to the solution to the full master equations is plotted against either $m_{\max}/m_{\min}$ (Fig. 3.2*a*) or $(\nu_b/\nu_i)A_c m_{\min}/\langle n\rangle_\infty$ (Fig. 3.2*b*). It can be seen that, when $m_{\max}/m_{\min}$ [or $(\nu_b/\nu_i)A_c m_{\min}/\langle n\rangle_\infty$] is on the order of one, Eq. 3-8 (or 9) differs significantly from Eq. 3-7, suggesting the breakdown of the binomial (or Poisson) type of approximation. However, as $m_{\max}/m_{\min}$ [or $(\nu_b/\nu_i)A_c m_{\min}/\langle n\rangle_\infty$] increases to more than 50, the $p_0(\infty)$ ratio quickly approaches unity, supporting the validity of the solution to the simplified master equations in approximating the solution to the full equations in these parameter domains, which correspond to the conditions of the present experiment.

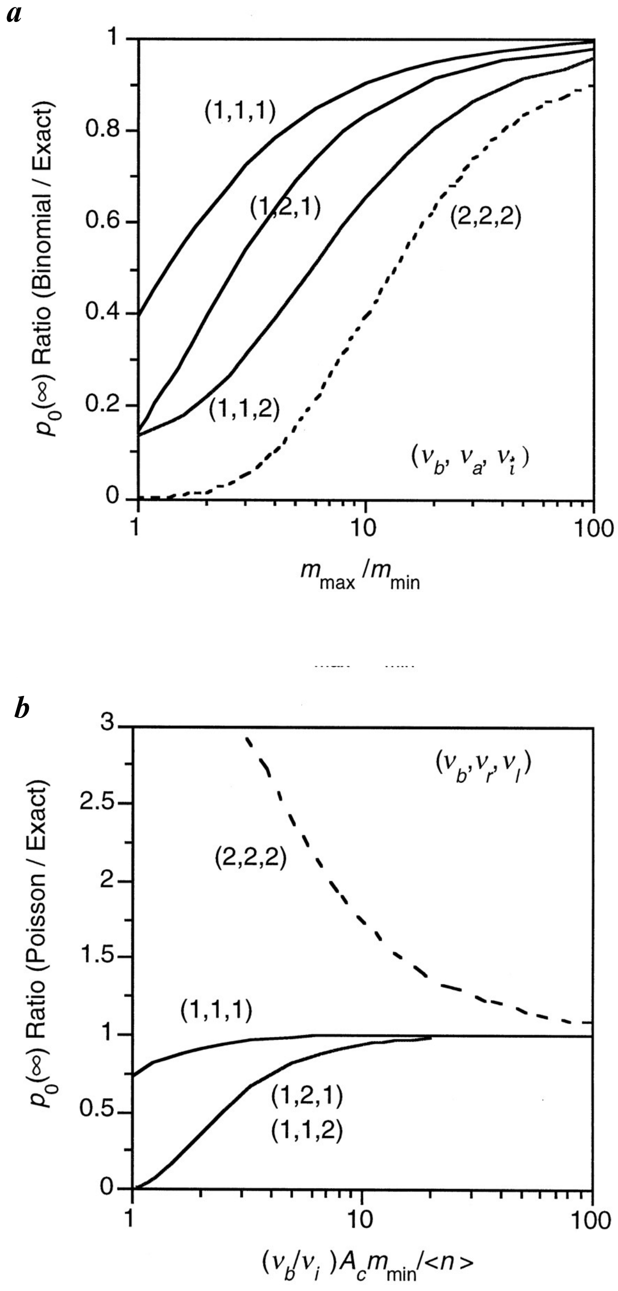

Figure 3.2: Validation of the two simplified master equations in approximating the full master equations. The ratios to the full steady-state solution (Eq. 3-7) of the binomial-type steady-state solution (Eq. 3-8) (*a*), and the Poisson-type steady-state solution (Eq. 3-9) (*b*) are plotted against the parameters m_{max}/m_{min} for the binomial-type solution and $(\nu_b/\nu_i)A_c m_{min}/<n>$ for the Poisson-type solution, respectively, that control the validity of the corresponding approximation. Different curves represent different stoichiometric coefficients (ν_b, ν_r, ν_l), as indicated. Note that the experimental conditions in the present work satisfy $[(\nu_b/\nu_i)A_c m_{min}/<n>] > 100$, which is in the parameter range that validates the two types of approximation.

Micropipette Force Determination Precision

The determination of detachment force can also be extracted from the CD16-IgG reactions observed using the micropipette system. In the determination of detachment force, an estimate of the micropipette systems precision was sought. A precision assessment first requires the determination of the force-deflection relationship, which requires a none trivial analysis of the mechanics of the RBC under a point load bond. In the mechanics literature a solution to a similar problem is available by Reissner (1946). However, the constitutive law used was that of 3-D isotropic elasticity. It is therefore not applicable to the RBC problem because the RBC membrane is known to behave as an anisotropic material whose in-plane mechanical properties are much different from those in the third dimension. Evans analyzed the RBC transducer problem using a finite difference numerical approach and established the sensitivity of such a device. Here a finite difference assessment of the precision of the RBC transducer is also presented so that the results obtained from this and other techniques can be fairly compared. Analytical solutions (via perturbation and linearization) to the membranes mechanics problem are also available in our lab and can be compared to the computational solution. Each of these mechanical solutions contains the components of membrane binding. In addition, the theoretical models are directly validated with independent experimental measurements. The solutions are then used to predict the precision of the force measurement devise, identify the most important concern areas of experimental accuracy, and the influence of binding and area dilution constants to the final solution.

Mechanical characterization of cell membranes has been a biomedical area of research beginning in the early 20th century and continuing into the 1970's with the introduction of the Singer and Nicolson Fluid Mosiac Model. The experimental study of biological membranes has focused mainly on human red blood cells (RBCs) and characterizes their deflective characteristics under load with the use of several properties: elastic and bending moduli. If the membrane undergoes large deformation, the isotropic prestressed tension will no longer dominate. In order to determine the deformed shape of a human RBC membrane surface under applied loads, the stresses need to be related to the strain. A linear elastic assumption is commonly applied to the human RBC and two elastic moduli are defined, the modulus for area dilation, K, and the shear modulus, μ.. The total volume of the enclosed by the membrane is constant during the imposed deformation which is typically assumed axisymmetric about *z*. The 2-D curvilinear coordinate system describing the membrane deformation is presented in Figure 3.3; the shape of the membrane is defined by $r = r(z)$ with *s* defined as the arc length and ϕ as the angle around the *z* axis. Because the problem is axisymmetric the stress resultants τ_s and τ_ϕ are the principle stresses and $\tau_{\phi s}=0$ and $\partial/\partial\phi = 0$. Therefore, the membrane equilibrium equations are presented as, where m and ϕ are directions normal and tangential to the membrane surface, respectively:

$$\frac{c_m}{r}\left[\frac{\partial}{\partial s}\{rM_m\}-M_\phi\frac{\partial r}{\partial s}\right]+\frac{1}{r}\left[\frac{\partial}{\partial s}\{r\tau_m\}-\tau_\phi\frac{\partial r}{\partial s}\right]=0 \qquad (3\text{-}10)$$

$$\frac{1}{r}\frac{\partial}{\partial s}\left[\frac{\partial}{\partial s}\{rM_m\}-M_\phi\frac{\partial r}{\partial s}\right]-c_m\tau_m-c_\phi c_\phi+P_n=0 \qquad (3\text{-}11)$$

The geometries of a micropipette aspirated RBC before (dotted curve) and after (solid curve) the application of a point force on the apex is shown in Figure 3.3. This geometry also illustrates the nomenclature of the membrane equilibrium equations given in equations 3-10 and 3-11.

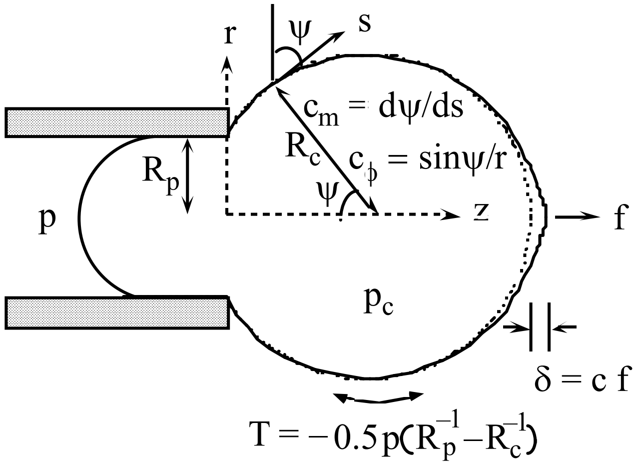

Figure 3.3: Geometries and coordinate system of a micropipette aspirated RBC under a point load at the apex.

Two principle stretch ratios are defined along the m and ϕ coordinate lines as λ_m and λ_ϕ and T is the isotropic prestressed tension in the RBC membrane, see Equations 3-12 and 3-13. The reference configuration is defined in a prestressed state rather than the stress-free state so that when the area dilation vanishes, the mean membrane tension is equal to the prestress tension rather than zero. The binding rigidity is defined as B and the binding moments in the principle directions are defined as M_m and M_ϕ.

$$\lambda_m = 1/(R_c c_m) \tag{3-12}$$

$$\lambda_\phi = 1/(R_c c_\phi) \tag{3-13}$$

Under the previous definitions, the following constitutive equations are used to relate the in-plane tensions and bending moments to the stretch ratios and curvatures:

$$\tau_m = T + K(\lambda_m \lambda_\phi - 1) + \frac{\mu}{2}(\lambda_m^2 - \lambda_\phi^2) \tag{3-14}$$

$$\tau_\phi = T + K(\lambda_m \lambda_\phi - 1) - \frac{\mu}{2}(\lambda_m^2 - \lambda_\phi^2) \tag{3-15}$$

$$M_m = M_\phi = B\left(c_m + c_\phi - 2R_c^{-1}\right) \tag{3-16}$$

In the finite difference analysis, the equations are discritized into segments along the membrane and the polar region is essentially treated as cone. The resolution of the apex cone section is controlled by increasing or decreasing the number of segments used in the analysis. The red cell was broken into inside and outside pipette sections. The outside section of the membrane was assumed symmetric about the maximum change in radius, R_c, as shown in Figure 3.4. Note that the z location of R_c is different in the loaded versus unloaded RBC.

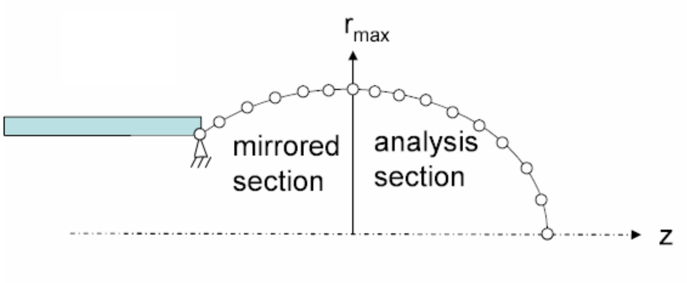

Figure 3.4: Geometries and coordinate system of the finite difference solution method to a micropipette aspirated RBC under a point load at the apex.

Two boundary conditions are imposed on the solution:

$$\Psi = \pi/2 \quad \text{at } R_{c,\max} \tag{3-17}$$

$$\Psi = 0 \quad \text{at } R_c = 0 \tag{3-18}$$

In addition, the solution imposed both area and volume conservations upon the geometry. The deformation of the red cell is converted into a finite difference problem by sectioning the red cell problem into a series of sections across the *z* axis and taking a Taylor series expansion of constitutive equation. The initial guess for the problem solution was the initial undeformed condition. Each solution imposed a force to the apex of the red cell and solved the constitute equations to achieve equilibrium. From each of these solutions the spring constant of the red cell could then be back calculated. Because the size of the cone segment at the problem apex is critical to the solution and the shape at the apex is a function of the imposed force, the number of segments in the solution is dependent upon the imposed force. The overall solution is joined together as a function of each unique solution at each imposed force. As such there is an expected small nonlinearity when the solutions are joined as a result in the error tolerance at each numerical solution. This non-linearity due to the error tolerance is expected to be small.

CHAPTER 4

RESULTS

This thesis completes two specific aims or goals. Two papers (Chesla et al. 1998 and 2000) address these aims in detail; in both papers I was the lead author with extensive contributions. During the course of this research, I also explored other directions and gathered initial data. These directions were further explored by other researchers and are presented here and also appear in publications where I am a coauthor. Nagaragjan et al. 1995, presents data confirming the ability of CHO cells to phagocytosis immune complexes on the single cell level via fluorescent microscopy. This is an important contribution to immunology as it presents a cellular model for the study of signal transduction via CD16 isoforms. Zhu et al. 2002 presents data supporting the measurement of single receptor/ligand bonds via micropipette. This is important because biophysical research has recently focused on the resolution of kinetic rates, lifetimes and rupture forces at the signal bond level. Huang et al. 2004 presents data that introduces the effect of receptor/ligand orientation and/or length on the measure kinetic rates. This is important because these parameters are often overlooked in biophysical analysis and their quantification here illustrates their significance in the determination of solid phase kinetic rates.

Quantification Of Receptor And LigandS urface Densities

The quantification of surface densities of CD16a expressed on CHO cells and IgG coated on RBC is illustrated in Figure 4.1. Figure 4.1*a* shows the results of one of the radioimmunoassays (Scatchard plot) used to quantify the receptor density. Figure 4.1*b* shows the receptor expression in samples of the same CHO cells measured by flow cytometry with calibration beads. As can be seen in Figure 4.1*c*, the receptor densities determined via the two methods are comparable. Flow cytometric analysis was solely used to determine the ligand densities on RBCs (Figure 4.1*d*)

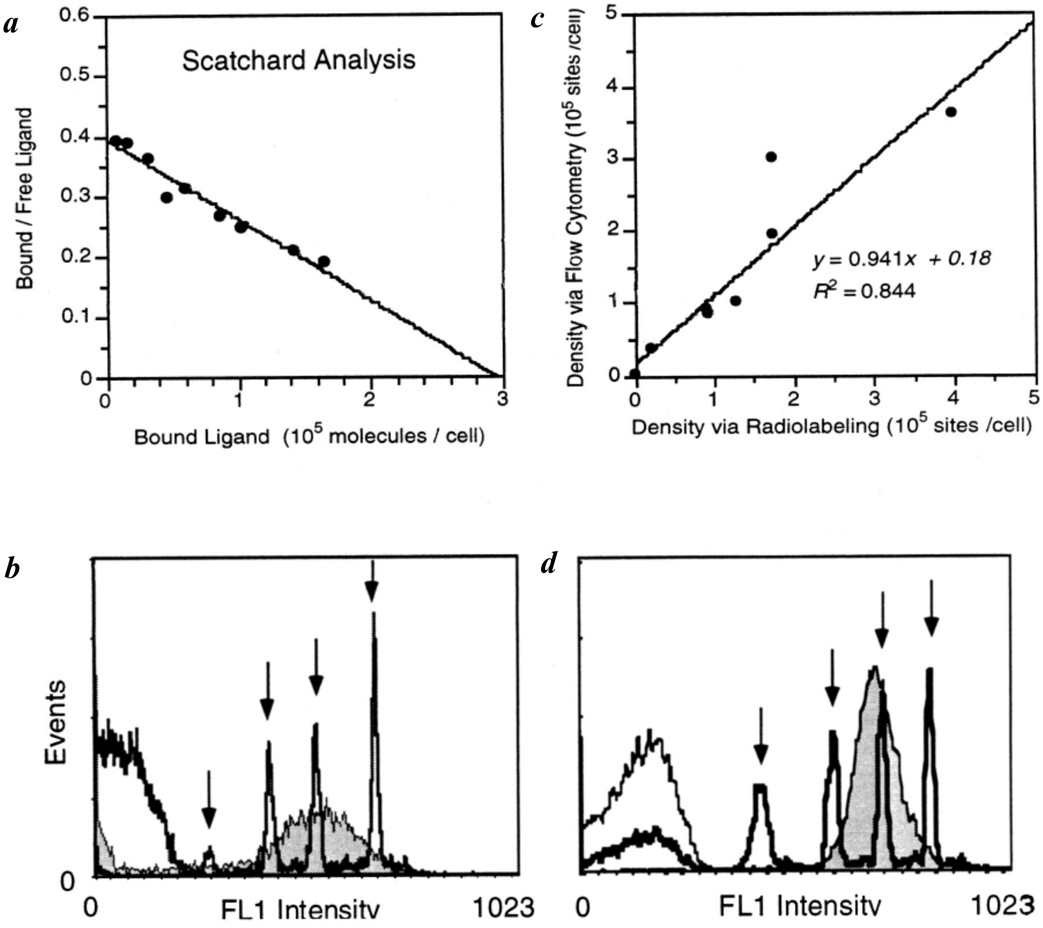

Figure 4.1: Quantification of molecular density on the cell surface. (*a*) The radioimmunoassay method involves radiolabeling specific antibodies and determining its density by counting the amount of antibody bound to the cell surface as it varies with the concentration of antibodies added in the solution. The *x* intercept of the Bound/Free versus Free line in the Scatchard plot predicts the total number of receptors per cell, (*b*) The flow cytometer method is similar, except that the cell labeling is accomplished in a two-step process with the fluorescent secondary antibody. The distributed fluorescent intensity of the CD16a+ cells (shaded curve) is then compared to those of the standard calibration beads (four unshaded curves, arrows). The negative control (without primary antibody) (unshaded curve near origin) is shown for comparison. (*c*) Comparison between receptor densities determined by the two methods, using sorted CHO cells expressing various narrow levels of CD16a (points). A strong correlation can be seen from the linear fit of the data. (*d*) Determination of IgG site density on RBCs, as in (*b*).

Measurement Of TheA dhesion Probability

The measurement of adhesion probability per contact is illustrated in Figure 4.2, in which the running averages (adhesion frequency) of the binary adhesion scores (one if adhesion results, and zero if not) for sequential adhesion tests are plotted against the test cycle count. Not only was the same pair of cells used in each set of repeated tests, but the location, area, and duration of all of the contacts in the same sequence were also kept constant by the experimenter. Thus the fluctuations in the running frequencies, especially at low test cycle counts, were most likely due to the randomness inherent to small system kinetics of receptor-ligand binding. The running adhesion frequencies became stabilized as the test number increased, allowing the adhesion probability, P_a, to be estimated from the adhesion frequency (see Fig. 4.2 legend). To ensure statistically stable results, at least 400 repeated tests were conducted for each data point, using multiple cell pairs. A total of ~7250 single cell pair adhesion tests were performed to yield the data presented here

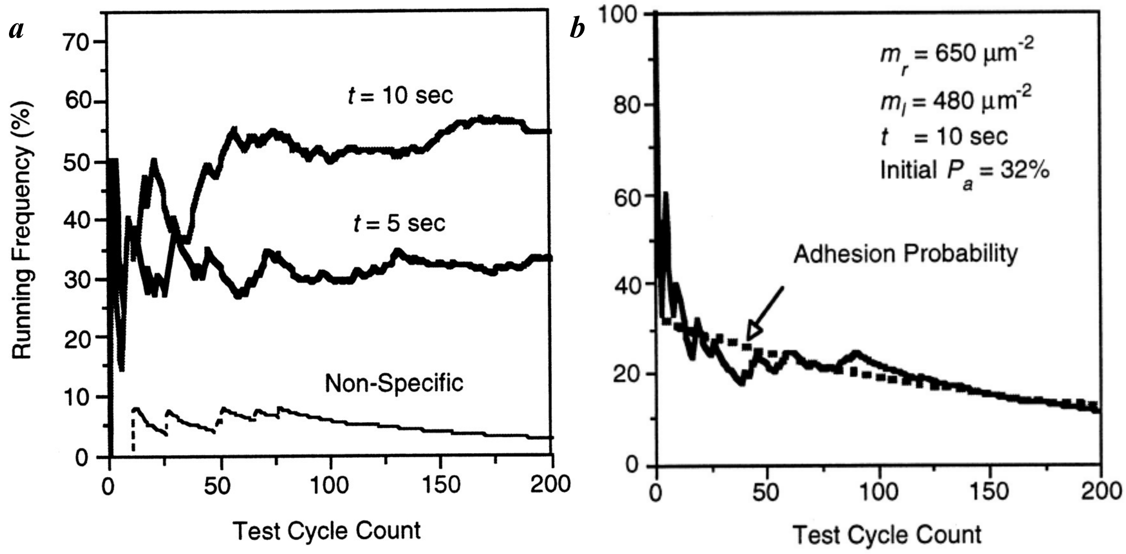

Figure 4.2: Measurement of adhesion probability per contact. (*a*) The running averages of adhesion scores versus test cycle counts of three sequences of 200 adhesion tests each, each performed in a single cell pair of a CD16a-expressing CHO cell (m_r = 650 µm^{-2}) interacting with a RBC coated with either human IgG (m_l = 1200 µm^{-2}, solid curves) or BSA (dashed curve). The apparent contact area was kept constant (~3 µm^2) for all tests. The contact durations were t = 5 s for the BSA (nonspecific) and one of the hIgG-coated test series and t = 10 s for the other hIgG-coated series, as indicated. The adhesion probability for each cell pair was estimated from the running adhesion frequency at the last adhesion test (54% and 35% for CD16-hIgG, 10- and 5-s contact durations, respectively, and 3% for CD16-BSA, 5-s contact time). The specificity of the adhesions is seen from the dependence of adhesion probability on the presence of hIgG on the RBC surface. The feasibility of measuring adhesion kinetics is revealed from the dependence of adhesion probability on contact time. The stability of the running adhesion frequency after 50 test cycles is an indication of its adhesive detachment mechanism (receptor-ligand dissociation). (*b*) Illustration of another type of running adhesion frequency (solid curve), this time declining with increasing test cycle counts, which suggests a cohesive detachment mechanism (molecular extraction from the cell membrane). This type of irreversible behavior was found when the coated ligand was a specific antibody against the receptor (anti-CD16 mAb Leu-11b). The adhesion probability (dotted curve), determined by fitting of the entire running adhesion frequency curve to a Markov process model, decreases with the test cycle count, suggesting the gradual loss of functioning adhesion molecules in the contact area. Its extrapolated initial value before the first test (32%) can be used for the purposes of the present method.

Demonstration Of Binding Specificity

Also shown in Figure 4.2 is the fact that coating an irrelevant protein (BSA) instead of the ligands on the RBCs resulted in a dramatic decrease in the adhesion probability. The binding specificity is further demonstrated in Figure 4.3, which summarizes the results of experiments designed to address this question. As can be seen under the same contact duration (5 seconds) and apparent area (3 μm^2), hIgG-coated RBCs adhered with high probability to CHO cells transfected to express CD16a, but not to untransfected parental CHO cells (K1) or to CHO cells (A5) transfected with an irrelevant receptor (integrin $\alpha_{IIb}\beta_3$). Moreover, CD16a-expressing CHO cells did not adhere to uncoated RBCs or RBCs coated with an irrelevant protein (BSA). In addition, the adhesion probabilities were reduced to the nonspecific level of binding when the CD16a-expressing CHO cells were preincubated with the adhesion-blocking anti-CD16 monoclonal antibody (mAb) (CLB at 10 µg/ml), or when the hIgG-coated RBCs were preincubated with a soluble CD16a molecule (Fig. 4.3*b*). By contrast, preincubation of the CD16a-expressing CHO cells with an irrelevant mAb (X63) or of the hIgG-coated RBCs with an irrelevant soluble molecule (B7) had no effect (Chesla, Li, Nagarajan, Selvaraj, Zhu (2000)). These data established that the measured cell adhesions were mediated by the specific interactions between CD16a and hIgG.

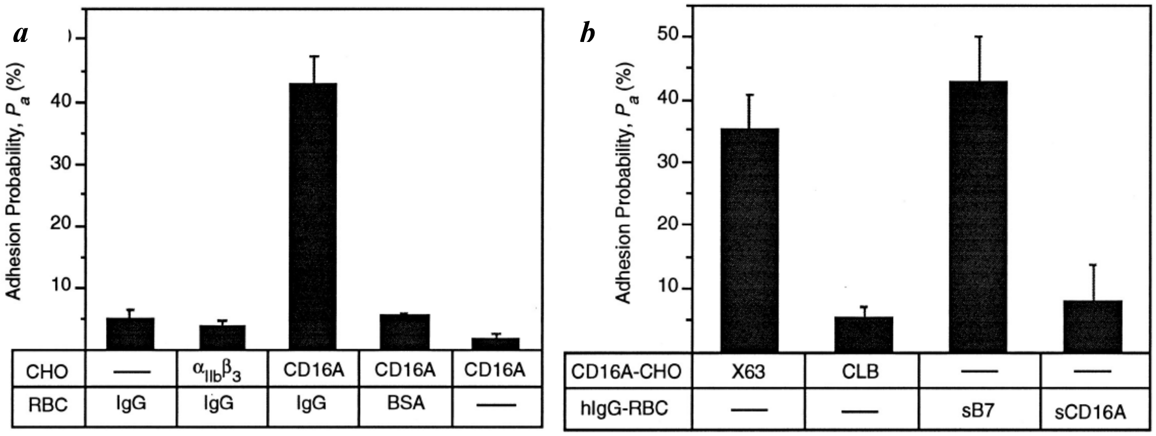

Figure 4.3: Demonstration of binding specificity. (*a*) The adhesion probability varied with the molecular combinations present or absent on the apposing cell surfaces. When CD16a was expressed on the CHO cell and the RBC was coated with hIgG, a high adhesion probability (45%) was observed. In contrast, when either no receptor (−) or an irrelevant receptor ($\alpha_{IIb}\beta_3$) was expressed on the CHO cell, low adhesion probabilities (5% and 4%, respectively) were observed for the same hIgG coating on the RBC. Similarly, when no ligand (-) or an irrelevant protein (BSA) coated the RBC, the adhesion probability was reduced to low levels (6% and 2%, respectively) for the same CD16a-expressing CHO cells. (*b*) The adhesion could also be inhibited by incubating the cells with blocking agents. The addition of the conditioned medium of hybridoma secreting anti-CD16 mAb CLB (contained ~10 μg/ml antibody) reduced the adhesion probability to 5%. Similarly, the addition of the conditioned medium of soluble CD16A-secreting CHO cells (contained ~10 μg/ml sCD16A) decreased the adhesion probability to 8%. In contrast, conditioned media of hybridoma secreting an irrelevant mAb X63 and of CHO cells secreting an irrelevant soluble molecule B7 had no effect on the overall adhesion probability (35% and 42%, respectively). Each of the bars in A and B represents mean ± standard error of data from two to four series of 50-200 tests, each at a contact duration of 5 s.

Dependence Of Adhesion Probability On Contact Duration

It can also be seen in Figure 4.2 that, when the contact times in a test sequence were prolonged from 5 to 10 s, the adhesion probability was increased. The dependence of P_a on t was systematically measured; the results (after subtracting the nonspecific binding) are shown in Figure 4.4. As expected, the adhesion probability increased with increasing contact duration initially and then reached a plateau. The initial transient phase contains information about kinetic rates, whereas the equilibrium association constant can be derived from the steady state. Furthermore, for fixed contact durations, P_a increased with both the densities of the receptor and the ligand, as expected from the law of mass action.

Because $P_a(t) = 1 - p_0(t)$ is also solved from the master equations, comparing the measured and the predicted dependence of adhesion probability on contact time allows us to evaluate the kinetic rates. However, rate constants so calculated represent intrinsic properties if and only if the correct kinetic mechanism, i.e., the realistic order of the reaction, is assumed in Eq. 3-3. To identify the appropriate kinetic mechanism, the ability of the theory to account for the experiment was compared with the different stoichiometric coefficients assumed

Determination Of The Kinetic Mechanism

We first examine the order of dissociation. The Poisson type of simplified master equations was used to address this question, because the valences of the receptor and the ligand, v_r and v_l, need not be specified for such a case, as they are lumped into one of the two curve-fitting parameters, $A_c m_r^{v_r} m_l^{v_l} k_f^0$ and $A_c^{1-\nu_b} k_r^0$. The equations were solved for various ν_b values, and the errors between the predictions and the data were minimized by adjusting the lumped rate parameters for each of the four P_a versus t curves in Figure 4.4. The minimum χ^2 (averaged over four curves) is plotted in Figure 4.5*a* against the ν_b value. It appears that the reverse reaction is of the first order, as this mechanism ($\nu_b = 1$) is best able to reproduce the data (i.e., results in the lowest χ^2).

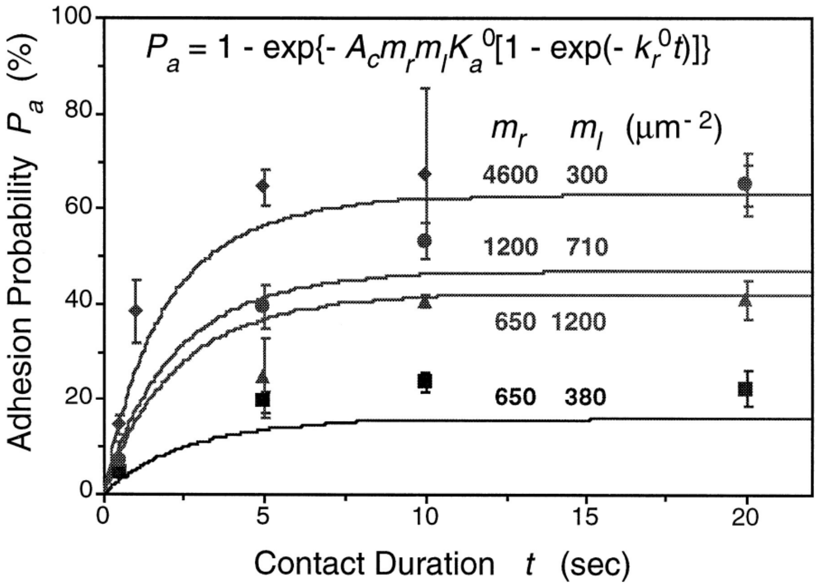

Figure 4.4: Dependence of adhesion probability on contact time and receptor/ligand densities. The total adhesion probability (P_t) was converted into the probability of specific adhesion $P_a = (P_t - P_n)/(1 - P_n)$, where the probability of nonspecific adhesion P_n was P_t at $m_l = 0$, i.e., measured with BSA-coated RBC), plotted as a function of the contact duration for each set of receptor and ligand densities, and fitted with the indicated theoretical solution (curves). A single set of kinetic rate constants (listed in Table 4-1) was used to fit all data corresponding to four different pairs of (m_r, m_l) values (indicated). The data (points) represent mean ± standard error of two to five series of tests of at least 50 each to yield at least 400 total tests per data point.

The above conclusion that the CD16a-hIgG interaction obeys first-order dissociation greatly facilitated the remaining investigation for the kinetic mechanism, as the closed-form solution, Eq. 3-6, can now be applied to the data analysis. Not only is this handy to use, but it also suggests informative ways of presenting the data for hypothesis testing. It follows from Eq. 3-6 that

$$\ln[\ln(1 - P_a)^{-1}] = v_r \ln m_r + v_l \ln m_l + \ln\{A_c K_a^0[1 - \exp(-k_r^0 t)]\} \tag{4-1}$$

Thus, in $\ln[\ln(1 - P_a)^{-1}]$ versus ln m_l (or ln m_r) plots, the data should appear as linear for each fixed t and m_r (or m_l), and the slope of the line should be the valence of the ligand, ν_l (or the receptor, ν_r). To test this argument, the two sets of P_a versus t data shown in Figure 4.4 that correspond to the same m_r (= 652 μm^{-2}) were replotted in Figure 4.6*a* as

$\ln[\ln(1 - P_a)^{-1}]$ versus $\ln m_l$ for various t. It can be seen that, as the contact time changes, the y intercept of the $\ln[\ln(1 - P_a)^{-1}]$ versus $\ln m_l$ line shifts, but its slope remains nearly the same (= 0.86 for the average of four constant time lines). Because ν_l can only take positive integer values, the data suggest that hIgG is a monovalent ligand for CD16a

We can now use the conclusion of $\nu_l = 1$ to subtract the term involving the ligand on the right-hand side of Eq. 4-1. This allowed us to plot $\ln[\ln(1 - P_a)^{-1}] - \ln m_l$ versus $\ln m_r$ in Figure 4.6*b*, using all four sets of P_a versus t data. It is evident that, for each fixed contact time, the data appear to line up in a straight line with a slope of approximately unity. Not only does this indicate the monovalency of CD16a binding; it also supports the validity of the present method for determining the kinetic mechanism. Further support of this argument is provided in Fig. 4.5*b* in which the minimum χ^2 is plotted against ν_r and ν_l. A single set of kinetic rates, $A_c k_f^0$ and k_r^0, were used to fit all P_a versus t data for each pair of ν_r and ν_l values for all admissible ν_b [$\leq \min(\nu_r, \nu_l)$] values. Again, the bimolecular binding mechanism between a single epitope on CD16a and a single binding site on the Fc domain of hIgG ($\nu_r = \nu_l = 1$) was bound to be best able to describe the data. This conclusion further supports the first-order dissociation mechanism, as ν_b cannot be greater than the smaller of ν_r and ν_l.

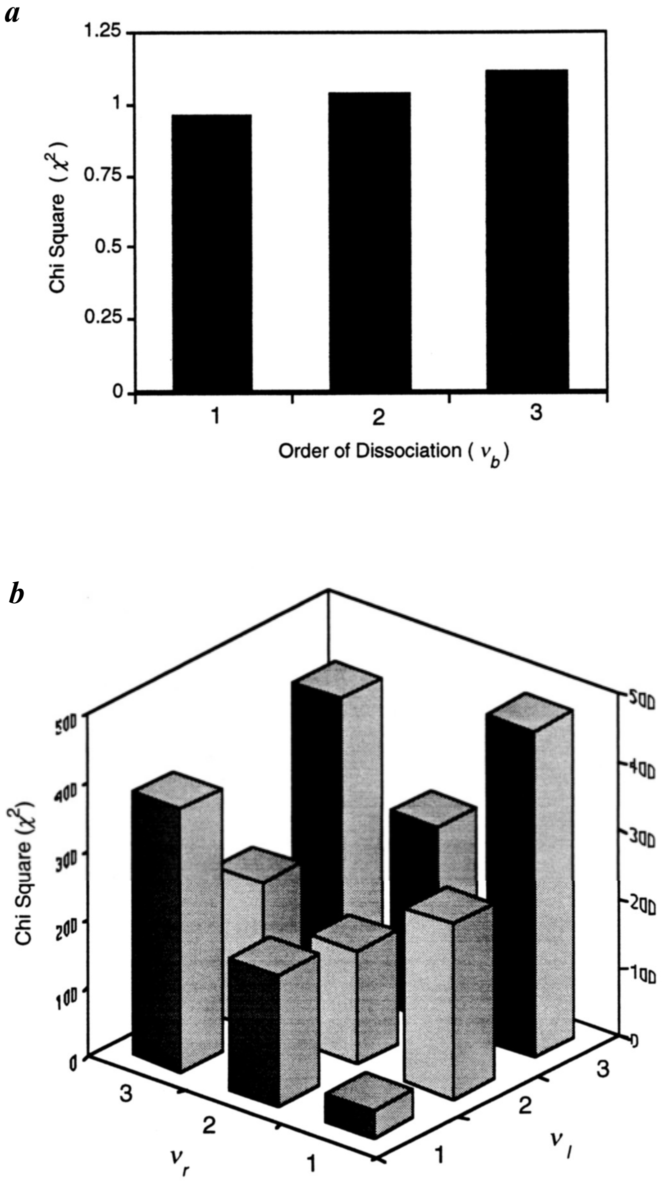

Figure 4.5: Comparison of the abilities of various kinetic mechanisms to account for the data. (*a*) The solutions of the Poisson-type master equations with various orders of dissociation (ν_b) were fitted separately to each of the four sets of P_a versus t data from Fig. 4.4. The sum of squared weighted errors (χ^2) from all of the curves was averaged and plotted against the ν_b value. (*b*) The four sets of data from Fig. 4.4 were simultaneously fitted by the solutions of the full master equations (Eq.3-3), with various stoichiometric coefficients, ν_b, ν_r, and ν_l. The minimum χ^2 was calculated as a function of ν_r and ν_l. At each pair of (ν_r, ν_l) values, the lowest χ^2 for all admissible ν_b ($\leq \min(\nu_r, \nu_l)$) values was plotted (bars).

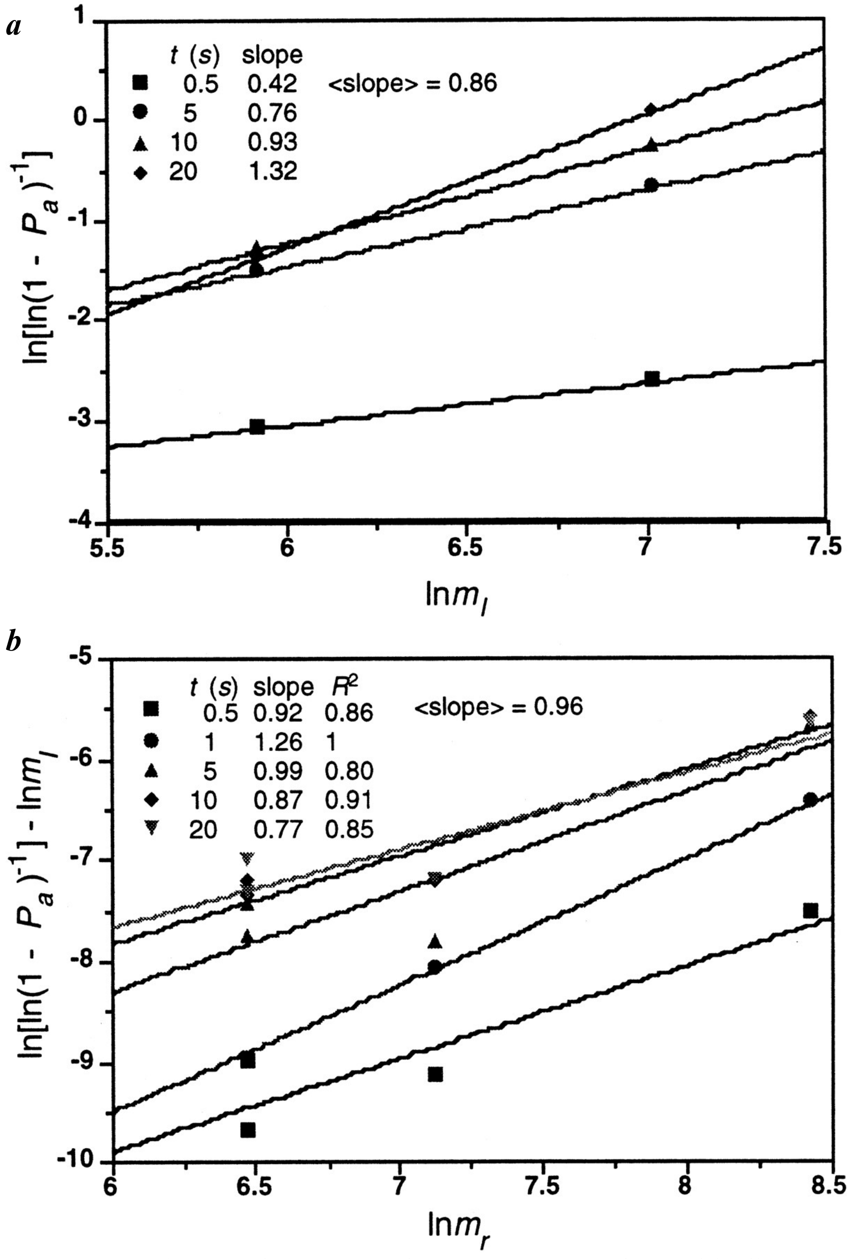

Figure 4.6: Demonstration of the monovalency of CD16a-hIgG binding. (*a*) The two P_a versus t curves from Fig. 4.4 that correspond to the same receptor expression level (m_r = 650 μm^{-2}) but different ligand coating densities (m_l = 380 and 1200 μm^{-2}) were replotted as $\ln[\ln(1 - P_a)^{-1}]$ versus $\ln m_l$ data (points) for each contact duration t (indicated) and fitted with a linear function (lines). The nearest integer of the slopes of these lines (indicated) is predicted to be the most probable value of ν_l, which is 1. (*b*) All curves were replotted as $\ln[\ln(1 - P_a)^{-1}] - \ln m_l$ versus $\ln m_r$ data (points) for each contact duration t (indicated) and fitted with a linear function (lines) with the goodness of fit indicated by the R^2 value. The nearest integer of the slopes of these lines (indicated) is predicted to be the most probable value of ν_b, which again is unity.

Validating The Theoretical Predictions And Evaluating The Kinetic Rate Constants

It follows from Equation 4.1 that, when $\nu_r = \nu_l = 1$ and for a fixed value of t, $\ln(1 - P_a)^{-1}$ should increase bilinearly with m_r and m_l. The slope of the $\ln(1 - P_a)^{-1}$ versus $m_r \times m_l$ line should be equal to $A_cK_a^0[1 - \exp(-k_r^0t)]$. These predictions were tested in Figure 4.7 and were found to be well supported by the data. Minimizing the errors between the predicted and measured slope versus contact time relationship (Fig. 4.7*b*) makes it possible to evaluate the binding affinity (per contact area), $A_cK_a^0$, and the reverse rate constant, k_r^0. To test the accuracy and reliability of these values, the kinetic rate constants were also calculated using each P_a versus t curve in Fig. 4.4 for various m_r and m_l levels, as well as fitting all of the data simultaneously (Table 4-1). Conversely, the k_f^0 and k_r^0 values evaluated from the fitting of one P_a versus t curve were then used to predict other P_a versus t curves obtained from independent experiments using different levels of m_r and m_l (not shown). The ability of the model to use only a single pair of rate constants to fit a wide range of data, including five time points and four ligand and three receptor densities, not only attests to the validity of the method employed, but also suggests that the estimated parameters are indeed intrinsic molecular properties.

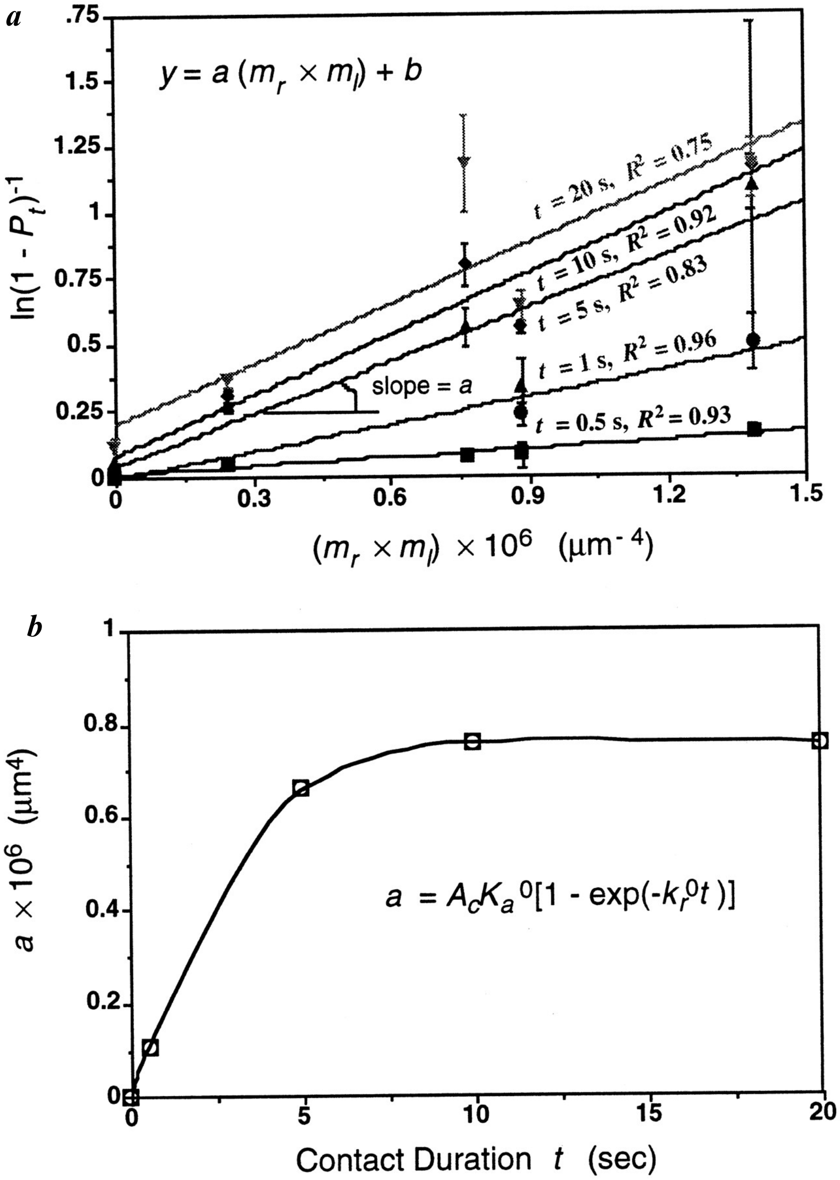

Figure 4.7: Further demonstration of the bimolecular kinetic mechanism. (*a*) The probability of total adhesion P_t versus the product of surface densities ($m_r \times m_l$) of CD16a and hIgG is shown in a semi log plot ($P_t \approx \ln(1 - P_t)^{-1}$ for small P_t). For each contact duration t (indicated), the data (points) were fitted with a linear function (lines), and the goodness of fit was indicated by the R^2 value. The error bars were computed from the original data according to the Gaussian error propagation law. (*b*) The slopes of the individual lines from (*a*) were plotted against t and fitted with the indicated equation. The ability of the theoretical model to fit the data well in both panels is another indication that the proper kinetic mechanism is being assumed, i.e., $v_r = v_l = v_b = 1$.

Additional support for the theory was found when it was tested for the predicted functional form of the adhesion probability, i.e., that all P_a versus t data for the same receptor-ligand pair should collapse into a single $(m_r m_l)^{-1}\ln(1 - P_a)^{-1}$ versus t curve, regardless of the densities of the receptors and ligands (Figure 4.8). The four P_a versus t curves shown in Figure 4.4 did indeed collapse in Figure 4.8. When the origin of the IgG ligands was changed from human to rabbit, the $(m_r m_l)^{-1}\ln(1 - P_a)^{-1}$ versus t curve shifted, indicating different kinetic rate constants for different molecular pairs. Indeed, human CD16a binds twice as rapidly to, but dissociates half as rapidly from, RbIgG than hIgG, leading to a fourfold difference in affinity (Table 4-1), which is consistent with the affinity difference measured when the IgGs were in solution (i.e., 3-D affinity).

Table 4-1: Summary of kinetic rate constants

IgG origin	m_r (µm^{-2})	m_l (µm^{-2})	$A_c k_f^0 \times 10^7$ (µm^4 s^{-1})	k_r^0 (s^{-1})	$A_c K_a^0 \times 10^6$ (µm^4)
Human	650	380	4.0 ± 1.5	0.36 ± 0.16	1.1
Human	650	1200	1.9 ± 3.7	0.13 ± 0.06	1.4
Human	1200	710	2.5 ± 0.94	0.42 ± 0.18	0.59
Human	4600	300	2.9 ± 0.52	0.35 ± 0.09	0.82
Human	Combined data		2.6 ± 0.32	0.37 ± 0.06	0.72
Rabbit	1200	190	6.0 ± 0.42	0.25 ± 0.07	2.4
Rabbit	1200	360	5.2 ± 0.49	0.16 ± 0.05	3.3
Rabbit	Combined data		5.7 ± 0.31	0.20 ± 0.04	2.8

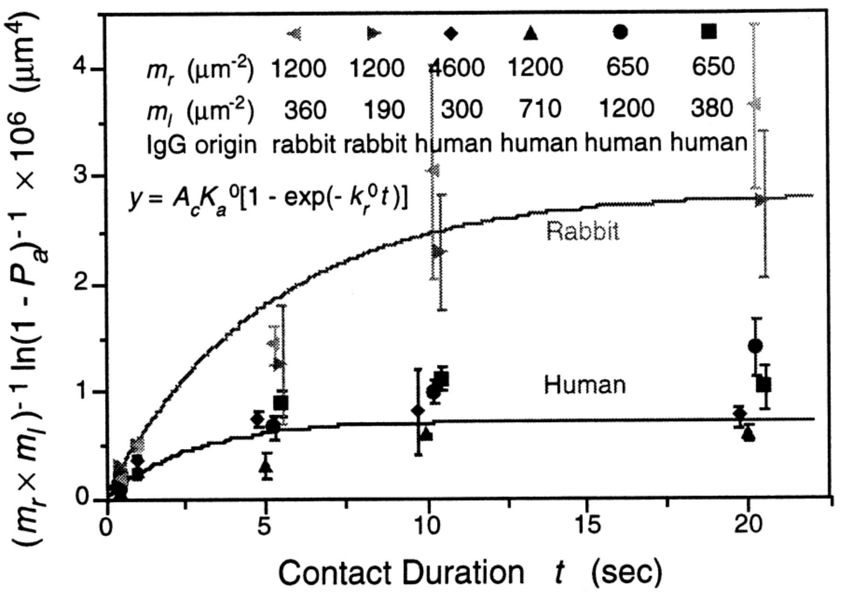

Figure 4.8: Validation of the functional form of the theoretical prediction. Data (points) from Figure 4.4 (hIgG group) plus those measured for IgG from a different species (rabbit) were converted into a logarithmic scale, divided by ($m_r \times m_l$), plotted against t, and fitted with the indicated equation (curves). The theoretical solution predicts that, for the same receptor-ligand pair, data measured using different m_r and m_l values (indicated) should collapse into a single curve in this plot. Thus the difference in the two data groups reveals different kinetic rate constants for CD16a binding IgG of different origins (human and rabbit). As such, a single set of $A_ck_f^0$ and k_r^0 (Table 4-2) was used to fit multiple data curves for the same receptor and ligand pair (CD16a-hIgG or CD16a-RbIgG). The error bars were computed from the original data, using the Gaussian error propagation law. Adhesions were measured at t = 0.5, 1, 5, 10 and 20 s. However, not all data were plotted at the exact time points, to avoid symbol overlap.

A Simple Graphic Representation

A simple graphic representation for estimation of the kinetic rates from the adhesion probability versus contact time data without using χ^2 fitting of nonlinear curves is also available. The value of $A_cK_a^0$ can be estimated directly from the slope of the $\ln[1 - P_a(\infty)]^{-1}$ versus m_rm_l plot, where $P_a(\infty)$ is the steady-state value of the adhesion probability. This has been exemplified in Figure 4.7 (the 10- and 20-s lines in Fig. 4.7*a* or the corresponding points in Figure 4.7*b*). Similarly, the value for the reverse rate constant can be estimated directly from the time, t_{50}, that is required for the P_a versus t data to achieve half-maximum,

$$k_r^0 = \frac{\ln 2}{t_{50}} C(A_c m_r m_l K_a^0) \tag{4-2 a}$$

where C varies between 0 and 1; and its weak dependence on $A_c m_r m_l K_a^0$ can be derived from Equation 3-6:

$$C = \frac{1}{\ln 2} \ln\left(1 + \{\ln[1 + \exp(-A_c m_r m_l K_a^0)] - \ln 2\}/(A_c m_r m_l K_a^0)\right)^{-1} \tag{4-2 b}$$

As can be seen from Figure 4.9, for the values of $A_c m_r m_l K_a^0$ encountered in the present work (Table 4-1), C only varies between 0.7 and 0.9. Thus,

$$k_r^0 \approx t_{50}^{-1} \times 50\% \tag{4-2 c}$$

Above, the kinetic rates and binding affinity of the CD16a-IgG interaction using the developed micropipette method were quantitated. Additionally the question may be asked whether the membrane anchor (including the associated subunits) itself had any influence on these intrinsic binding parameters. The mechanisms that might cause such differences are also of interest. These questions are a natural progression of the initial research that I began at Georgia Tech: 1) by using existing radiographic protocols, I determined whether binding affinity differences exist between CD16a-TM and CD16b-GPI to soluble hIgG and RbIgG, and 2) I determined the debonding force characteristics of IgG to CD16a using existing micropipette protocols and the methodology developed to determine the 2D kinetic rates of cellular adhesion.

To answer the above questions, additional data was needed with different combinations of CD16 anchored molecules and different IgG molecules exhibiting different affinities. The different CD16 anchoring mechanisms are depicted in Figure 2.5. The data reported above was collected using the CD16a-TM isoform with its interaction with hIgG. To determine the effect of the anchoring mechanism on CD16 rates and affinity, first additional data was gathered using the CD16a-GPI isoform, again using hIgG as the ligand. Next the rates and affinity were determined for both CD16a-TM and CD16a-GPI for interactions with RbIgG and mIgG2a (Chesla, Li, Nagarajan, Selvaraj, Zhu (2000)).

The data shows that, in comparison to CD16a-TM, CD16a-GPI bound with faster forward rates and higher affinities to hIgG and rabbit IgG (RbIgG) but with a slower forward rate and a lower affinity to mIgG2a. Thus, the membrane anchor of CD16 influenced its ligand binding kinetic rates and affinity, and the qualitative trend of such an effect was inverted when the ligand was changed. Furthermore, this effect exhibited the same pattern regardless whether binding was measured with membrane-bound ligands using the micropipette method or with fluid-phase ligands via competitive inhibition. The findings that the anchor effect flipped with different ligands and that the same results were observed in both two-dimensional and three-dimensional studies are important. They enable the following six possible mechanisms for the membrane anchor effect to be ruled out: differing lateral diffusivity, rotational flexibility, molecular orientation, binding site height, surface distribution, and functional clustering of the two molecules. Furthermore, no major differential glycosylation between the two CD16a isoforms was found by SDS-PAGE analysis (Chesla, Li, Nagarajan, Selvaraj, Zhu (2000)). The hypothesis is that there is a conformational difference between the two CD16a isoforms that causes the observed anchor effects. This proposed mechanism is also supported by a finding that whereas an anti-CD16 monoclonal antibody (mAb) bound with higher affinity for CD16a-GPI than CD16a-TM, another mAb reacted strongly with CD16a-TM but only weakly with CD16a-GPI, suggesting that an antigenic epitope was down-regulated after the membrane anchor of CD16a had been changed from TM to GPI (Chesla, Li, Nagarajan, Selvaraj, Zhu (2000)).

The structural segments of cell surface receptors consist of distinct domains as follows: a glycosylated extracellular domain linked to either a transmembrane (TM) domain with a cytoplasmic tail or to a glycosylphosphatidylinositol (GPI) moiety without TM and cytoplasmic domains (Cross (1987), Low (1987)). The anchor can influence the function of a receptor. TM anchors of some receptors carry information for protein internalization and subunit association, whereas those of other receptors transduce signals (Klausner *et* al. (1990), Lanier *et* al. (1990)). The GPI moiety consists of a glycan core sandwiched between ethanolamine and a lipid tail. Ethanolamine is covalently attached to the carboxyl terminus of the protein by an amide bond, whereas the lipid tail directly inserts into the outer leaflet of the membrane but does not cross the bilayer (Ferfguson et al. (1988)). The GPI anchor has been implicated in facilitating the lateral mobility of the protein on the cell surface (Zhang et al. (1991)) and enhancing receptor-mediated cell adhesion (Chan et al. (1991), Tozeren et al. (1992)).

As presented in Chapter 2, there are four known eukaryotic receptors that naturally exist in both membrane anchor isoforms as follows: neural cell adhesion molecule, lymphocyte function-associated antigen 3, vascular cell adhesion molecule 1, and Fcγ receptor III (FcγRIII or CD16). The physiological significance of this coexistence of two distinct membrane anchor isoforms for the same receptor is not clear. As such, a comparison of the 2D to 3D kinetic rates and binding affinities for TM-anchored FcγRIIIa versus GPI-anchored FcγRIIIb is relevant and significant.

The Two-Dimensional Kinetic Rates Depended On The CD16 Membrane Anchor And This Dependence Varied with Ligand

The micropipette method quantifies the dependence of adhesion probability on contact time and densities of the receptors and ligands, as exemplified in Figure 4.4. To allow for direct visual comparison of the kinetic rates and binding affinity, the mass action effect, manifesting itself in Figure 4.4 as an upward or downward shifting of the curves depending on the receptor and ligand densities (m_r and m_l), must be eliminated. This is achieved by a simple transformation of Equation 4-1 (with monovalent coefficients) into Equation 4-3.

$$y \equiv (m_r m_l)^{-1} \ln(1-P_a)^{-1} = A_c K_a [1 - \exp(-k_r t)] \tag{4-3}$$

It is evident that the far right-hand side of Equation 4-3 depends only on the binding affinity (K_a) and the reverse rate constant (k_r) of the interacting molecules, provided that the contact area (A_c) is kept constant, as in the present study. Thus, this transformation collapses a family of P_a *versus* t curves for the same receptor-ligand pair into a single curve on the transformed ordinate. Only when different interacting molecules are tested will the transformed binding curves shift, allowing for a direct visualization of the distinct K_a and k_r values.

The transformed binding curves are shown in Figure 4.9 for each of the two human CD16a isoforms interacting with IgG from each of the three species. It is evident from Figure 4.9*a* that for hIgG the CD16a-GPI binding curve achieved a >2-fold higher level than the CD16a-TM binding curve at steady state (contact time $t > 10$ s). To test further this result, two additional ligands, IgGs from rabbit and murine, were examined, since they were known to interact well with human CD16. A similar trend was obtained when RbIgG was tested (Figure 4.9*b*). When mIgG2a was tested, however, an inverted result was observed. The CD16a-TM binding curve reached a ~7-fold higher equilibrium level than the CD16-GPI curve (Chesla, Li, Nagarajan, Selvaraj, Zhu (2000)). The plateau level of the transformed binding curve provides a direct measure for the binding affinity because the far right-hand side of Equation 4-3 approaches A_cK_a as t approaches infinity.

The values for the reverse rate constant can also be visually compared from the transformed binding curves. It follows from Equation 4-3 that k_r is equal to ln2 divided by the time required for the curve to reach half-maximum, $t_{1/2}$, as shown in Equation 4-4.

$$k_r \approx 0.7/t_{1/2} \tag{4-4}$$

From the data shown in Figure 4.9, the $t_{1/2}$ values appear to be comparable for the two CD16a isoforms interacting with the same IgG species, suggesting their similar reverse rate constants.

Whereas the transformation given by Equation 4-3 makes the effect of the membrane anchor on kinetic rates and binding affinity readily visible without analysis, fitting Equation 4-3 to the data (Figure 4.9) allows for quantitative evaluation of k_f, k_r, and

K_a. The values of these two-dimensional kinetic properties are presented in Table 4-2, which quantitatively confirm the visual observations.

Table 4-2: Summary of two-dimensional CD16a-IgG kinetic rates and affinities.

CD16a	IgG	$A_c k_f$	k_r	$A_c K_a$
		$10^{-6}\ \mu m^4\ s^{-1}$	s^{-1}	$10^{-6}\ \mu m^4$
TM	hIgG	0.25 ± 0.11	0.34 ± 0.05	0.74 ± 0.3
GPI	hIgG	0.77 ± 0.29	0.42 ± 0.02	1.8 ± 0.7
TM	RbIgG	0.58 ± 0.05	0.24 ± 0.02	2.4 ± 0.1
GPI	RbIgG	0.70 ± 0.09	0.17 ± 0.02	4.1 ± 0.2
TM	mIgG2a	2.4 ± 0.26	0.31 ± 0.02	7.6 ± 0.7
GPI	mIgG2a	0.59 ± 0.27	0.54 ± 0.03	1.1 ± 0.5

Thus, the micropipette data revealed the membrane anchor of CD16a as a major determinant of its kinetic properties; it altered the forward, but not the reverse, rate constant and thereby also altered the binding affinity. Significantly, this effect varied with the ligand species, with the GPI-anchored CD16a having higher affinity for hIgG and RbIgG but lower affinity for mIgG2a than its TM-anchored counterpart. This "flipping" phenomenon is interesting and may be useful in understanding the underlying mechanism

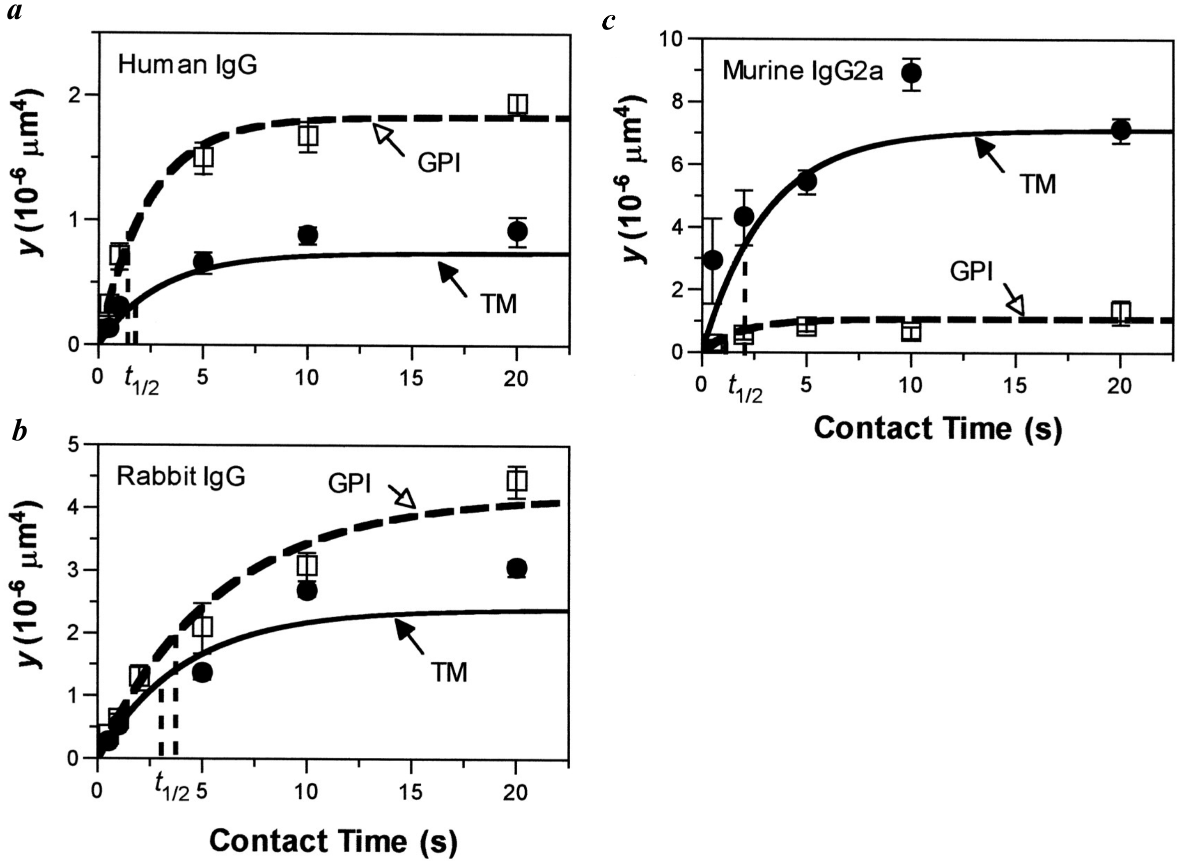

Figure 4.9: Transformed binding curves of CD16a-TM and CD16a-GPI-expressing CHO cells interacting with red blood cells coated with IgGs from human (*a*) and rabbit (*b*), *and mouse (c)*. The adhesion probability data, exemplified in Figure 4.4, were transformed according to Equation 4-3 (the logarithm of the reciprocal of 1 - P_a was taken and divided by m_r and m_l) and then plotted against the contact time t. By normalizing the ordinate with respect to m_r and m_l, the family of curves corresponding to the same pair of interacting molecules but different densities of receptors and ligands collapse. Furthermore, the dependence of binding affinity K_a and reverse rate k_r on molecular identity becomes apparent. The higher plateau level indicates a greater K_a; and a shorter half-time ($t_{1/2}$, indicated) reflects a faster k_r. The theoretical predictions (Equation 4.3, curves) were fit to each data set (points, mean ± S.E.) to evaluate the K_a and k_r values, which are listed in Table 4.2. The number of cell pairs examined was 43, 17, 20, 22, 11, and 12 for the CD16a-TM-hIgG, CD16a-GPI-hIgG, CD16a-TM RbIgG, CD16a-GPI-RbIgG, CD16a-TM-mIgG2a, and CD16a-GPI-mIgG2a curves, respectively. Each cell pair was repeatedly tested 50-200 times to obtain a stable adhesion probability estimate.

The CD16 Membrane Anchor Effect On Binding Affinity And Its Ligand Dependence Was Also Found In Three-dimensional Binding Studies

The preceding section represents the first application of the developed micropipette method for determining two-dimensional kinetic rates in a comparative study of the ligand-binding property of a cell surface receptor. Although this method has been carefully validated (Chesla et al. (1998)), it is important to further verify it by comparing its predictions with those derived from more established methodologies. For this reason, three-dimensional binding studies were conducted to address the following questions. Was the CD16 membrane anchor effect on ligand binding seen in Figure 4.9 a true indication of the structure-function relationship of the interacting molecules, a real reflection of the two-dimensional experimental conditions, or a mere artifact of the micropipette method?

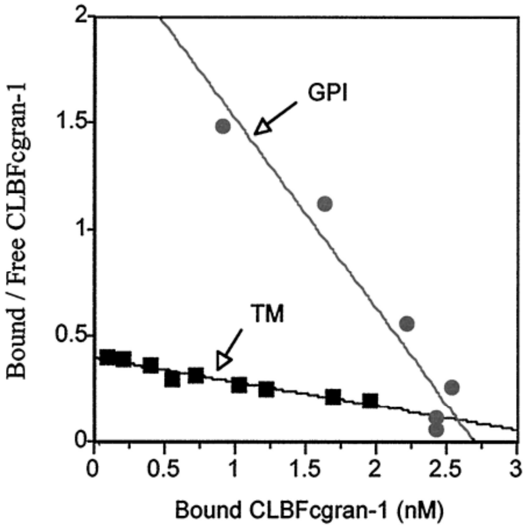

Figure 4.10: Scatchard analyses of binding of ^{125}I-labeled CLBFcgran 1 Fab to CHO cell transfectants expressing CD16a-TM (squares) and CD16a-GPI (circles). Points are experimental data, and the solid lines are least square linear fits to the two data sets. The slope of each line equals the negative of the three-dimensional binding affinity, K_a, whereas the x intercept provides a measure for the receptor density. The results shown are representative. The mean and S.D. of all measured values are listed in Table 4-3.

The affinities of an anti-CD16 mAb CLBFcgran-1 in fluid-phase for both CD16a-TM and CD16-GPI on CHO cells were first determined by Scatchard analysis (Figure 4.10). The membrane anchor effect (in this case using the Fab fragment of CLBFcgran-1 as ligand) again is apparent in Figure 4.10, with the GPI-anchored CD16a exhibiting a higher affinity than the TM-anchored CD16a. Because CD16 is a low affinity receptor for monomeric IgG, measuring CD16-IgG interactions by the Scatchard method is rather difficult and results so obtained may not be reliable.

A competitive inhibition protocol using nonlinear curve-fitting based on Equation 3-1 was therefore adapted. Representative data comparing the two human CD16a membrane anchor isoforms are presented in Figure 4.11*a, b, and c* using hIgG, RIgG, and mIgG2a respectively (Chesla, Li, Nagarajan, Selvaraj, Zhu (2000)). It is evident from Figure 4.11*a* and *b,* that CD16a-GPI had higher affinities than CD16a-TM for hIgG and RbIgG, as the same ligand concentration inhibited the CLBFcgran-1 binding to a greater extent. The fact that CLBFcgran-1 bound with a higher affinity to CD16a-GPI than CD16a-TM (Figure 4.11) should lead to less, rather than more (as was the case), inhibition by hIgG or RbIgG. The situation using mIgG2a is different. Using mIgG2a the *lower curve* corresponds to CD16a-TM, which has a lower affinity than CD16a-GPI for CLBFcgran-1. Hence it would be easier to be inhibited even if mIgG2a were to bind both CD16a membrane isoforms with the same affinity. However, fitting Equation 3-1 to the data revealed that CD16a-TM indeed had a higher affinity than CD16a-GPI for mIgG2a, as was in the two-dimensional case. The three-dimensional affinity results are summarized in Table 4-3

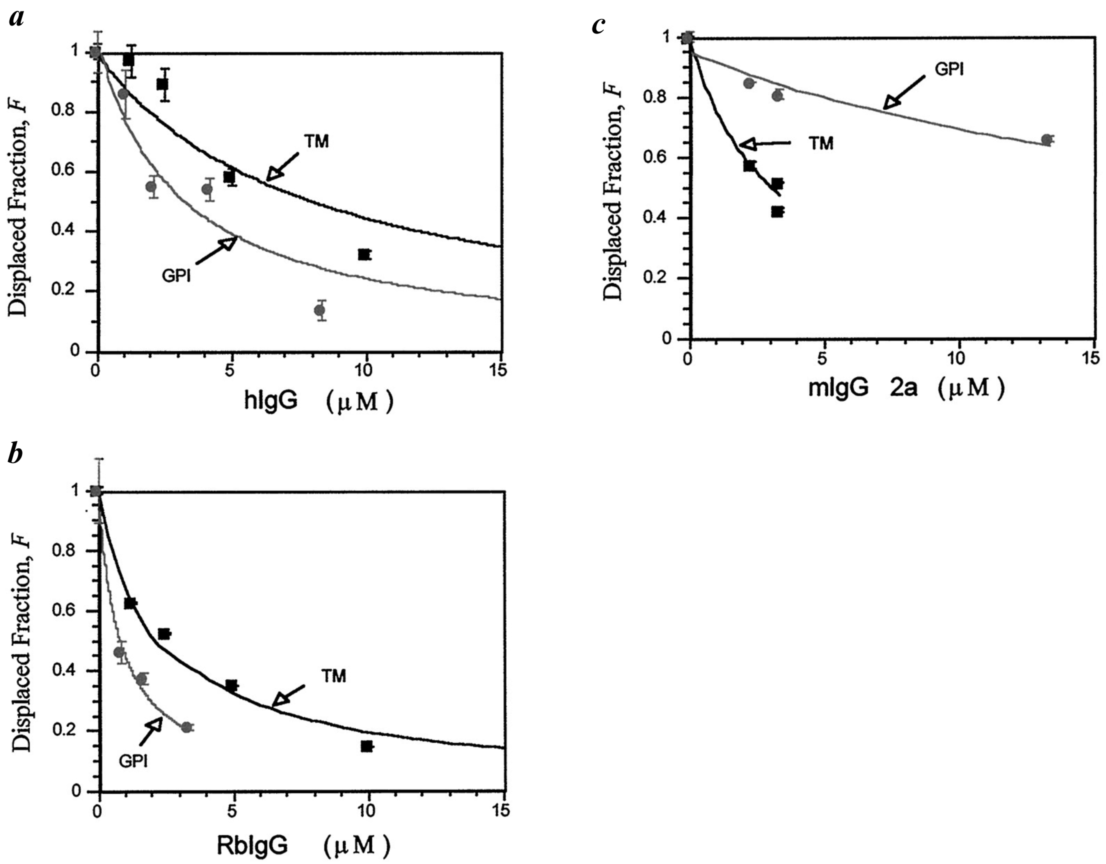

Figure 4.11: Competitive inhibition curves for determining the binding affinities of CD16a-TM and CD16a-GPI for IgG of three species. CHO cells expressing CD16a membrane isoforms were allowed to bind ^{125}I-labeled CLBFcgran-1 Fab in the presence of varying concentrations of hIgG (*a*), RbIgG (*b*) or mIgG2a (c). Points are data presented as mean ± S.D. of triplicate wells, whereas each curve is a χ^2 fit to that set of data using Equation 3-1. The mean and S.D. of the K_a values of each ligand to both CD16a-TM and CD16a-GPI are listed in Table 4.3.

Table 4-3: Summary of three-dimensional CD16-ligand affinities.

Receptor	CLBFcgran-1	hIgG	RbIgG	mIgG2a
	$10^8\ M^{-1}$		$10^6\ M^{-1}$	
CD16a-TM	1.0 ± 0.2 (4)	0.25 ± 0.09 (5)	0.93 ± 0.17 (3)	0.41 ± 0.03 (2)
CD16a-GPI	5.4 ± 0.2 (7)	2.1 ± 0.31 (3)	6.3 ± 0.9 (3)	0.11 ± 0.01 (2)
CD16a-γ	0.97 ± 0.25 (2)	0.40 ± 0.1 (2)	0.57 ± 0.1 (2)	0.66 ± 0.1 (2)
CD16a-ζ	0.61 ± 0.23 (2)	0.34 ± 0.1 (2)	0.80 ± 0.17 (2)	0.47 ± 0.21 (2)
CD16b^{NA1}	1.5 ± 0.2 (2)	0.032 ± 0.01 (3)	0.033 ± 0.004 (3)	ND
CD16b^{NA2}	0.83 ± 0.4 (2)	0.019 ± 0.004 (3)	0.028 ± 0.01 (3)	ND

This work elucidates the how the receptor anchor mechanism can influence kinetic rates; compared with CD16a-TM, CD16a-GPI bound faster and with higher affinities to human and rabbit IgGs but slower and with lower affinity to murine IgG2a. The same differential affinity patterns were observed using soluble IgG ligands. A monoclonal antibody bound CD16a-GPI with higher affinity than CD16a-TM, whereas another monoclonal antibody reacted strongly with CD16a-TM but weakly with CD16a-GPI. No major differential glycosylation between the two CD16a isoforms was detected by SDS-polyacrylamide gel electrophoresis analysis. The hypothesis is that a conformational difference is the mechanism underlying the observed anchor effect, as it cannot be explained by the differing diffusivity, flexibility, orientation, height, distribution, or clustering of the two molecules on the cell membrane. These data demonstrate that a covalent modification of an Ig super family receptor at the carboxyl terminus of the ectodomain can have an impact on ligand binding kinetics (Chesla, Li, Nagarajan, Selvaraj, Zhu (2000)).

Effect Of LigandO rientation And Availability

During the course of data acquisition to complete the specific aims of this thesis, it was also observed that ligand orientation has a dramatic effect on the kinetic parameters calculated using the developed system. Again, observation of these ligand orientation effects was a natural progression from the work previously presented. This section will examine how the surface presentation of adhesion receptors influences cell adhesion. The micropipette adhesion frequency assay was used to quantify how the molecular orientation of adhesion receptors on the cell membrane affected two-dimensional kinetic rates of interactions with surface ligands. Interactions of CD16a with the respective ligands or antibody were used to demonstrate such effects. Randomizing the orientation of the adhesion receptor lowered two-dimensional affinities of the molecular interactions by reducing the forward rates but not the reverse rates. In contrast, to the ligand orientation effects on two dimensional binding properties, the soluble antibody bound with similar three-dimensional affinities regardless of their orientation.

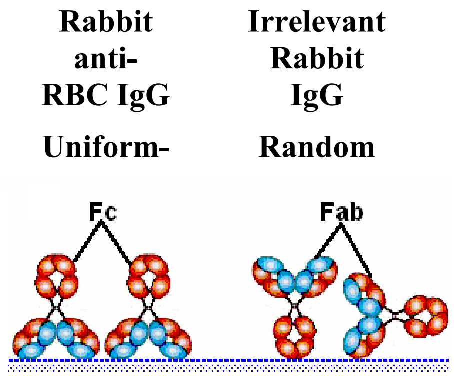

Figure 4.12: Schematics of rabbit anti-human RBC IgG that was oriented uniformly via binding to RBCs or irrelevant RbIgG was oriented randomly by coupling via $CrCl_3$.

These results demonstrate that the orientation of an adhesion receptor influences its rate of encountering and binding a surface ligand but does not subsequently affect the stability of binding. The different RbIgG orientations are described in Figure 4.12. The three dimensional binding characteristics of RbIgG are presented in Table 4-3. The non-specific RbIgG was used to determine this 3D affinity. The 3D affinity of the anti-RBC RbIgG to CD16a is assumed identical as the molecular differences in the RbIgG molecule are in the Fc region away from the binding mediating Fc portion.

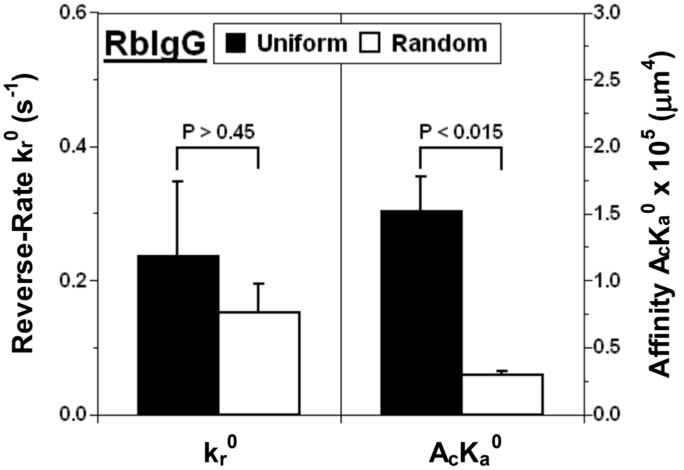

Figure 4.13: 2D kinetic reverse-rates and effective affinities of CD16a for uniformly or randomly oriented RbIgG. Adhesion experiments were performed using two sets of receptor and ligand densities for each orientation: $m_r \times m_l = 1200 \times 40$ and 240×40 μm^{-4} for uniformly captured RbIgG and 240×190 and 1200×360 μm^{-4} for randomly coupled RbIgG, respectively. The reverse rates, k_r^0, and effective binding affinities, $A_cK_a^0$, for CHO cell CD16a interacting with uniformly (solid bars) and randomly (open bars) oriented RbIgG were obtained by fitting.

Measuring Extraction Probability Of Receptors From The Cell Membrane

Previous micropipette protocols mainly focused on the resolution of detachment force from the observed deflection in the red cell membrane. The interpretation of the micropipette force data requires the knowledge regarding the detachment mode, i.e., via dissociation at the receptor-ligand binding site or via extraction at the membrane anchor of either the receptor or the ligand, as both detachment modes may require similar levels of force. Observation of these detachment mode effects was also a natural progression from the work previously presented. During the course of this thesis, a quantitative method to address the question of detachment mode was developed. The key observations were the two qualitatively distinct features seen when a large number of repeated adhesion tests were performed sequentially on the same contact area using a single pair of cells. One of these, characterized by a uniform distribution of adhesion events amongst all tests and a stable running frequency, may be called reversible binding (Figure 4.14*a*). It is suggestive of dissociation of the receptor-ligand bonds; and this behavior was seen when the receptor-ligand interaction was of low affinity (3D $K_d \sim$ μM, referred to as a weak bond). The other of these, characterized by a concentration of adhesion events near early tests and a declining running frequency, may be called irreversible binding (Figure 4.14*b*). It is indicative of disruption of the membrane anchor of either the receptor or the ligand; and this behavior was seen when the receptor-ligand interaction was of high affinity (3D $K_d \sim$ nM, referred to as a strong bond). To quantitatively measure the likelihood of molecular extraction I, a Markov model was constructed for the statistical analysis of the running adhesion frequency, P_a, (Figure 4.14).

$$P_a = 1 - \frac{1}{i}\sum_{j=1}^{i} \exp\{- A_c m_r m_l K_a^0(1 - e^{-k_r^0 t})[1 - I m_{\max} K_a^0(1 - e^{-k_r^0 t})]^{j-1}\} \qquad (4\text{-}5)$$

where i is the cycle number in the repeated adhesion tests, $m_{\max} = \max(m_r, m_l)$. When $I = 0$, Eq. 4-5 reduces to Eq. 4-6.

$$P_a = 1 - \exp\{- A_c m_r m_l K_a^0 [1 - \exp(-k_r^0 t)]\} \qquad (4\text{-}6)$$

Comparisons between the expected and measured running adhesion frequency vs test cycle count curves are shown in Figures 4.14*a* and *b*, for the reversible (low I) and irreversible (high I) cases, respectively. Figure 4.14*c* shows the systematic determination of the extraction probability for TM- or GPI-CD16a interacting with either a natural ligand, hIgG, or a mAb directed against CD16 (Lue-11). Here the extraction probability, I, was determined by a χ^2 error minimization of the data using equation 4-5 as a model. As expected, when the receptor-ligand bond was strong (i.e., of high affinity), it was more likely to uproot the molecule from the cell membrane. Similarly, when the receptor membrane anchor was strong (i.e., TM-linked), it was less likely to be extracted if extraction was to occur. By comparison, if the extraction was unlikely, as in the weak bond case, the anchor strength had no effect. These data demonstrate our ability to determine the detachment mode, required for the proper interpretation of the force data.

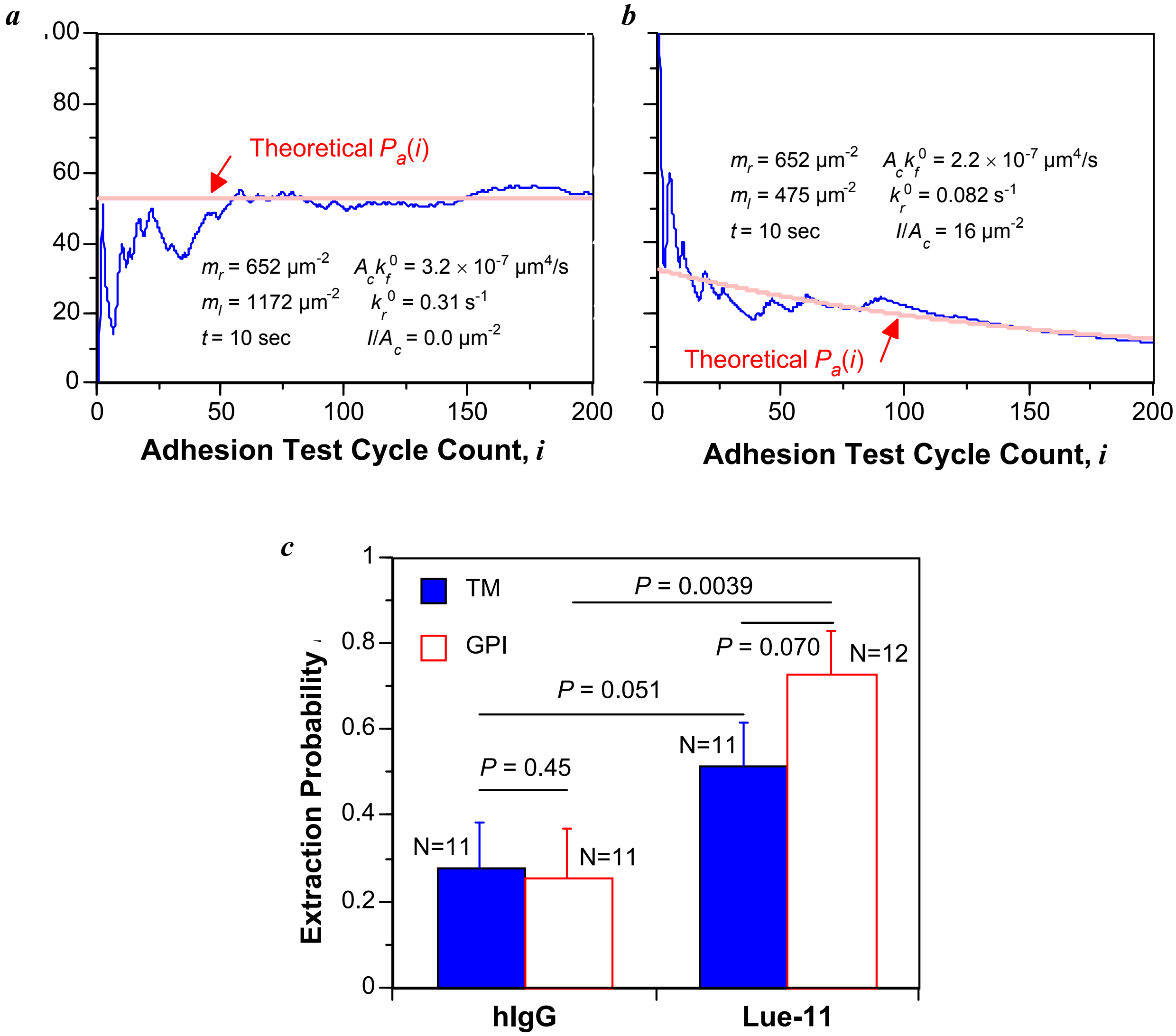

Figure 4.14: Running frequency vs adhesion test cycle count curves for reversible (*a*) and irreversible (*b*) binding between CD16a-TM expressing CHO cells interacting with RBC coated with hIgG (a) or anti-CD16 mAb Lue-11 (*b*). Summary data (mean ± standard error) for the extraction probability, I, for four cases of strong (TM) or weak (GPI) anchored CD16a forming strong (Lue-11) or weak (hIgG) bonds with ligands. Also indicated are the sample sizes and the P values from the student t test.

Micropipet Force Determination Precision

The detachment force was extracted from the CD16-IgG reactions observed using the method described in Chapter 3. In addition to the detachment force, an estimate of the micropipette systems precision was also calculated. The precision assessment first required the determination of the force-deflection relationship using a finite difference method. Analytical solutions (via perturbation and linearization) to the membranes mechanics problem are also available in our lab and can be compared to the finite difference computational solution.

Each of the techniques shows good agreement in their solutions. The greatest difference in the predicted membrane shape under a point load occurs at the apex of the cell. The deformed shape near the apex of the aspirated RBC predicted from each of the three solution techniques is plotted in Figure 4.15. The linearized solution shows the greatest propensity toward cone formation. This may be interpreted as the solution whose contribution from the binding rigidity is the smallest. The computational and perturbation techniques show good agreement especially in the shape of the cell apex.

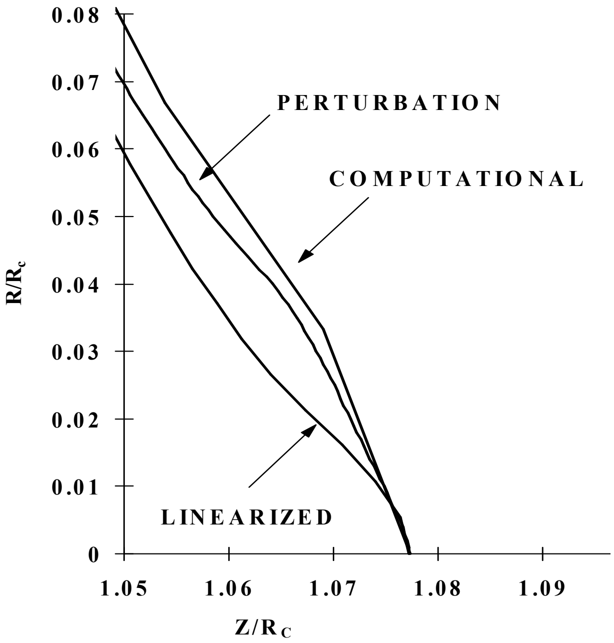

Figure 4.15: Magnified non-dimensional view of the RBC apex loaded by a point force. The linearized solution shows the greatest propensity toward cone formation. This may be interpreted as the solution whose contribution from the binding rigidity is the smallest. The computational and perturbation techniques show good agreement especially in the shape of the cell apex.

The force versus deflection relationship predicted from each analysis under similar conditions are shown in Figure 4.16*a* in nondimensional form and shows good agreement. Agreement is close between the computational and linearized solutions. This contrasts the results at the cell tip and illustrates that the majority of the cell deformation in the z direction occurs away from the tip.

The RBC transducer compliance coefficients are plotted in Figure 4.16*b* against the deflection. This plot illustrates the assumed linearity of both analytic solutions; however, the nonlinearity of the problem is clearly evident in the computational solution. This plot extends a detection limit at the lower end.

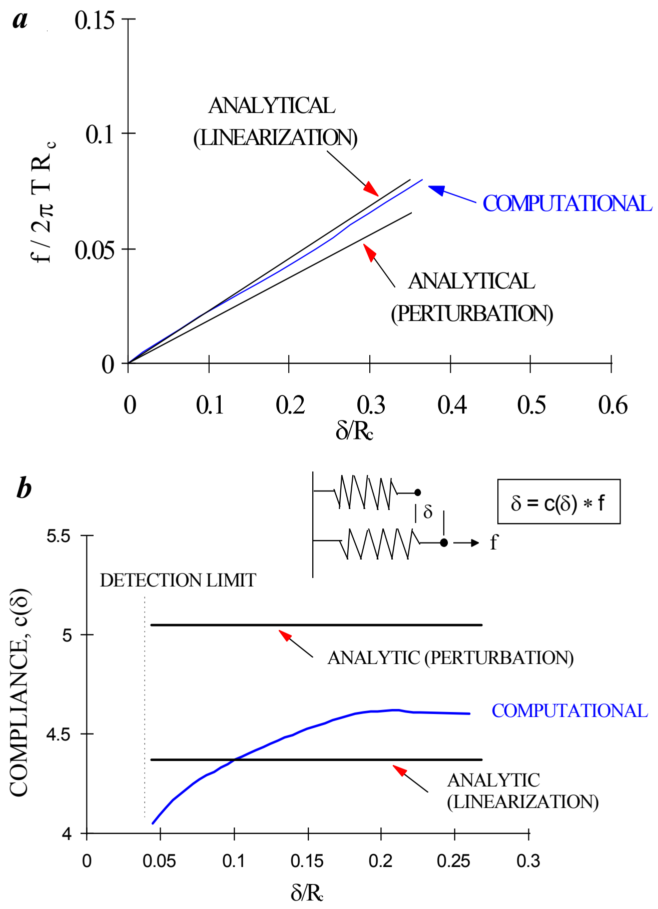

Figure 4.16: (*a*) Force versus deflection relationship of the three different solutions to the RBC membrane mechanics equations. (*b*) The compliance coefficient of each solution plotted versus deflection.

Although all solutions to the membrane equations show good agreement, the validity of the analyses has not yet been demonstrated. Accordingly, an experiment was devised to load an aspirated RBC transducer with a known force in order to calibrate its deflection. The experimental set up illustrated in Figure 4.17 and 4.18 utilizes a fully aspirated RBC that acts as a force imposing piston. Leakage effects around the piston during this experiment were neglected. It has recently come to our attention that this validation was also independent performed by Yeung (1994).

Briefly a RBC's were osmotically preswollen and allowed to come in contact with a anti-RBC antibody coated bead. The RBC on the left hand side was aspirated into a smaller pipette. The geometry of the aspirated pipetteis in agreement with the geometry depicted in Figure 4.17. Simultaneously, the right hand side RBC was aspirated into a larger pipette which was matched to the RBC diameter size. This experiment was repeated on several occasions with different pipette sizes and different cell sets. The sensitivity of the left hand side pipette was tuned by controlling the left hand side suction pressure and the imposed force on the bead was controlled by controlling the right hand side suction pressure.

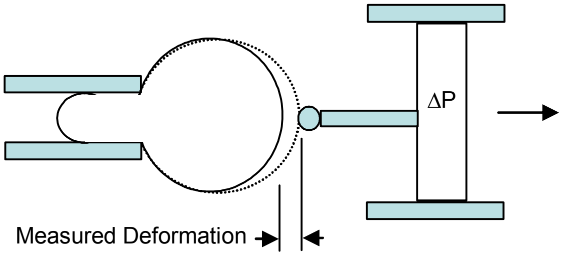

Figure 4.17: A schematic showing the force transducer arrangement used to validate the calculated spring constant of the RBC deflection models.

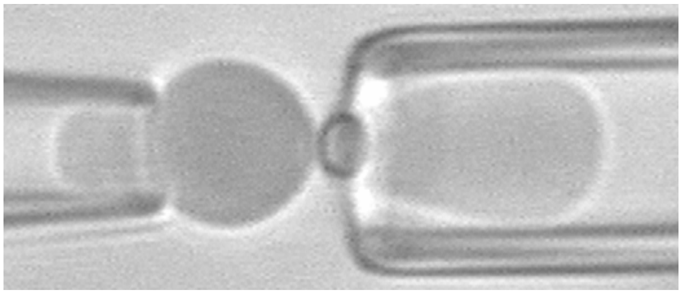

Figure 4.18: The transducer validation experiment in which a partially aspirated RBC transducer is loaded by a fully aspirated RBC piston.

Comparing a representative force versus deflection relationship predicted from computational analysis to validation data in Figure 4.19*a*, again good agreement is seen.

Figure 4.19*b* presents the error of the calculated versus measured force. As shown in equation 4-7, the measured force from the force validation experiment is heavily dependent upon the accuracy of the pressure measurement in the right hand side pipette

$$f_{measured} = \left[\Delta P r_{pipet}^{2} \pi\right] - \left[\varepsilon_{leakage}\right] \tag{4-7}$$

An accuracy of 0.05 mm H_2O is expected in the measurement of the pipette pressure. The scatter in the measured force data illustrated in Figures 4.19 reflects the accurate suction pressure reading sensitivity. The predicted standard deviation of approximately 30%, shown in Figure 4.19*b*, is derived assuming an accuracy of 0.05 mm H_20 in piston suction pressure. Taking into account the error associated with the pressure measurement, the leakage affects and minor errors in bead displacement measurement and left hand side pipette cell radius, pipette radius or pressure measurement, the agreement between the experimental system and theoretical predictions is good.

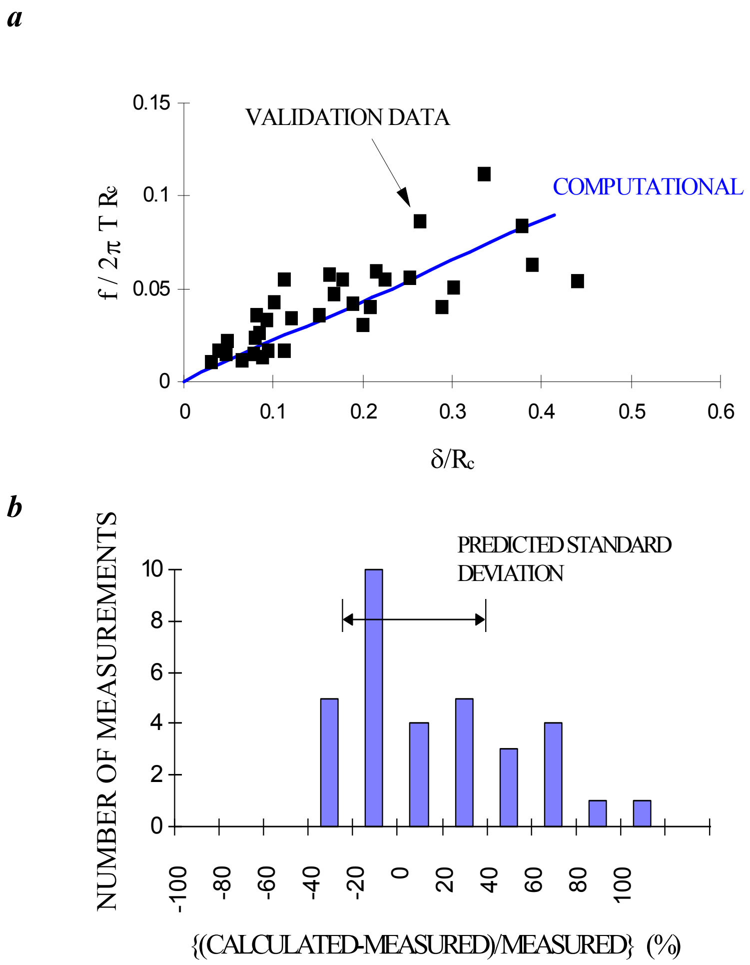

Figure 4.19: (*a*) Comparison between the predicted and measured force versus deflection relationship. (*b*) Histogram of error between the validation data and matched computational solutions. An error of 30% is expected solely as a result of suction pressure inaccuracy of 0.05mm H2O.

It has previously been illustrated that the micropipette transducer is sufficiently sensitive to make it an attractive force measurement devise; however, assessing the accuracy of the piconewton force measurement requires a summed error propagation across all independent parameters, not just the observed deflection. Random errors in the measurement of x, y, or z can lead to error in the determination of f, when f is defined in equation 4-8. Because random errors can be defined as either positive or negative errors in the measurement of x, y and z, the error associated in f is usually written as a function of $(\mathrm{d}f)^2$. Then, using equation 4-8, $(\mathrm{d}f)^2$ takes the form of equation 4-9. If the measured variables are not correlated, the cross terms average to zero, i.e., $\mathrm{d}x\, \mathrm{d}y = 0$, $\mathrm{d}y\, \mathrm{d}z = 0$, and $\mathrm{d}x\, \mathrm{d}z = 0$ because $\mathrm{d}x$, $\mathrm{d}y$, and $\mathrm{d}z$ are both positive and negative values. Then $\mathrm{d}f = (\mathrm{d}f)^{1/2}$. If the standard deviation (σ) of the measurement is assumed equal to the differentials, equation 4-10 is the error propagation formula.

$$f = f(x, y, z) \tag{4-8}$$

$$(df)^2 = \left(\frac{\partial f}{\partial x}\right)_{y,z}^2 dx^2 + \left(\frac{\partial f}{\partial y}\right)_{x,z}^2 dy^2 + \left(\frac{\partial f}{\partial z}\right)_{x,y}^2 dz^2 + \tag{4-9}$$

$$2\left(\frac{\partial f}{\partial x}\right)_{y,z}\left(\frac{\partial f}{\partial y}\right)_{x,z} dxdy + 2\left(\frac{\partial f}{\partial y}\right)_{x,z}\left(\frac{\partial f}{\partial z}\right)_{x,y} dydz + 2\left(\frac{\partial f}{\partial x}\right)_{y,z}\left(\frac{\partial f}{\partial z}\right)_{x,y} dxdz$$

$$\sigma_f = \left[\left(\frac{\partial f}{\partial x}\right)_{y,z}^2 \sigma_x^2 + \left(\frac{\partial f}{\partial y}\right)_{x,z}^2 \sigma_y^2 + \left(\frac{\partial f}{\partial z}\right)_{x,y}^2 \sigma_z^2\right]^{1/2} \tag{4-10}$$

Table 4-4 presents the accuracy in which the independent parameters can be measured in column 1. Using equation 4-10, the propagated error from the individual measurements can define the precision of the overall force measurement. The measurements of concern are the suction pressure of the aspirated RBC, the measured cell radius, the measured pipette radius, the measured RBC deformation, the bending coefficient (determined from literature) and the shear constant (determined from literature). In this analysis the suction pressure accuracy is again assumed as 0.05 mm H_2O. Because the configuration of the aspirated RBC is not in the configuration of a piston, the dependence of the force measurement on suction pressure is less critical.

Therefore, the propagated error due to accuracy in pipette suction pressure is the least of all the identified measured parameters as shown in Figure 4.20*a*. A useful purpose justifying the determination of the propagated error is in determining the principle source of measurement error and suggesting improvement in that area. Figure 4.20*a* and Table 4.-4 both indicate the major source of error in the force calculation is the deflection measurement. The measured deflection in the case of an experimental configuration according to Figure 4.17 is expected to much less then the deflection measurement of an experimental configuration according to Figure 3.3. In the experimental case of Figure 4.17, the binding is mediated by antibody bound to plastic bead. The position of the bead can be more certainly determined. In the experimental configuration depicted in Figure 3.3, the binding is mediated by receptors and ligand expressed on the surface of apposing cells. While binding measured using membrane bound molecules is more physiologic the RBC edge is less certainly determined than is a bead edge or centroid. Because the deflection measurement accounts for much the propagated error in the experimental system, thought should be given to it's optimization towards the experimental goals. Image analysis may be used to improve the accuracy of edge determination of the RBC membrane, although this step is time and cost sensitive.

Another critical measured parameter with respect to the proper determination of force in the membrane deformation model is the aspirating pipette radius. An accuracy of the pipette radius measurement of 100 μm was used in Table 4-4. This accuracy assumes that a correction is available for an apparent pipette radius measurement determined from the binding experiment images. Without correction the accuracy of the pipette radius may be as low as 250 μm and the propagated error could be more than double of its reported value in Table 4-4. The relationship used to correct from the apparent diameter to the true diameter can be developed from pipits whose radii are first determined when immersed in diH2O then in oil. Pipettes immersed in oil will produce more accurate determinations of their radii. Alternatively, the pipette radius may be determined using a scanning electron microscope then in diH2O immersion. Using these methods a relationship between the apparent and true pipette radii may be determined. The apparent pipette radius should be converted into the true radium before force calculation are attempted using the RBC membrane experimental technique.

The bending constant or binding modulus is also a critical parameter with respect to the determination of force in the membrane deformation model. The influence of the bending modulus on the force measurement error is a justification and validation of including the bending terms in the governing equations. As shown in Figure 4.20*b*, good agreement is shown between the propagated error calculated using both the theoretical and computational models. This agreement is an indication that the assumptions in each model (independent in each case) do not result in significant errors.

There is consistent agreement between the propagated errors calculated using both the analytical and computational methods for all the other parameters except the cell radius measurement which accounts for a difference between the two methods of over 600% as shown in Figure 4.20*b*. The cell radius term in the computational model tends to cancel itself out in the discritization of the problem. The theoretical solution indicates that cell radius errors can propagate significant errors to the force calculation, although less than both the pipette radius and deflection measurements. One the sources of cell radius measurement error is a band width which is visualized at typically 0.5 μm as shown in

Figure 4.21. In order to reduce random propagation of error into the force calculation, the cell radius should be consistently measured on the inside of the band. To reduce the systematic error propagation due to errors in cell radius measurement, a relationship can be constructed between the true and apparent radius using area or volume conservation experiments.

Table 4-4: Expected accuracies for the independent parameters and their influence on the overall accuracy of the force calculation for the micropipette piconewton force transducer.

PARAMETER (X_i)	ACCURACY (σ_{Xi})	Propagated Error on Force	
		Analytical (Perturbation)	Computational
Suction Pressure	0.05 mm H_2O	0.275 pN	0.23 pN
Cell Radius	0.250 μm	2.10 pN	0.27 pN
Pipet Radius	0.100 μm	2.81 pN	1.71 pN
Deformation	0.05 μm	3.31 pN	2.14 pN
Bending Constant	1E-19 J	1.50 pN	1.3 pN
Shear Constant	1E-5 N/m	----	0.26 pN
$\sigma_f = \sqrt{\sum((\partial f / \partial X_i) \times \sigma_{X_i})^2} =$		5 pN	3 pN

Examination of Table 4-4 indicates that the summation of all individual errors predicts an expected standard deviation of 3 to 5 pN out of a 40 pN calculated force. In this manner we estimate that the precision of the membrane technique for force determination is approximately 7.5 to 12.5%.

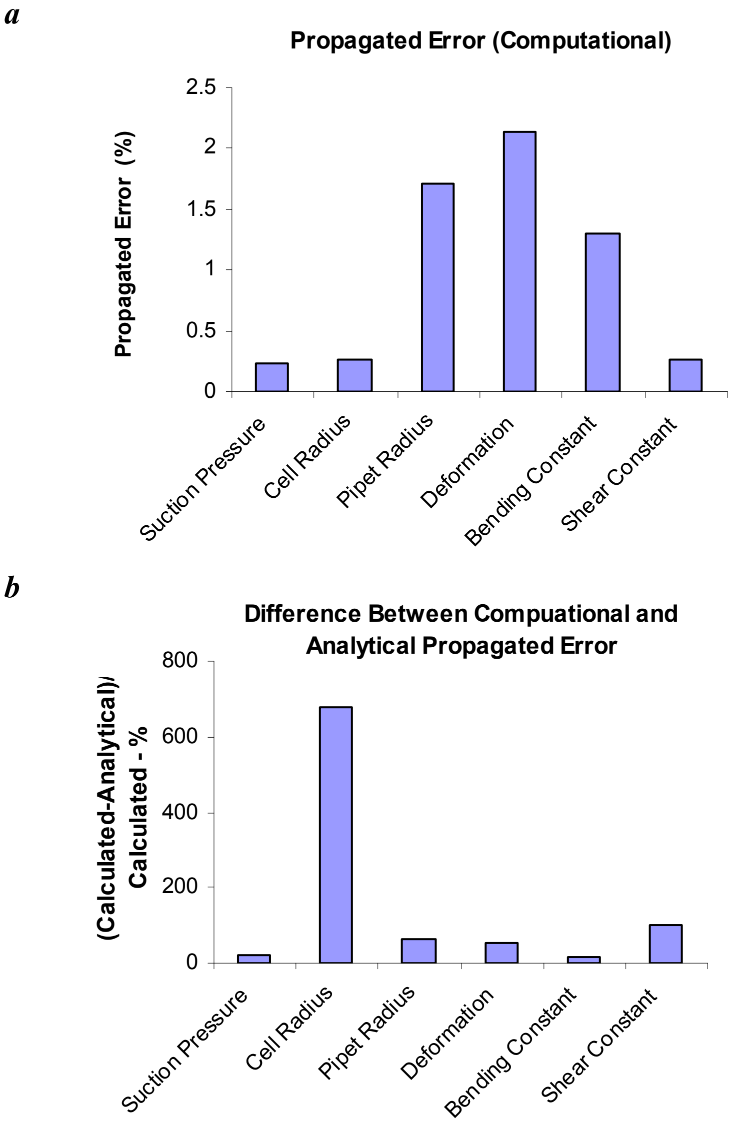

Figure 4.20: (*a*) The propagated error as determined by the method outlined in equations 22-24 using the computational model with parameters accuracies listed in Table 1. (*b*) The difference between the propagated error using the computational and theoretical models.

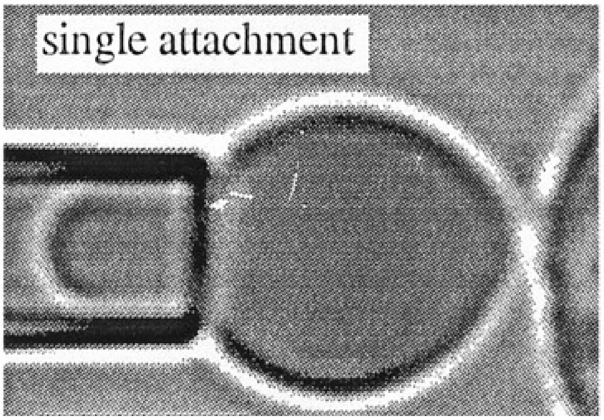

Figure 4.21: A RBC used as a force determination device. The RBC configuration does not utilize a bead to mediate binding. Although the expression of receptor and ligand within the binding area may be more physiologic and binding statistics more relevant, the determination of the red cell deformation in the z direction is less certain due to the interfering bands of each cell. Image analysis across the entire red cell membrane can increase the certainty of the red cell deformation measurement.

The sensitivity of the micropipette piconewton force transducer has made it attractive to use, but the precision of the devise has not been addressed. This work indicates that even without sophisticated image processing to improve the parameter accuracies, the expected standard deviation is small at +/- 5 pN when measuring forces in the 40 pN range. This sensitivity was achieved using both analytical and computational models of the RBC under a point load at the cell apex. Good agreement was demonstrated between the models and the assumptions imposed on the linearization of the governing equations in the analytic solutions appear validated. The propagation of error was also addressed using both the analytic and computational models. Again, good agreement was demonstrated between the error predictions.

Quantal Behavior Of Observed CD16 Binding Events

A discussion of the statistical basis for the existence of single bonds has been introduced. It is useful to recall that the developed micropipette device collects data in two modes: force and event data. Previously, a theory was developed that allows the determination kinetic rates form the event data. Here both the adhesion probability and debonding force data are gathered with the goal of presenting evidence of quantal behavior at the single bond level. This data is summarized in Figure 4.22.

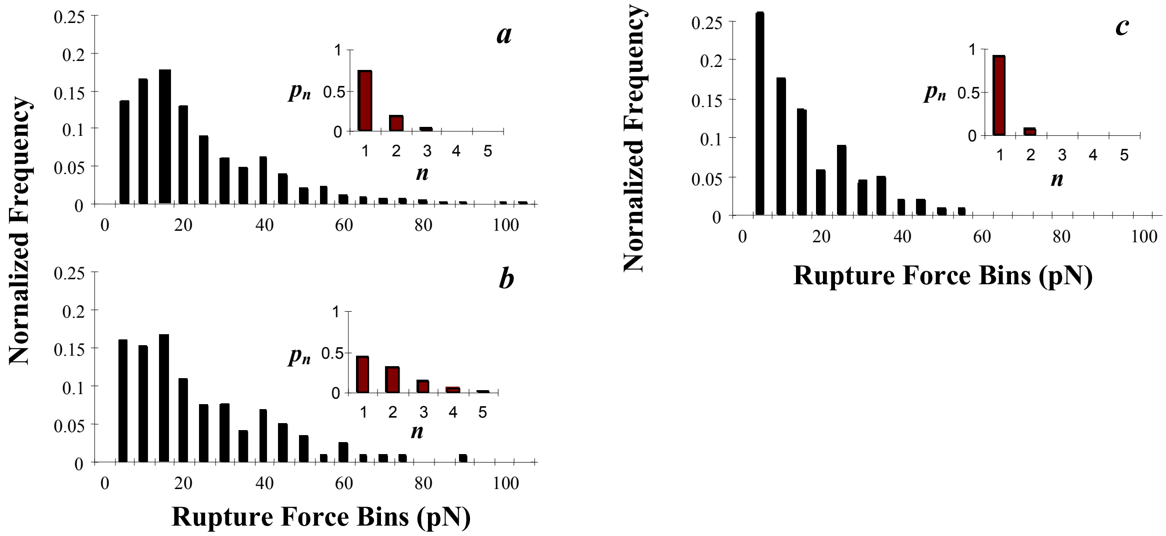

FIGURE 4.22: Detachment force histograms, measured by micropipette with constant rate ramping, of IgG-coated RBC from CD16a-expressing CHO cells, performed in a way similar to those described in Appendix II. Inserts: Probability distribution of bonds, p_n, that mediate the observed adhesions, predicted by the Poisson distribution from the measured adhesion probability, $P_{a|0}$, from the data in each panel. (*a*) All data, 1200 points at an average $P_{a|0}$ of 0.47. (*b*) Subpopulation of A, 100 points at an average $P_{a|0}$ of 0.76. (*c*) Subpopulation ofA , 100 points at an average $P_{a|0}$ of 0.13.

An appealing argument for seeing single bonds is the appearance of quantal behavior in the measurements of low number molecular interactions. This was initially observed in histograms of rupture (or unbinding) forces of biotin/avidin interactions measured with the AFM, which exhibited multiple peaks that appeared periodic (Florin et al. (1994). This kind of histogram is exemplified in Figure 4.22, which was obtained by the micropipette technique using human immunoglobulin G (IgG) coated RBC interacting with CD16a-expressing Chinese hamster ovary (CHO) cells. The histogram of 1200 forces, measured from membrane elongation of the RBC that was retracted at a constant rate, peaks at bins of 15, 40 and 55 pN, which appear to be integer multiples of a quantal unit 18 pN (Fig. 4.22*a*). The frequencies of occurrence of these peak forces seem to correlate with the probabilities p_n of having 1, 2, and 3 bonds (Fig. 4.22*a* insert), calculated from the average $P_{a|0}$ (= 0.47) using Poisson statistics. A subpopulation of these, 100 forces that were measured at a high $P_{a|0}$ (= 0.76) value, resulted in a histogram with the same peak locations but altered relative heights (Fig. 4.22*b*). These heights again correlate with the p_n, which is now redistributed towards more likely having multiple bonds (Figs. 4.22*b* insert). Another subpopulation of 100 forces that were measured at a low $P_{a|0}$ (= 0.13) value resulted in a histogram with leftward shifted peak locations (Fig. 4.22*c*). This is likely due to nonspecific binding, which comprises ~7% of total binding with much smaller rupture forces

One interpretation of histograms such as those shown in Figure 4.22 is based on a deterministic view: A single bond should have a defined strength below which it would remain intact and above which it would fail, *n* bonds would have an overall strength *n* times that of the single bond strength. Applying this view to analyze the rupture force histogram, the quantal unit was interpreted as the single-bond strength (Florin et al. (1994)). However, such a deterministic view may not be valid at low loading rates (Zhu et al. (2000)). Recently more and more data support a probabilistic view: Noncovalent bonds dissociate stochastically, resulting in random rupture forces of a broad distribution, which is governed by the force-dependence of reverse-rate (Bell (1978), Evans et al. (2001 and 1995), Merkel et al. (1999), Zhu et al. (2000)). Unless the loading rates are sufficiently high, there may be significant overlaps among distributions of forces required to rupture clusters of different number of bonds, which obscures their discrimination (Zhu et al. (2000)).

The term quantal behavior is generally used to describe measurements that appear to behave as superposition of a low number of “elementary quantities”. In essence, a quantal binding unit possesses invariant characteristics of measurements as they become less and less frequent, often resulted from the number of interactions involved being progressively decreased. Besides the rupture force case exemplified in Figure 4.22, quantal behavior has also exhibited in other forms. The point-attachments observed in the micropipette experiments behaved as quantal binding units because they appeared to form independently of each other and with equal probability, regardless how much their frequency of occurrence decreased. In the flow chamber experiment, while the frequency of cell tethering should decrease with decreasing site density, the distribution of the observed tether lifetimes should not change in the low site density regime where single molecular interaction is expected to be predominant. This kind of “quantal behavior” has indeed been observed, which has been used to argue that the observed tethering events are supported by single bonds (Alon et al. (1995)).

However, although single bonds must behave as quantal binding units, quantal behavior does not necessitate single bonds, i.e., quantal behavior is a necessary but insufficient condition for single bonds. There are several caveats that can critically affect data interpretation. The questions are: Does the quantal binding unit represent the elementary binding unit or the smallest detectable unit or is the elementary binding unit a single bond or a cluster of bonds?

Observation Of FcγRIII Mediated Phagocytosis At The Single Cell Level:

Fcγ receptors are a critical link between the humoral and cellular arms of the immune system. They are expressed on hematopoietic cells and result in a wide array of cellular responses that include the release of inflammatory mediators, lymphokine production, cytotoxic triggering, cell activation, regulation of antibody production, and phagocytosis of antibody coated particles. As previously mentioned, there are three major classes of Fcγ receptors. Many cells coexpress more than one type of Fcγ receptor; moreover each type is polymorphic and expressed in different structural forms making experimental procedures difficult to design that isolate the source of a specific cellular function to a particular Fcγ receptor type. Controversy has surrounded the role of CD16b and the immune function of phagocytosis. Because CD16b is GPI anchored and does not require coexpression with the γ or ζ subunit, it was theorized not to be able to signal for phagocytosis. Some experimental results have implicated this to be the case, however, here CD16 was transfected into CHO cells to remove the influence of other Fcγ receptors for the experimental design. The link between the CD16 form and phagocytosis function was investigated at the single cell level.

The direct visualization of the phagocytosis of EA by CHO cells at the single cell level was accomplished using micropipette manipulation. Previously this technique was used to observe the phagocytosis of yeast by macrophages. The phagocytosis described here occurred over a period of 15 minutes. The ingestion of the EA was confirmed using an ultrasensitive liquid nitrogen cooled CCD camera under epi-fluorescence illumination.

The EA, when viewed separately was autofluorescent. The CHO cell, when viewed separately, was not autofluorescent. After engulfing the EA, however, the CHO cell became fluorescent. Because CHO cells are not normally capable of phagocytosis, these data confirmed that CD16a expressing CHO cells could phagocytose EA and confirmed the phagocytosis data derived from colorimetric and fluorescent methods. Together, these results demonstrate that GPI anchored CD16b alleles differ from CD16a in their ability to mediate phagocytosis. Futhermore, since studies with other FcγRs have shown that CHO cells lack the phoagocytic pathways mediated by the cytoplasmic domain of FcγRs, the phagocytosis of EA by CHO cells stably transfected with C16a and CD16a-subunit chimera provides an ideal system to dissect the phagocytic signaling pathways mediated by these FcγR-associated subunits

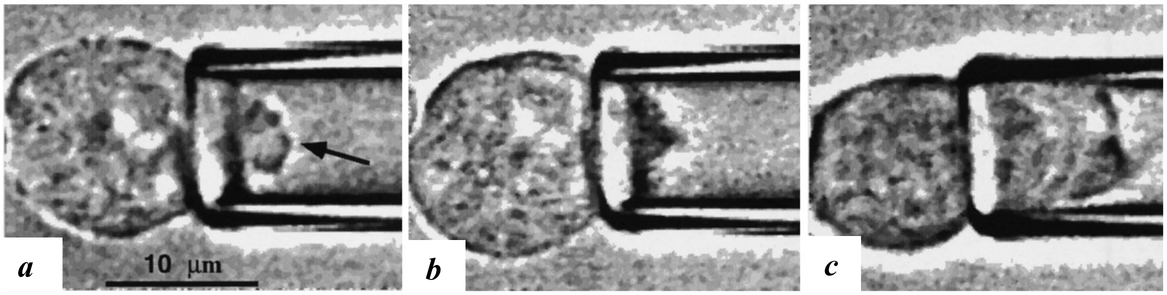

Figure 4.23: Sequential photomicrographs of phagocytosis of EA by a CHO cell expressing CD16a. The human erythrocytes were opsonized with CLBFcgran1, an anti-CD16 mAb, and allowed to adhere to CHO cells in a micromanipulation chamber. A CHO cell with a bound EA (indicated by arrow) was captured by a micropipette (*a*) and the entire phagocytic process (*b* and *c*) was viewed with brightfield microscopy, and the images were recorded using a closed circuit video system.

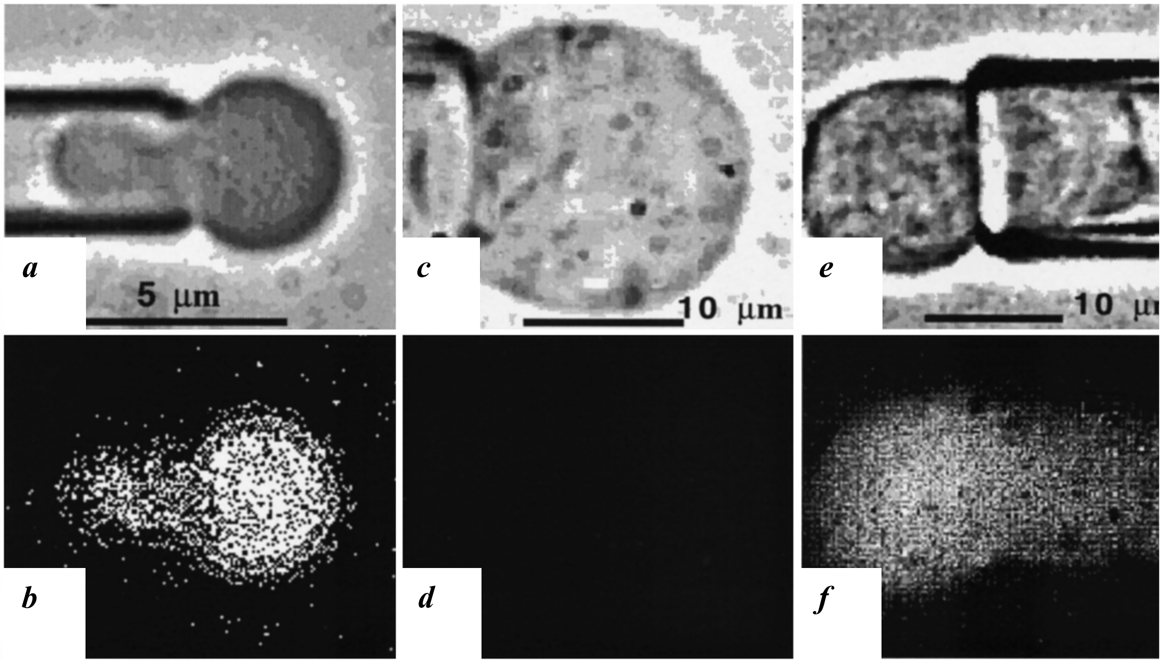

Figure 4.24: Brightfield (*a*, *c*, and *e*) and fluorescent (*b*, *d*, and *f*) images of a human EA (*a* and *b*), a CD16a-positive CHO cell (*c* and *d*), and a CD16a-positive CHO cell that has engulfed an EA (*e* and *f*). The fluorescent images were obtained using an ultrasensitive liquid nitrogen-cooled CCD camera. No fluorescent dyes were used; therefore, the images seen were from autofluorescence of the cells. The fluorescent images shown in *b*, *d*, and *f* were the same cells as those brightfield images shown in *a*, *c*, and *e*. It can be seen that the originally nonfluorescent CHO cell (*d*) became fluorescent after engulfing the autofluorescent EA (*f*).

CHAPTER 5

DISCUSSION

The Method Measures Zero-Force Rate Constants

One of the major goals of this thesis was to develop a method to measure 2D kinetic rates when both of the interacting molecular species are anchored to apposing surfaces, as in the case of cell adhesion. An interesting feature of this method is that the chemistry of receptor-ligand binding is quantified mechanically. Because it is well known that applied forces can influence the binding kinetics (Bell, 1978), the question naturally arises: At what force level were the kinetic rates measured by the present method? The answer is that k_f^0 and k_r^0 represent rate constants at zero force, as indicated by their superscript. This is a critical contention, for without it, all of the analytical solutions to the master equations would have no longer been valid (Piper et al., (1998)).

The reason for the above contention is that, during the contact period, the pipette impingement force that pushes the two cells together is most likely borne by the membrane and/or cytoskeleton support rather than by the receptor-ligand bonds. Although at the end of the contact period the bonds (if adhesion occurs) are stretched and broken as the cells are being pulled apart, this only serves to provide a signal to the observer of whether or not adhesion occurred during the given contact time. It is necessary to apply force to break all bonds for the adhesion test to be repeated in the next cycle; but this takes place at a later time. The contact period ends at the instant when the piezo-driven pipette starts to pull the cells apart. Moreover, care was taken to ensure that the rate of force application was sufficiently fast that the time it took to break the contact was negligible compared to the shortest contact duration tested (see below). In other words, in the present method, one counts the occurrence of adhesion events in the contact time when no tensile force is applied, instead of measuring the time required for the forced dissociation of the preformed bonds in the postcontact adhesion-detection phase. The latter measurement, i.e., lifetime of stressed bonds, also contains kinetic information; and this is similar to the flow chamber experiment (Alon et al., (1995, 1997); Chen et al., (1997)). Thus, despite the fact that the formation of adhesive bonds can only be detected when they are broken by externally applied forces, the rates measured by the present method are those of spontaneous reaction in the absence of force.

The Method Measures Receptor-Ligand Binding

A useful extension from the above line of reasoning is that this micropipette protocol ensures that the measured rate constants represent the kinetics of reversible binding of receptors and ligands rather than their irreversible extraction from the cell membrane. The latter possibility always arises when the assay involves cell detachment (Evans et al., (1991)). This thesis develops a novel method of addressing this question quantitatively. The details of this approach were described in the results section, the key observation is that the binding evolution curves such as those exemplified in Fig. 4.14 exhibit two qualitatively different features. One is characterized by the evenly distributed positive adhesion scores among all tests and a stable running frequency as the test cycle count becomes large (Fig. 4.14*a*). The other is characterized by the concentration of positive adhesion scores in the earlier tests and a declining running frequency with increasing test cycle count (Fig. 4.14*b*). The basic argument is that the former reversible behavior is suggestive of dissociation at the receptor-ligand binding site (adhesive detachment mode), whereas the latter irreversible behavior is indicative of disruption at the protein-membrane anchor site (cohesive detachment mode). It was found that the detachment modes were correlated with the types of molecular bonds involved (e.g., receptor-ligand binding versus antibody-antigen binding) (Chesla et al., (1995)). A quantitative measure of the extraction probability, or irreversibility, can be derived from the statistical analysis of the binding evolution curves (Chesla et al., (1997)).

The receptor (CD16a) and ligands (IgG) employed in this work were found to form weak bonds that would most likely dissociate at detachment. In fact, analyses of all of the binding evolution curves that gave rise to all of the adhesion probability data shown in Figure 4.4 demonstrated small probabilities of uprooting compared to the extraction probability in the case in which the bonds were mediated by Leu-11b-CD16a binding (Fig. 4.14*b*). While this low extraction probability is not required for the insurance of the rate constants determined by the present method to be those governing the binding of receptors and ligands rather than their membrane anchoring, it does justify the use of the running frequency at the last test as the best estimate for the adhesion probability. For declining running frequency, the measurement of adhesion probability requires fitting of the entire binding evolution curve to a Markov process model, as exemplified in Fig. 4.14*b*. Unlike reversible binding, where the adhesion probability is independent of the test cycle count, the adhesion probability for the irreversible binding decreases with the test cycle count. Nevertheless, its extrapolated initial value before the first test can be used for the purpose of employing the present method. Using such initial P_a data, the theoretical analysis described herein can still be applied to evaluate the kinetic rates for receptor-ligand binding, despite the fact that measurement of this binding probability results in uprooting of receptors and/or ligands in such a case (Chesla et al., (1997)).

Further Support For The Poisson Approximation

The described micropipette method includes a systematic approach to determining the kinetic mechanism. The 1:1 stoichiometry of the 2D adhesion determined by the present work is in agreement with that measured in 3D binding (Ghirlando et al., (1995)). The analyses presented in the Results section have clearly demonstrated the feasibility and illustrated the strategy of the approach. The analysis was greatly enhanced by the closed-form solution, Eq. 3-5, which forms the basis of several novel graphical representations of the data (Figs. 4.6-4.8). From Fig. 3.2, the condition for the Poisson type of approximate solution (Eq. 3-5 if $\nu_b = 1$) to be valid is $A_c m_{\min} \gg (\nu_r/\nu_b)\langle n \rangle$, which, when all stoichiometric coefficients are unity, becomes $K_a^0 m_{\max} \ll 1$. From the values listed in Table 4.1, it can be seen that this condition is satisfied for all $m_{\max}$ values tested, justifying the use of the Poisson approximation. When P_a is plotted against the average number of bonds, $\langle n \rangle$ (Fig. 5.1), all of the P_a versus t data shown in Fig. 4.8 collapse into a single curve, regardless of the individual values of k_f^0, k_r^0, m_r, m_l, and t, further supporting the Poisson approximation and demonstrating the same kinetic mechanism for the two IgG ligands from different origins.

Comparison To TheD eterministic Kinetic Model

In addition to the master equations, Eq. 3-3, its deterministic counterpart, the large system limit of Eq. 3-4a (with $\sigma_n^{(\nu_r+\nu_l)} = \sigma_n^{(\nu_b)} = 0$), or rather, that of the Poisson approximate master equations (the $\nu_b = 1$ case),

$$\frac{d}{dt}\left(\frac{<n>}{A_c}\right) = k_f^0 m_r^{\nu_r} m_l^{\nu_l} - k_r^0\left(\frac{<n>}{A_c}\right) \qquad (5\text{-}1)$$

was tested for the ability of its solution ($\langle n\rangle/A_c$) to fit the measured P_a versus t data. Given the nearly linear relationship between P_a and $\langle n\rangle$ when they are small (see Fig. 5.1), it is not surprising that Eq. 5.1 was also able to fit the data, yielding comparable rate constants (not shown)

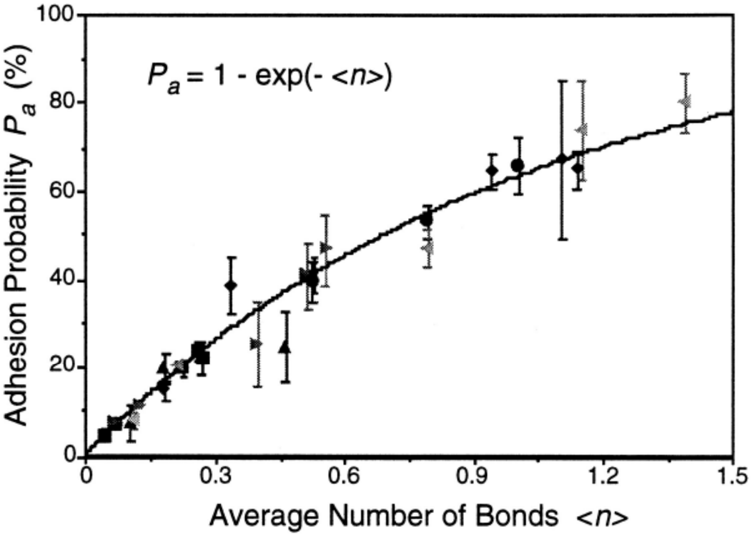

Figure 5.1: The probability of specific adhesion, P_a, was plotted against the average bond number, $\langle n\rangle$, which was calculated based on Eq. 3.6b, using the two pairs of evaluated kinetic rate constants (Table 4.1, the two "combined data" rows for human and rabbit IgG, respectively). All data (points) collapsed into a single curve, which is in excellent agreement with the indicated theoretical solution (curve). The error bars were computed from the original data by using the Gaussian error propagation law.

However, it cannot be emphasized enough that major conceptual differences exist between the deterministic and probabilistic viewpoints. In large systems appropriate for the deterministic description, the fraction of molecules in the bound state is small initially; and only when the contact time approaches the reciprocal per cell forward rate constant, $1/(A_c m_r m_l k_f^0)$, will the number of bonds become comparable to that of the total reacting molecules. Because the number of receptors and ligands participating in binding is enormous, however, even a very small fraction of these represent many molecules. Therefore, bond formation must occur as soon as the two cell membranes are placed in contact. Similarly, dissociation takes place immediately after bonds are formed, despite the fact that the fraction of bonds dissociated is small until the contact time is comparable to the reciprocal reverse rate constant, $1/k_r^0$. In the transient phase of the $\langle n \rangle/A_c$ versus t curve, bond formation outpaces bond dissociation, whereas the two processes reach an equal rate in the plateau phase.

In small systems, by comparison, only a few or even no bond may form during the entire contact time, for one no longer has large numbers of molecules interacting simultaneously. As illustrated in Fig. 5.2*a*, bond formation may occur at any instant during the contact time, or it may not occur at all. Moreover, bonds formed at an earlier instant after the beginning of contact may dissociate at a later instant before the end of the contact. In any particular adhesion test, when an adhesion is detected during cell-cell separation, the experimenter does not know the precise moment in the contact period when the bonds are formed. Similarly, when no adhesion is detected, it is not known whether this is a case in which the bonds formed at earlier instants have already dissociated, or it is the case in which there is no bond formation at all. Nevertheless, one thing is certain and measurable in repeated adhesion tests: the probability of adhesion and its changes with the contact time. Thus, from the probabilistic standpoint, it is the likelihood of bond formation (as opposed to bond formation itself) that outpaces the likelihood of bond dissociation (as opposed to bond dissociation itself) in the transient phase of the P_a versus t curve. In the plateau phase the changes in the two likelihoods reach an equal rate.

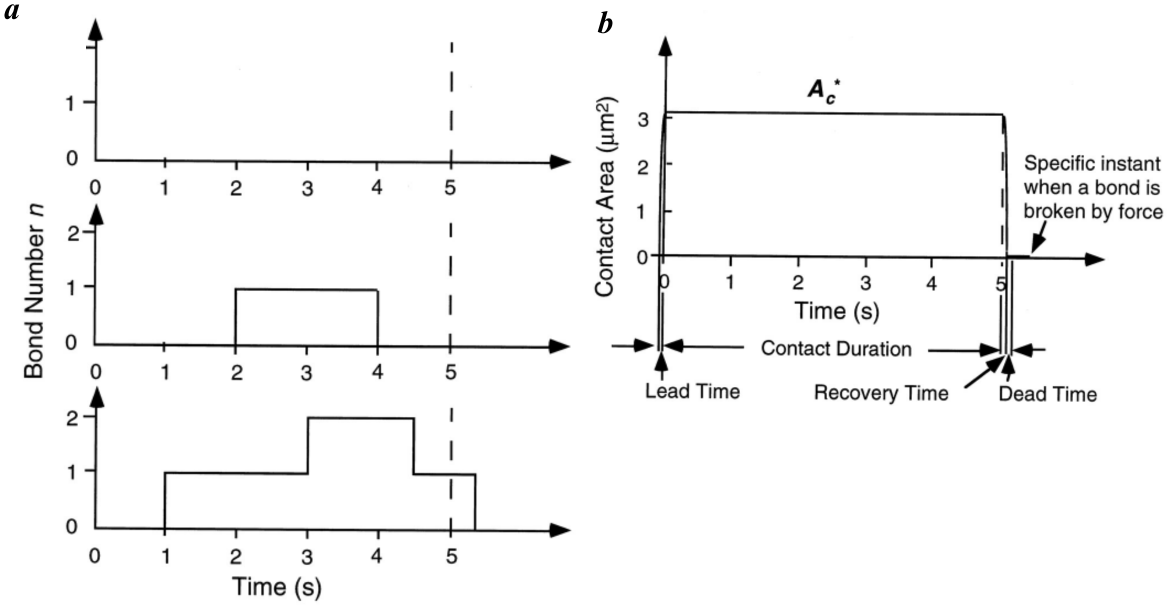

Figure 5.2: (*a*) Three example realizations of the bond number, n, as a stochastic process in time, t, during the cell-cell contact. The changes in n appear as random jumps of unit step size that could take place at any instant. Either formation of a new bond (n is increased by 1) or dissociation of a preformed bond (n is decreased by 1) may occur. (Top) No bond formation occurred during the entire 5 s of contact duration. (Middle) A bond was formed at 2 s but dissociated at 4 s. In both cases, no adhesion was detected by the experimenter, and he would not be able to tell the different between the two. (Bottom) Two bonds were formed at the 1- and 3-s time points respectively. Adhesion was detected in the postcontact cell-cell separation phase at the end of the dead time (5.1-s time point), after which the bond was broken by force at the 5.3-s time point. However, the experimenter would not know that more than one bond was formed, but one dissociated at the 4.5-s time point before the end of the contact duration. (*b*) Schematic of how the apparent contact area changes with time, indicating the definitions of lead time, contact duration, recovery time, and dead time. Note that the apparent contact area A^*_c ($=\pi D^2/4$, where $D \approx 2$ μm is the apparent contact diameter measured from photomicrographs such as that shown in Fig. 3.1) is proportional, but not necessarily equal to the true contact area A_c. Also indicated is the instant at which the bond shown in the bottom panel of A was broken by force.

It should be noted that, in small systems appropriate for the probabilistic description, the time scales set forth by $1/(A_c m_r m_l k_f^0)$ and $1/k_r^0$ reflect the respective waiting times necessary for the events of bond formation and dissociation to occur, not the actual durations of these events. The physical processes during which the binding pockets of the receptor and ligand fit into or break away from one another take place on a much shorter time scale (~ μs or even ns; Bell, 1978), as illustrated in Fig. 5.2*a* by instantaneous jumps. The waiting time is limited by diffusion (predominantly the rotational and orientational modes rather than the translational mode).

Effect Of Finite Time Requirement For Adhesion Detection

The beginning of the contact period is operationally defined as the instant when the piezo-driven micropipette first arrives at its pause position and stops motion (Fig. 5.2*b*). At this moment, the contact area has achieved a plateau level; this is defined as A_c. To arrive at this finite contact area, however, requires a nonvanishing time (called *lead time*) that precedes the above-defined beginning instant of the contact period and which starts when the two cell membranes first come into point contact (Fig. 5.2*b*).

Similarly, the end of the contact period is operationally defined as the instant when the experimenter starts to pull the cells apart, but at this moment the cells are still in touch with one another (Fig. 5.2*b*). In a process that is the reversal of what occurred in the lead time, the RBC membrane gradually reassumes its uncompressed shape upon the removal of the impingement force (assuming that adhesion, if any, occurs at the apex); the time of this process is called the *recovery time* (Fig. 5.2 *b*).

Theoretical treatment of the variable contact area during the lead time and the recovery time is possible by replacing the constant A_c in Eq. 3-3 with a (given) function of time; but this will greatly increase the mathematical complexity of the analysis. Such a treatment seems not to be warranted, for the overall effect of not including in the analysis the lead time and recovery time must be minimal. Adhesions that occurred in the lead time would be included as adhesions that occurred during contact time. In contrast, bond formation and dissociation that occurred in the recovery time would not be included, as they could not be detected by the experimenter. Thus the individual effects of excluding the lead time and recovery time from analysis cancel one another.

The experimenter cannot tell whether adhesion has occurred until the RBC has been further withdrawn, resulting in either a deflection in its membrane (Fig. 3.1*c* or *d*) or a separation of its spherical outline from the CHO cell (Fig. 3.1*b*). This is also a process that takes nonvanishing time (called *dead time*) to accomplish. Formation of new adhesions during dead time is highly unlikely because of the vanishing contact area. However, bonds preformed during the contact time but dissociated in the dead time (probably at a faster rate because of the influence of force) cannot be counted. The effect of such a dead time is analyzed below.

Because $0.5/k_r^0$ is the contact time needed for the adhesion probability to reach half-maximum, some of the P_a data ought to be measured in contact times shorter than $0.5/k_r^0$ for both kinetic rate constants (as opposed to just the binding affinity) to be resolved, as measurements at longer contact times where the adhesion probability levels off contain only equilibrium information. In the present work, $0.5/k_r \approx 1.4$ and 2.5 s for CD16a binding to human and rabbit IgG, respectively. Two contact time points (0.5 and 1 s) shorter than $0.5/k_r^0$ were used. The piezoelectric translator withdrew the micropipette at a speed of 10 μm/s. A 0.5-μm withdrawal, which is quite enough for the experimenter to determine whether adhesion has occurred, required only 0.05 s. Such a dead time is an order of magnitude shorter than the shortest contact duration and 30-50 times shorter than $0.5/k_r^0$. This ensures that the adhesion events that occurred during the dead time would be negligible compared to those that occurred during the contact time, validating the applicability of the present method to the CD16a-IgG system.

However, if the receptor-ligand interaction in question dissociates with a fast rate such that its $0.5/k_r^0$ is comparable to the dead time, then bond dissociation becomes likely to occur in the dead time. This would result in an underestimation of the adhesion frequency if contact times comparable to $0.5/k_r^0$ were used. To minimize such an effect, much longer contact times must be used to ensure that binding events that take place in the contact time would remain dominant over those that occur in the dead time. Consequently, only steady-state, not transient data can be reliably measured, yielding only the binding affinity, not kinetic rate constants.

Thus it is of interest to reduce the dead time as much as possible. However, withdrawing the RBC too fast would induce significant hydrodynamic forces that deform the cell. Moreover, rapid deflections of the RBC would be resisted by the membrane viscosity in addition to elasticity. Both effects would reduce the sensitivity of the RBC force transducer. Using the Stokes equation, $F = 6\pi\eta R_c V$, the drag force F a spherical RBC (of radius $R_c = 2.5$ μm) experiences as it moves in a medium of viscosity $\eta = 10^{-3}$ pN · s/μm^2 at a speed of $V = 10$ μm/s can be found to be 0.5 pN, much smaller than the typical single bond strength. However, using a Voigt model for the RBC membrane with a membrane viscosity $\eta_m \approx 0.6\text{-}1.2$ pN s/μm (Hochmuth, (1987)), the viscous resistance to a 10 μm/s deformation rate would be 6-12 pN, on the same order of magnitude as the typical single bond strength. Indeed, we found that a pipette retraction speed much greater than 10 μm/s resulted in notable reduction of the frequency of detectable adhesions.

Effect Of Low Force Detection Limits

The value of the forward rate constant predicted by the present method depends on several factors. One of these is whether the adhesion probability estimate takes all positive adhesion scores into account. This requires that even a single receptor-ligand bond be unambiguously detected. To achieve this ultrahigh level of sensitivity, the human red blood cell was used as the adhesion detector (Fig. 3.1). The micropipette aspirated RBC force transducer has been shown to be capable of detecting forces as low as subpiconewtons, which is orders of magnitude lower than the typical strength of a noncovalent receptor-ligand bond (Bell, (1978); Evans et al., (1991); Chesla and Zhu, (1996); Zhu and Chesla, (1997)). However, dissociation of such noncovalent receptor-ligand bonds is a stochastic event that could occur at any force, even at zero force (Bell, (1978); Evans et al., (1991); Zhu and Chesla, (1997)). As such, there would always be a fraction of positive adhesions that are inevitably miscounted as false negative nonadhesions. The impact of this detection limit is examined below.

Let α_n be the fraction that is miscounted in those adhesion events that are mediated by n bonds, because of the sensitivity cutoff of the adhesion detector. The relationships $\alpha_n \geq 0$ and $\alpha_n > \alpha_{n+1}$ ($n \geq 1$) must hold, as the more bonds that are involved in the adhesion, the harder it is for it to dissociate at low force, and hence the smaller the miscounted fraction. For simplicity, the α_n's are assumed to be parameterized as $\alpha_n = \alpha^n$ ($0 \leq \alpha < 1$). This equation is probably not exact, but it should be a reasonable approximation. The advantage of using such a power law expression with a single parameter is that it enables a close-form solution. Discounting these fractions from the "ideal" adhesion probability, $P_{ai} = 1 - p_0$, the "actual" adhesion probability, P_{aa}, detected by the experimenter, the one that ought to be used to fit the data, should be

$$\begin{aligned} P_{aa} &= P_{ai} - \sum_{n=1}^{\infty} \alpha^n p_n = 1 - \sum_{n=0}^{\infty} \frac{(\alpha <n>)^n}{n!} \exp(- <n>) \\ &= 1 - \exp\{-(1-\alpha) A_c m_r m_l K_a^0 [1 - \exp(-k_r^0 t)]\} \end{aligned} \tag{5-2}$$

It follows from Eq. 5-2 that, as a result of detection cutoff, the binding affinity (and thereby the forward rate constant) would be underestimated by a factor of $1 - \alpha$, whereas the reverse rate constant is not affected.

Effects Of Receptor And LigandA vailability

Other factors affecting the value of k_f^0 (and K_a^0) derived from the present work have to do with the availability of the receptors and ligands in the contact area. In contrast to k_r^0, which has the same unit (s^{-1}) on both the per-cell and per-molecular density basis, the per molecular density k_f^0 (in $\mu m^2\ s^{-1}$) was not computed directly from the fitting of the P_a versus t data. Instead, it was lumped into a per-cell forward binding rate constant, $A_c m_r m_l k_f^0$ (s^{-1}). To calculate k_f^0 from $A_c m_r m_l k_f^0$ requires separate experiments to independently measure the densities of receptors, m_r, and ligands, m_l, as well as the contact area, A_c.

Two assays were employed in the present study to measure m_r and m_l: flow cytometry and radioimmunoassay. As can be seen in Fig. 4.1, either assay allowed for consistent quantification of CD16a expressed on CHO cells and IgG coated on RBCs. However, whereas soluble antibodies used in these assays could access all surface antigens, it is likely that ligands coating the RBCs were only able to access those receptors that were localized on the tips of the microvilli, but not those that were hidden in the membrane folds of the rough surface of a CHO cell. It is not known whether the CD16a molecules are evenly distributed on the CHO cell surface, as are β_2 integrins on neutrophils, or are concentrated on the microvilli tips, as are L-selectin and PSGL-1 on neutrophils (Hasslen et al., (1996)). Should it be the former case, the number of molecules capable of participating in binding ought to be its density (molecule per cell/total area per cell) times the area of the microvillus tips in the contact, not the apparent contact area. Taking an estimated 100% excess membrane over a spherical cell of radius 10 μm and assuming the microvilli to be cylinders 0.5 μm long and 0.1 μm in diameter, it can be estimated that only 2.5% of the apparent contact area measured from the photomicrograph (~3 μm^2 in all experiments; cf. Fig. 3.1*a*) can be counted as true A_c.

Although the surface of a RBC is much smoother than that of a CHO cell, not all of the ligands necessarily have a proper orientation that is recognizable by the cell-bound receptors, as the chromium chloride method employed to coat the RBC surface with IgG is not specific. We have investigated this issue, and the details will be described elsewhere. Briefly, it was found that, of the ligands capable of interacting with soluble antibodies in the surface density determination (the values listed in Table 1 for m_l), only a small fraction (~10-20%) are functioning in cell adhesion. The kinetic parameters reported in Table 4-1 and 4-2 were calculated assuming all IgG molecules detected by flow cytometry in site density determination were functioning; thus the values for k_f^0 (and K_a^0) are underestimated.

In addition, the total human IgG used in this study includes all four subtypes, of which only two, hIgG1 and hIgG3, bind to CD16 (Nagarjan et al., (1995)). Because they comprise ~70% (hIgG1) and 5% (hIgG3), respectively, of the total hIgG, the kinetic rate constants calculated here are average properties of CD16a binding to the two subtypes of hIgG. Experiments are under way to measure the intrinsic kinetic properties of each subtypes of hIgG1 and hIgG3.

Despite the uncertainty associated with dissecting the per molecular density forward rate constant k_f^0, the values of the per-cell forward rate constant, $A_c m_r m_l k_f^0$, and the reverse rate constant, k_r^0, should be unambiguous and directly relevant to predicting cellular behavior, as they were evaluated directly from the cell adhesion data. It is interesting to note that these two parameters are of the same order of magnitude as those measured for E-selectin/carbohydrate ligand binding by the flow chamber method (Kaplanski et al., (1993)). Because the kinetic rates are believed to determine whether the receptor-ligand interaction is rapid enough to capture moving cells in the flow environment, we tested whether Fcγ receptors could mediate adhesion of flowing cells to a hIgG-coated surface. Preliminary results suggest that this is indeed the case (Wright, (1997)).

Individual Molecular Features Of TheM ethod

An interesting observation from Fig. 5.1 is the smallness of the average number of bonds ($\langle n \rangle < 1.5$) that mediate the adhesion seen here. To further explore this low bond number feature, the P_{aa} versus $\langle n \rangle$ relationship (Eq. 5-2) was used to eliminate $\langle n \rangle$ from Eq. 3-5 to obtain a prediction for the bond distribution as a function of adhesion probability:

$$p_n = \frac{(1 - P_{aa})^{1/(1-\alpha)}}{n!} \ln^n (1 - P_{aa})^{-1/(1-\alpha)} \tag{5-3}$$

It can be seen from Fig. 5.3*a* that, even with the highest adhesion probability seen in our experiments, the number of bonds that have nonvanishing probabilities (≥ 0.01) is no more than five. If $\alpha = 0$, $p_1 > p_n$ for $n > 1$, even at $P_{aa} = 80\%$. For moderate and low adhesion probabilities, the bindings are mediated predominantly by single bond events, although this dominance is weakened somewhat as α increases (Fig. 5.3*b*).

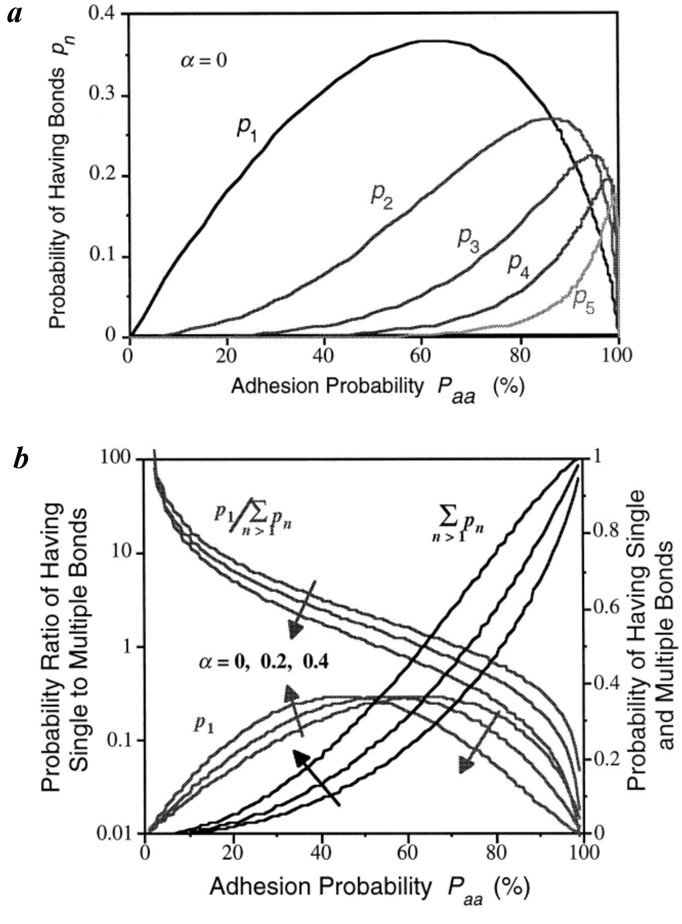

Figure 5.3: Individual bond feature of the present method. (*a*) Probabilities of having the first five bonds, p_n ($n = 1$-5), and (*b*) that of having single, p_1, and multiple, $\Sigma_{n>1}p_n$, bonds (right ordinate), as well as the ratio of the probability of having a single bond to that of having multiple bonds, $p_1/\Sigma_{n>1}p_n$, (left ordinate) as a function of the measured probability of adhesion per contact, P_{aa}, and the fraction of miscounting false nonadhesions, α.

The above low bond number prediction is also consistent with the observation in the micropipette experiment that, although the two cells were allowed to touch each other via an apparent area of a few square microns during the contact period, only very few (usually only one if at all) spatially separate discrete attachment point(s) were observed when the contact was being separated (Fig. 3.1*c* and *d*). One might argue that it was still possible that multiple bonds were involved in these point attachments. For this to be the case, however, the receptors and ligands must either be multivalent or be presented on their respective cell surfaces as clusters, such that bonding of one binding site in the multivalent molecule (or one molecule in the cluster) dramatically increases the probability that the other binding sites in the same multivalent molecule (or other molecules in the same cluster) will bind, leading to the rapid formation of multiple bonds as a single unit in a discrete attachment point of vanishing area, despite the fact that the odds of forming more new bonds in the rest of the contact area of much larger size remains low. The CD16a-IgG binding is monovalent, as shown in the Results and by Ghirlando et al. (1995). Furthermore, it is unlikely that both CD16a and IgG are clustered on their respective cell membranes. Thus, not only does our micropipette method measure the adhesion kinetics of individual cells; it also is very likely to probe the binding kinetics of individual molecules. It should be emphasized that the method does not require all adhesions to be single bond mediated, as the analysis utilizes not only single but also multiple bond events. In other words, the small fraction of multiple bond events contributes useful information, not noise, to the analysis.

A major goal of the present work was to compare the two-dimensional binding kinetics and affinities of two human CD16a membrane anchor isoforms for the Fc domain of IgG. Since adhesion of Fc receptor-expressing leukocytes to IgG-coated targets is an initiating step for many immune responses, the determination of CD16-IgG kinetic rate constants is important in both biological and clinical settings. Unlike typical hormone receptors that bind soluble ligands (*i.e.* three-dimensional binding kinetics), adhesion receptors bind membrane-bound ligands (*i.e.* two-dimensional adhesion kinetics). Clearly, it is the two-dimensional, rather than the three-dimensional, kinetic rate constants that are most relevant to physiological situations such as adhesion of a CD16a-expressing NK cell or macrophage to an antibody-coated target cell.

By applying the micropipette method developed in this thesis, an attempt was made to address the following biological questions. Did the membrane anchor (including the associated subunits) influence the kinetic rates? If so, what might be the mechanisms causing the observed changes? To address these questions, the effects of the extracellular domain and the membrane anchor were isolated using the lipid-anchored CD16a-GPI construct. CHO cell transfectants were used to obtain a uniform cellular background across the CD16 membrane isoforms expressed. Under these conditions, the membrane anchor effect was clearly revealed by the micropipette experiment (Figure 4.9). This is the first experimental demonstration of the membrane anchor effect on the kinetic rates.

The three-dimensional binding characteristics were also measured for the same interacting molecules (Figure 4.11) in order to elucidate the mechanism underlying the observed anchor effect. Because much work is available in the literature on three-dimensional CD16-IgG interactions, comparison to those helps validate the two-dimensional measurements and strengthen the conclusions. Indeed, the same trends for affinities were seen in both two-dimensional and three-dimensional measurements, indicating that the micropipette method is adequate for measuring structure-function relationship of cell-bound receptors.

Comparison To Published Results

Vance *et al.* (Vance et al. (1993)) reported a higher three-dimensional binding affinity for monomeric hIgG of CD16a on NK cells (3-10 × 10^6 M^{-1}) than of CD16b on neutrophils (value not determined). The former is therefore referred to as an intermediate affinity receptor, whereas the latter is considered as a low affinity receptor. It was not demonstrated, however, to what degree this differing affinity was due to the differences in the extracellular domain, in the membrane anchor, or in the cellular background of the two membrane isoforms. On the other hand, Tamm *et al.* (Tamm et al. (1996)) reported a similar three-dimensional avidity of CD16a-GPI and CD16b^{NA2}, both expressed on a human embryonic kidney cell line 293, for heat-aggregated hIgG1 (~20×10^6 M^{-1}). These authors suggested that the minor differences in the ectodomains of the two molecules (Figure 2.5*b* and *c*) would not affect their affinity, although their data showed an ~2-fold higher avidity of CD16a-GPI than CD16b for dimeric hIgG1 (3.7 and 2.1 × 10^6 M^{-1}, respectively). In this work it was found that in our CHO cell system using hIgG and RbIgG, CD16a-GPI showed consistently higher affinity than CD16a-TM in both two-dimensional (Table 4-2) and three-dimensional (Table 4-3) binding studies. Furthermore, repeated side-by side experiments reproducibly showed that the order of three-dimensional affinities for hIgG, hIgG1, and RbIgG was CD16a-GPI > CD16a-TM > CD16b^{NA1} ~ CD16b^{NA2} (Table 4-3 and data not shown). The discrepancies in the absolute values of three-dimensional affinities measured by the different laboratories might be due to cell type-specific glycosylation of CD16 (Edberg et al. (1997)). However, the data acquired in this work were obtained using the same CHO cells to express various CD16 membrane isoforms. These results appeared to indicate that in comparison to CD16a, the variations in the extracellular domains of the two CD16b alleles (Figure 2.5,*b* and *c*), although very small, did significantly reduce their affinities for hIgG and RbIgG (Table 4-3) and for hIgG1 (data not shown). This is not surprising, as two independent single nucleotide polymorphisms (resulting in amino acid changes Leu-48 to Arg-48 or His-48 and Val-176 to Phe-176) in CD16a have been reported to alter the affinity of IgG binding (de Hass et al. (1996),Wu et al. (1997)). The CD16a-TM and CD16a-GPI molecules used in the present study do not have these polymorphic variations (Kurosaki et al. (1989)), as confirmed by sequencing during subcloning of the CD16a-TM cDNA into the pcDNA3 vector.

Possible Role Of The Associated Subunits

Miller *et al.* (1996) suggested that the associated γ chain could enhance the ligand binding affinity of FcγR. They reported at least an order of magnitude higher three-dimensional affinity of CD16a-TM than CD16a-GPI for mIgG2a. The affinity of CD16a-TM for mIgG2a obtained by these authors (12×10^6 M^{-1}) is much higher than the value obtained in our lab, which may be due to the differences in the cells and/or the γ chain used. Miller *et al.* (1996) used monkey kidney COS cells to express transiently human CD16a-TM in association with human γ chain. By comparison, results from our lab were obtained using stably transfected CHO cells to express human CD16a-TM in association with rat γ chain. Furthermore, Miller *et al.* (1996) employed direct Scatchard analysis, whereas this work and our labs work used indirect competitive inhibition to measure affinity. Nevertheless, we found the same trend as Miller *et al.* (1996) that CD16a-TM had higher affinity than CD16a-GPI for mIgG2a.

However, here this effect was ligand-dependent. For CLBFcgran-1, hIgG, and RbIgG, the trend inverted, with CD16a-TM having lower affinity than CD16a-GPI (Figures 4.9 and 4.11,*a* and *b*). These three-dimensional results were supported by those of the two dimensional micropipette experiments, which involved direct visualization of over 20,000 controlled single cell pair adhesion tests. In addition, affinity measurements available in our lab showed that the chimeric molecules CD16a-γ and CD16a-ζ bound similarly to CD16a-TM but differently from CD16a-GPI for all ligands tested, including IgGs from three species and a mAb (Table 4-3) (Chesla, Li, Nagarajan, Selvaraj, Zhu (2000)). Thus, these findings indicate that the role of the associated subunit, if it is indeed the cause of the anchor effect, is not limited to the γ chain but also includes the ζ chain. Moreover, their putative role is not to enhance, but rather to alter, the ligand binding affinity.

The Difference In Ligand Binding Kinetic Rates And Affinity Of CD16 Isoforms Cannot Be Explained By Their Differing Diffusivities

The GPI-anchored CD16 molecules (including both alleles of CD16b and the CD16a-GPI) exhibit a few folds faster translational diffusion on the CHO cell membrane than TM-anchored CD16a as determined by preliminary fluorescence recovery after photobleaching measurements (data not shown). In addition, the GPI anchor is likely to provide more flexibility to the ectodomain of the receptor, which increases its rotational diffusion coefficient, a parameter more relevant to enhancing two-dimensional binding than the translational diffusion coefficient. One should therefore consider whether the faster binding of CD16a-GPI than CD16a-TM to hIgG and RbIgG could be explained by the diffusional difference of the two membrane anchor isoforms. However, the following three lines of reasoning argue against this explanation and allow us to rule it out as the cause for the different kinetic rates of CD16 anchor isoforms.

First, faster diffusion of CD16a-GPI cannot explain the observed effect of the GPI anchor on the forward, and the lack thereof on the reverse, rate constants (Table 4-2). Existing theories have shown that diffusion influences k_f and k_r similarly but not $K_a = k_f/k_r$, since the diffusion effects on the two rates cancel each other in the ratio (Bell (1978)). Second, the anchor effect was seen not only in the two-dimensional micropipette experiment, but also in the three-dimensional binding assays (Table 4-3) where identical but soluble ligands and the same CD16-expressing CHO cells were examined. Diffusion should not affect the three-dimensional results not only because it was the ratio K_a, not k_f or k_r separately, that was measured but also because diffusion is unlikely to be the rate-limiting step in the two-step binding process (the other step being intrinsic reaction). The diffusivity of proteins in fluid phase (>10 $\mu m^2/s$) is usually orders of magnitude greater than cell surface proteins (Lauffenburger et al. (1993)). Finally, the diffusion mechanism cannot explain the inversion of the anchor effect; the faster diffusing CD16a-GPI bound with slower forward rate and lower affinity to mIgG2a than CD16a-TM (Tables 4-2 and 4-3). This negative correlation between diffusion coefficient and forward rate/binding affinity provides direct and definitive experimental proof for the inability of the differing diffusivities to account for the CD16a anchor effect on kinetic rates and affinity.

It should be pointed out that in the micropipette experiment accumulation of receptors in the contact area by lateral diffusion is unlikely. The diffusion coefficients for various CD16 isoforms on CHO cells are of the order of 0.01 μm^2/s (data not shown). The longest contact time in the micropipette experiments was 20 s, which was far from sufficient for the receptors to accumulate in an apparent contact area of ~3 μm^2. Furthermore, only a few bonds were formed in an adhesion produced by the controlled contact in the micropipette experiments (Chesla et al. (1998)), which is a negligibly small number comparing to the hundreds and thousands of receptors in the contact area. This will not generate any appreciable density gradient of free receptors to drive them to diffuse into the contact area.

The Difference In Ligand Binding Kinetic Rates And Affinity Of CD16 Isoforms Cannot Be Explained By Their Differing Orientations And Lengths

The lack of TM and cytoplasmic domains as well as the associated subunits of the CD16a-GPI may alter the orientation of its extracellular domain. Moreover, the GPI moiety may extend the Fc binding epitope further outward relative to the glycocalyx (Figure 2.5). The length of a receptor has been demonstrated to influence its ability to support adhesion at 4 °C (but the effect diminished at higher temperatures) (Chan et al. (1992)) and under flow (but not static) conditions (Patel et al. (1995)). It is thought that a longer and more flexible molecule can explore larger space above the membrane and assume more spatial configurations. This lengthens the interaction range of the receptor, thereby facilitating its effort to find the ligand when it is surface-linked (Wong et al. (1997)). However, although both orientation and length can influence ligand binding kinetic rates and affinity, this effect should be qualitatively monotonic for all ligands. Therefore, the observation that the GPI anchor increases affinity for human and rabbit

IgGs but decreases affinity for murine IgG2a allow us to exclude orientation and length as possible causes for the anchor effect (Chesla, Li, Nagarajan, Selvaraj, Zhu (2000)).

The Difference In Ligand Binding Kinetic Rates And Affinity Of CD16 Isoforms Cannot Be Explained By Their Differential Distribution And Clustering

Some GPI-anchored proteins have been suggested to be clustered in glycosphingolipid and cholesterol-enriched domains, *e.g.* caveolae (Anderson et al. (1998)). CD16a-GPI might appear to bind better than CD16a-TM in the three-dimensional assay should the former isoform be functionally clustered, since binding of aggregated soluble ligands to receptor clusters might result in an apparently higher avidity.

Similarly, being distributed in different membrane domains might potentially influence the two-dimensional binding properties of CD16a-GPI. The forward rate k_f and binding affinity K_a measured from the micropipette assay are lumped with the contact area A_c. The true or functional contact area A_c was not measured but should be proportional to the apparent contact area directly visible under the light microscope (Figure 3.1) (Chesla et al. (1998)). The CHO cell surface displays extensive roughness; thus only the "hills," not "valleys," of the membrane folds are likely to be part of the functional A_c. Since the same CHO cells were used to express CD16a regardless of the anchors and the same red blood cells were used to present IgG regardless of the species, A_c would be a constant if the apparent contact area was kept constant, as was the case in all of our experiments. Thus, not knowing the value of A_c or of which membrane microdomains it was composed should not affect conclusions based on relative comparisons, provided that the two CD16a membrane anchor isoforms were similarly distributed in the contact area. However, while some adhesion molecules (*e.g.* β_2 integrins) are more or less uniformly distributed on the cell surface, others (*e.g.* L-selectin) are known to localize on the microvillous tips (Hasslen el al. (1996)). Because the latter molecules are present at higher densities on A_c, their k_f and K_a values will be overestimated by a calculation that assumes a uniform molecular distribution. Thus, CD16a-GPI would appear to bind better than CD16a-TM should CD16a-GPI be differentially enriched on the hills (accessible area) or CD16a-TM be differentially enriched on the valleys (inaccessible area) of the membrane folds.

Although the arguments in the preceding paragraphs may seem consistent with the binding pattern seen in the human and rabbit IgG experiments, they cannot explain the inversion of that trend observed in the mIgG2a experiment. The differential distribution and clustering of receptors should not flip when IgGs from different species were used as ligands to assay kinetics. Moreover, differential distribution of GPI- and TM-anchored CD16a should not affect the three-dimensional results, since the soluble ligands should be able to access any membrane domains, and the calculation is based on average measurements over the entire cell surface, not particular compartmentalized domains. We thus conclude that the differences in ligand binding kinetic rates and affinity of CD16a isoforms are not due to their differential distribution and clustering.

No Major Differential Glycosylation Of CD16a Isoforms Can Account For The Anchor Dependence Of Ligand Binding Kinetic Rates And Affinity

GPI-anchored proteins may have different resident time and may hence be processed differently in the Golgi apparatus than TM anchored proteins, resulting in different carbohydrate modifications. However, available analysis of CD16 isoforms purified from CHO cells using SDS-PAGE did not reveal major differences in *N*-linked glycosylation. (Chesla, Li, Nagarajan, Selvaraj, Zhu (2000)). The ~4-kDa higher molecular mass of CD16a-TM than CD16a-GPI can be well accounted for by the 45 amino acid TM and cytoplasmic domains (~5.4 kDa) of the former isoform and the GPI moiety (~1 kDa) of the latter isoform. Of course, more extensive analysis is required to test whether site-specific differential glycosylation exists between the two CD16a membrane anchor isoforms and, if so, whether it is the cause of the observed anchor effects on kinetic rates and binding affinity.

Could The Difference Be Explained By Differing Conformations

A consequence of the possible concentration of CD16a-GPI in glycosphingolipid-enriched membrane microdomains may be its being surrounded by different neighboring molecules. It is conceivable that neighboring molecules of CD16a-GPI could affect its ligand binding. But to affect binding in one way with hIgG, RbIgG, and mAb CLBFcgran-1 but in an opposite way with mIgG2a and mAb VEP13 would most likely require CD16a-GPI to associate with the neighboring molecules. Such an association would most likely have to be in sufficiently close proximity to render a conformational change of the receptor, resulting in variable accessibility by different ligands and mAbs. So far, only the myeloid cell-specific integrin $\alpha_M\beta_2$ has been reported to associate with the GPI-anchored CD16b (Poo et al. (1995)). CHO cells do not express β_2 integrins. By comparison, in order for it to be expressed on the CHO cell surface CD16a-TM must be associated with the γ chain (Figure 2.5*b*). Such an association has been shown to alter the binding of not only CD16a but also CD64 (Fcγ receptor I) (Chesla et al. (1998)).

Finally, an alternative and perhaps simpler hypothesis may be that the differing membrane anchors themselves, when they are inserted into the cell surface, yield such a conformational difference. The view that different conformations of the two CD16a isoforms may be the mechanism underlying their different kinetic rates and binding affinity is supported by the following resemblance between our observations and those commonly accepted as valid evidence for conformational change in integrins. Certain "activation-reporter" mAbs bind integrins only after they have been converted from resting to activated states, which is interpreted as a conformational change that allows for expression of antigenic epitopes that are specific to the activated conformer (Sanchez-Mateos et al. (1996)). Another characteristic of conformational changes of integrins is changes in their abilities to bind soluble ligands and to mediate cell adhesion. The binding results are also available using another mAb (VEP13). VEP13 reacts strongly with CD16a-TM but only weakly with CD16a-GPI, suggesting that the epitope detected by mAb VEP13 is substantially down-regulated after the molecule's anchor has been changed from TM to GPI. In addition, the abilities to bind soluble ligands (and the mAb CLBFcgran-1) and to mediate cell adhesion are different for the two CD16a membrane isoforms, which are caused by their different kinetic rates and binding affinities for ligands (and for mAb CLBFcgran-1) (Chesla, Li, Nagarajan, Selvaraj, Zhu (2000)). Similarly, Kukulansky *et al.* (1999) reported that following anchor cleavage by phospholipase C, the reactivity of the solubilized Thy-1 with several mAbs is lost, and its reactivity with polyclonal anti-Thy-1 antibodies is markedly decreased. These authors interpreted their finding by a GPI anchor-dependent conformational change of the Thy-1 molecule. Thus, the data presented in this thesis strongly suggests that replacement of polypeptide anchor with GPI anchor resulted in a conformational change of CD16a

The diversity of Fc receptors in both structure and function has long been appreciated (van de Winkel (1996)). The ability of Fc receptors to bind ligand has been shown to be influenced by a variety of structural variations. In this study we measured both two-dimensional kinetic rates and three-dimensional affinities of FcγRIII membrane isoforms for various ligands, and we showed that the membrane anchor had an effect on these binding properties, which is likely caused by a conformational difference between the two CD16a membrane isoforms. These findings provide insights into the biological significance of distinct anchors of cell surface proteins.

Resolution Of Force And Detachment Mode

Recently, there has been an increasing interest n measuring the interaction forces between cell adhesion receptors and their ligands (Evans et al. (1991) Florin et al. (1994), Zhu and Chesla (1997)). These molecules are either anchored on the membrane of a cell or coated on the surface of a substratum. The two surfaces are joined together as a result of the formation of non-covalent bonds between the receptors and ligands. The forces are measured when the two surfaces are separated. As previously stated in Chapter 2 (Background / Literature) Bell (1978) calculated the force to rapidly break a single CD16/IgG type bond in the order of 1.2 pN per bond. The force that he calculated to uproot a receptor that is not anchored to the cytoskeleton was estimated at 1.0 pN per molecule, which is the same order of magnitude. The interpretation of the force data therefore requires the knowledge of detachment mode, i.e., via adhesive mechanism if the receptor-ligand bond is dissociated or via cohesive mechanism if the receptor-membrane anchor is disrupted.

In this thesis, a simple micropipette assay was developed to measure the force and kinetics of Fcγ receptor III (CD16) binding to its ligands. It was noted that the running average of adhesion scores (Figure 4.14) in a series of repeated adhesion attempts (performed on the same contact area on the same pair of cells) exhibited different characteristics. Depending on the types of bonds and membrane anchors, either stable or declining running adhesion frequencies might be observed; here the suggestion is made that the latter is an indication for receptor uprooting.

In the results section the statistical analysis of the running adhesion frequency was presented that enabled measurement of the extraction probability of a receptor from the cell membrane. The idea was since the force to break a bond is a random variable, whether the detachment of a particular receptor-ligand crossbridge results in receptor extraction also is stochastic. Nevertheless, a defined probability of such an event exists and it reflects the relative strengths of the receptor-ligand bond and the membrane anchor. In this experimental system IgG or IgM is covalently bound to RBC membrane proteins using a $CrCl_3$ protocol. Given this, it is more likely that if one of the molecular agents is uprooted, CD16 on the CHO cell surface would be more likely suspected, especially if it is GPI anchored.

Each adhesion test can be modeled as a Bernoulli trial of two possible outcomes: the adhesion score (a random variable). If there are m_r receptors available before the test, each is independent to the others and all have an equal probability to bind a ligand. For each of the bonds formed there is an equal probability, I, of receptor extraction at detachment. Since the sequential repeated adhesion tests are a random process, statistical flucuations among individual realizations (measurements obtained with different cell pairs) are inevitable even if the underlying mechanism is the same. It is therefore important to look at isolated examples in order to draw conclusions about the detachment mechanism. As can be seen in Figure 4.14, the ligand type had a strong effect on the probability of receptor extraction, i.e., the anti-CD16 mAb mediated binding was found to exhibit a much higher probability of cohesive detachment (uprooting) than the Fc mediated binding. In addition, in the case of antigen-antibody binding the receptor type was found to have an influence: the *I* value for the GPI-CD16 was higher than that for the TM-CD16 suggesting an easier extraction for the GPI anchored receptor. As expected, no effect of the receptor anchor was found in the case of the Fc FcR bond, consistent with the adhesive mode of detachment hypothesis.

This model enables quantitiative evaluation of the probability of receptor extraction from the cell membrane using data from repeated adhesion tests. Measuring this probability and correlating it with various types of receptor-ligand bonds and membrane anchors provides insight into the structure-function relationship of the molecules and can provide the basis of a single cell assay for cytoskeletal linkage of integral proteins.

CHAPTER 6

SUMMARY AND RECOMMENDATIONS FOR FUTURE WORK

A novel method has been developed in this work to determine the 2D binding kinetics. The assay is designed to measure the adhesion probability using the micropipette method. Although the protocol was illustrated by the micropipette technique in this work, it can be adaptable to other techniques. The method was validated utilizing a CD16a-TM and human IgG experimental design and systematic strategies were developed to determine the kinetic mechanism and the associated rate constants of the binding reaction. Although the method is interesting and has merit in the fact that 2D kinetic rate determination is of scientific value, a broader affirmation of its merit was and is sought.

As previously stated CD16 is one of only four eukaryotic receptors known to exist natively in both the transmembrane (TM, CD16a) and glycosylphosphatidylinositol (GPI, CD16b) isoforms. The biological significance of this anchor isoform coexistence is not clear. Here we showed that the anchor influenced kinetic rates; compared with CD16a-TM, CD16a-GPI bound faster and with higher affinities to human and rabbit IgGs but slower and with lower affinity to murine IgG2a. The same differential affinity patterns were observed using soluble IgG ligands. The evidence suggests a conformational difference as the mechanism underlying the observed anchor effect, as it cannot be explained by the differing diffusivity, flexibility, orientation, height, distribution, or clustering of the two molecules on the cell membrane. These data demonstrate that a covalent modification of an Ig superfamily receptor at the carboxyl terminus of the ectodomain can have an impact on ligand binding kinetics. The method was utilized to determine the 2D kinetic rates of CHO cell expressed CD16a-TM, CD16a-GPI, CD16b^{NA1} and CD16b^{NA2} during interaction with Red Cell bound human IgG. By comparing these rates as well as the 3D binding affinities determined using soluble human IgG, the effect different CD16 anchor mechanisms (TM versus GPI) was elucidated.

As stated previously, the theory utilized here to determine the kinetic rates of reaction utilizing the micropipette technique can be modified to other experimental methodologies. Usually, cell adhesion assays measure either the probability or the strength of adhesion. In population based studies this result translates into the fraction of adherent cells or the force dependence of the detached fraction of cells. A commercial population based cell adhesion assay was reported in Chapter 2 and described in Figure 2.3. This assay measures the adhesion probability of antibody coated human RBCs to a substrate of variable antigen coating. As shown, the substrate is formed on the bottom of 96 well, “U” bottom wells. The end result of the assay is a determination of whether the substrate is coated with or not coated with antigen. Because the red cell adhesion in this assay is mediated by the formation of antibody-antigen bonds, and as such the adhesion probability and strength must relate to the force dependence of binding affinity of the adhesion molecules, the molecular binding characteristics should be readily derived form the adhesion data. Such models are readily available in literature for similar experimental systems. Piper et al. (1998) describes a similar experimental system involving a population based cell adhesion assay which is also performed in 96 flat well system. In the flat well experimental system, the cells are first allowed to adhere to the substrate bottom then detachment is encouraged by centrifugation of the cells away from the well bottom. The experimental system shown in Figure 2.3 is slightly different with the red cell attachment and detachment being simultaneously encouraged by a single centrifugation step. Nevertheless, the experimental model introduced by Piper (1998) along with the master equations introduced herein can be easily modified to describe the proposed system.

REFERENCES

Alon, R., S. Chen, K. D. Puri, E. B. Finger, and T. A. Springer. (1997) "The kinetics of L-selectin tethers and the mechanics of selectin-mediated rolling." *J. Cell Biol.* **138**:1169-1180.

Alon, R., D. A. Hammer, and T. A. Springer. (1995) "Lifetime of the P-selectin-carbohydrate bond and its response to tensile force in hydrodynamic flow." *Nature* **374**:539-542.

Anderson, P., Caligiuri, M., O'Brien, C., Manley, T., Ritz, J., and Schlossman, S. F. (1990) "Fc gamma receptor type III (CD16) is included in the zeta NK receptor complex expressed by human natural killer cells." *Proc. Natl. Acad. Sci. U. S. A.* **87:** 2274-2278.

Anderson, C. L., Shen, L., Eicher, D. M., Wewers, M. D., and Gill, J. K. (1990) *J. Exp. Med.* **171:** 1333-1345.

Anderson, R. G. (1998) "The caveolae membrane system." *Ann Rev Biochem.* **67**:199-225.

Bell, G. I. (1978) "Models for the specific adhesion of cells to cells." *Science* **200**:618-627.

Berlin, C., R. F. Bargatze, J. Campbell, U. H. von An-drian, C. Szabo, S. R. Hasslen, and e. al. (1995) "α4 integrins mediate lymphocyte attachment and rolling under physiological flow." *Cell* **80**:413–422.

Berenson, R. J., W. I. Bensinger, and D. Kalamasz. (1986) "Positive selection of viable cell populations using avidin-biotin immunoabsortion." *J. Immunol. Methods.* **91**:11-19.

Bianca, V. D., Grzeskowiak, M., Dusi, S., and Rossi, F. (1993) "Transmembrane signaling pathways involved in phagocytosis and associated activation of NADPH oxidase mediated by Fc gamma Rs in human neutrophils." *J. Leukocyte Biol.* **53:** 427-438.

Blank, U., Ra, C., Miller, L., White, K., Metzger, H., and Kinet, J. P. (1989) "Complete structure and expression in transfected cells of high affinity IgE receptor." *Nature* **337:** 187-189.

Bonnerot, C., Amigorena, S., Choquet, D., Pavlovich, R., Choukroun, V., and Fridman, W. H. (1992) "Role of associated gamma-chain in tyrosine kinase activation via murine Fc gamma RIII." *EMBO J.* **11:** 2747-2757.

Boyce, W. E., and R. C. DiPrima. (1977) Elementary Differential Equations and Boundary Value Problem, 3rd Ed. John Wiley and Sons, New York.

Brown, E. J., Bohnsack, J. F., and Gresham, H. D. (1988) "Mechanism of inhibition of immunoglobulin G-mediated phagocytosis by monoclonal antibodies that recognize the Mac-1 antigen." *J. Clin. Invest.* **81 (2):** 365-375.

Bruehl, R. E., K. L. Moore, D. E. Lorant, N. Borregaard, G. A. Zimmerman, R. P. McEver, and D. F. Bainton. (1997) "Leukocyte activation induces surface redistribution of P-selectin glycoprotein ligand-1." *J. Leukoc. Biol.* **61**:489-499.

Capo, C., F. Garrouste, A.-M. Benoliel, P. Bongrand, A. Ryter, and G. Bell. (1982) "Concanavalin-A-mediated thymocyte agglutination: a model for a quantitative study of cell adhesion." *J. Cell Sci.* **56**:21-48.

Chan, P.-Y., Lawrence, M. B., Dustin, M. L., Ferguson, L. M., Golan, D. E., and Springer, T. A." Influence of receptor lateral mobility on adhesion strengthening between membranes containing LFA-3 and CD2." (1991) *J. Cell Biol.* **115**:245-255.

Chan, P. Y., and Springer, T. A. (1992) "Effect of lengthening lymphocyte function-associated antigen 3 on adhesion to CD2." *Mol. Biol. Cell.* **3(2)**:157-166.

Chang, K.-C., D. F. J. Tees, and D. A. Hammer. (2000) "The state diagram for cell adhesion under flow: Leukocyte rolling and firm adhesion." *Proc. Natl. Acad. Sci. USA.* **97**:11262-11267.

Chen, S., and T. A. Springer. (1999) "An automatic braking system that stabilizes leukocyte rolling by an increase in selectin bond number with shear." *J. Cell Biol.* **94**:185-200.

Chen, S., and T. A. Springer. (2001) "Selectin receptor-ligand bonds: Formation limited by shear rate and dissociation governed by the Bell model." *Proc. Natl. Acad. Sci. USA.* **98**:950-55.

Chen, S., R. Alon, R. C. Fuhlbrigge, and T. A. Springer. (1997) "Rolling and transient tethering of leukocytes on antibodies reveal specializations of selectins." *Proc. Natl. Acad. Sci. USA.* **94**:3172-3177.

Chen, C., and Okayama, H. (1987) "High-efficiency transformation of mammalian cells by plasmid DNA." *Mol. Cell. Biol.* **7:** 2745-2752.

Chesla, S. E., P. Li, S. Nagarajan, P. Selvaraj, and C. Zhu. (2000) "The membrane anchor influences ligand binding two-dimensional kinetic rates and three-dimensional affinity of FcγRIII (CD16)." *J. Biol. Chem.* **275**:10235-10246.

Chesla, S. E., P. Selvaraj, and C. Zhu. (1998) "Measuring two-dimensional receptor-ligand binding kinetics with micropipette." *Biophys. J.* **75**:1553-1572.

Cozens-Roberts, C., D. A. Lauffenburger, and J. A. Quinn. (1990) "Receptor-mediated cell attachment and detachment kinetics. I. Probabilistic model and analysis." *Biophys. J.* **58:**841-856.

Delobel, J. (1992) Quantification of the adhesion force between individual promyelocytic cells and Kaposi's sarcoma cells using a micropipette technique. M.S. thesis. Georgia Institute of Technology, Atlanta.

de Haas, M., Koene, H. R., Kleijer, M., de Vries, E., Simsek, S., van Tol, M. J., Roos, D., and von dem Borne, A. E. (1996) "A triallelic Fc gamma receptor type IIIA polymorphism influences the binding of human IgG by NK cell Fc gamma RIIIa." *J. Immunol.* **156**: 3948-3955.

Dustin, M. L., Selvaraj, P., Mattaliano, R. J., and Springer, T. A. (1987) "Anchoring mechanisms for LFA-3 cell adhesion glycoprotein at membrane surface." *Nature* **329**: 846-848.

Dustin, M. L., Bromley, S. K., Davis, M. M., and Zhu, C. (2001) "Identification of self through two-dimensional chemistry and synapses." *Annu. Rev. Cell Dev. Biol.* **17**: 133-157.

Dustin, M. L., L. M. Ferguson, P.-Y. Chan, T. A. Springer, and D. E. Golan. (1996) Visualization of CD2 interaction with LFA-3 and determination of the two-dimensional dissociation constant for adhesion receptors in a contact area. *J. Cell Biol.* **132**:465-474.

Dwir, O., Kansas, G. S., and Alon, R. (2000) "An Activated L-selectin Mutant with Conserved Equilibrium Binding Properties but Enhanced Ligand Recognition under Shear Flow." *J. Biol. Chem.* **275**: 18682–18691.

Edberg, J. C., Redecha, P. B., Salmon, J. E., and Kimberly, R. P. (1989) "Human Fc gamma RIII (CD16). Isoforms with distinct allelic expression, extracellular domains, and membrane linkages on polymorphonuclear and natural killer cells" *J. Immunol.* **143:** 1642-1649.

Edberg, J. C., and Kimberly, R. P. (1997) "Cell type-specific glycoforms of Fc gamma RIIIa (CD16): differential ligand binding" *J. Immunol.* **159**, 3849-3857.

Edberg, J. C., Redecha, P. B., Salmon, J. E., and Kimberly, R. P. (1989) "Human Fc gamma RIII (CD16). Isoforms with distinct allelic expression, extracellular domains, and membrane linkages on polymorphonuclear and natural killer cells" *J. Immunol.* **143,** 1642-1649.

Erbe, D. V., Wolitzky, B. A., Presta, L. G., Norton, C. R., Ramos, R. J., Burns, D. K., Rumberger, J. M., Rao, B. N. N., Foxall, C., Brandley, B. K., and Lasky, L. A. (1992) "Identification of an E-selectin region critical for carbohydrate recognition and cell adhesion" *J. Cell Biol.* **119**: 215–227.

Ernst, L. K., Duchemin, A.-M., and Anderson, C. L. (1993) "Association of the high-affinity receptor for IgG (Fc gamma RI) with the gamma subunit of the IgE receptor." *Proc. Natl. Acad. Sci. U. S. A.* **90:** 6023-6027.

Evans, E. (2001) "Probing the relation between force--lifetime--and chemistry in single molecular bonds." *Annu Rev Biophys Biomol Struct.* **30**:105-28.

Evans, E., D. Berk, and A. Leung. (1991) "Detachment of agglutinin-bonded red blood cells. I. Forces to rupture molecular-point attachments." *Biophys J.* **59**:838-48.

Evans, E., and Skalak, R. (1980) Mechanics and Thermodynamics of Biomembranes, CRC Press, Boca Raton, FL.

Evans, E., and K. Ritchie. (1997) "Dynamic strength of molecular adhesion bonds." *Biophys J.* **72**:1541-55.

Evans, E., K. Ritchie, and R. Merkel. (1995) "Sensitive force technique to probe molecular adhesion and structural linkages at biological interfaces." *Biophys J.* **68**:2580-7.

Evans, E., Leung, A., and Zhelev, D. (1993) "Synchrony of cell spreading and contraction force as phagocytes engulf large pathogens." *J. Cell Biol.* **122:** 1295-1300.

Ferguson, M. A., Homans, S. W., Dwek, R. A., and Rademacher, T. W. (1988) "Glycosyl-phosphatidylinositol moiety that anchors Trypanosoma brucei variant surface glycoprotein to the membrane." *Science* **239**: 753-759.

Fleit, H. B., Kuhnle, M., and Kobasiuk, C. D. (1989) in *Leukocyte Typing* (Knapp, W. , Dorken, B. , Gilks, W. R. , Rieber, E. P. , Schmidt, R. E. , Stein, H. , and von dem Borne, A. E. G. J., eds), Vol. 4 , pp. 579-581, Oxford University Press, New York.

Florin, E. L., V. T. Moy, and H. E. Gaub. (1994) "Adhesion forces between individual ligand-receptor pairs." *Science.* **264**:415-7.

Fraker, P. J., and Speck, J. C. (1978) "Protein and cell membrane iodinations with a sparingly soluble chloroamide, 1,3,4,6-tetrachloro-3a,6a-diphrenylglycoluril." *Biochem. Biophys. Res. Commun.* **80:** 849-857.

Gazit, A., Yaish, P., Gilon, C., and Levitzki, A. (1989) “Tyrphostins I: synthesis and biological activity of protein tyrosine kinase inhibitors.” *Am. Chem. Soc.* **32:** 2344-2352.

Gergely, J., Sarmay, G., Rozsnyay, Z., Stanworth, D. R., and Klein, E. (1986) “Binding characteristics and isotype specificity of Fc receptors on K cells.” *Mol. Immunol.* **23:** 1203-1209.

Ghirlando, R., M. B. Keown, G. A. Mackay, M. S. Lewis, J. C. Unkeless, and H. J. Gould. (1995) “Stoichiometry and thermodynamics of the interaction between the Fc fragment of human IgG1 and its low-affinity receptor FcγRIV” *Biochem.* 34:13320-13327.

Gold, E. R., and H. H. Fudenberg. (1967) “Chromic chloride: a coupling reagent for passive hemagglutination reactions.” *J. Immunol.* **99**:859-866.

Greenburg, S., Chang, P., and Silverstein, S. C. (1993) “Tyrosine phosphorylation is required for Fc receptor-mediated phagocytosis in mouse macrophages” *J. Exp. Med.* **177,** 529-534.

Greenberg, S., Chang, P., and Silverstein, S. C. (1994) “Tyrosine phosphorylation of the gamma subunit of Fc gamma receptors, p72syk, and paxillin during Fc receptor-mediated phagocytosis in macrophages.” *J. Biol. Chem.* **269:** 3897-3902.

Grubmüller, H., B. Heymann, and P. Tavan. (1996) “Ligand binding : molecular mechanics calculation of the streptavidin-biotin rupture forces.” *Science.* **271**:997-999.

Hammer, D. A., and S. M. Apte. (1992) “Simulation of cell rolling and adhesion on surfaces in shear flow: general results and analysis of selectin-mediated neutrophil adhesion.” *Biophys J.* **63**:35-57.

Hasslen, S. R., A. R. Burns, S. I. Simon, C. W. Smith, K. Starr, A. N. Barclay, S. A. Michie, R. D. Nelson, and S. L. Erlandsen. (1996) “Preservation of spatial organization and antigenicity of leukocyte surface molecules by aldehyde fixation: flow cytometry and high-resolution FESEM studies of CD62L, CD11b, and Thy-1.” *J Histochem Cytochem.* **44**:1115-1122.

He, H. T., Finne, J., and Goridis, C. (1987) “Biosynthesis, membrane association, and release of N-CAM-120, a phosphatidylinositol-linked form of the neural cell adhesion molecule.” *J. Cell Biol.* **105**: 2489-2500.

Hinterdorfer, P., W. Baumgartner, H. Gruber, K. Schilcher, and H. Schindler (1996) “Detection and localization of individual antibody-antigen recognition events by atomic force microscopy.” *Proc. Natl. Acad. Sci. USA.* **93**:3477-3481.

Hochmuth, R. M. (1987) Properties of red blood cells. *In* Handbook of Bioengineering. R. Skalak, and S. Chien, editors. McGraw-Hill, New York.

Horovitz, A., and Levitzki, A. (1987) “An accurate method for determination of receptor-ligand and enzyme-inhibitor dissociation constants from displacement curves.” *Proc. Natl. Acad. Sci. U. S. A.* **84**: 6654-6658.

Huizinga, T. W. J., Kerst, M., Nuyens, J. H., Vlug, A., Von dem Borne, A. E. G. K., Roos, D., and Tetteroo, P. A. T. (1989) “Binding characteristics of dimeric IgG subclass complexes to human neutrophils” *J. Immunol.* **142:** 2359-2364.

Huizinga, T. W. J., Dolman, K. M., van Der Linden, N. M. J., Kleijer, M., Nuijens, J. H., Von dem Borne, A. E. G. K., and Roos, D. (1990) “Phosphatidylinositol-linked FcRIII mediates exocytosis of neutrophil granule proteins, but does not mediate initiation of the respiratory burst“ *J. Immunol.* **144:** 1432-1437.

Hulett, M. D., and P. M. Hogarth. (1994) “Molecular basis of Fc receptor function.” *Adv. Immunol.* **57**:1-127.

Hynes, R. O. (2002) “Integrins: Bidirectional, Allosteric Signaling Machines” *Cell* **110**, 673–687.

Indik, Z. K., Hunter, S., Huang, M. M., Pan, X. Q., Chein, P., Kelly, C., Levinson, A. L., Kimberly, R. B., and Schreiber, A. D. (1994) “The high affinity Fc gamma receptor (CD64) induces phagocytosis in the absence of its cytoplasmic domain: the gamma subunit of Fc gamma RIIIA imparts phagocytic function to Fc gamma RI.” *Exp. Hematol.* **22:** 599-606.

Izrailev, S., S. Stepaniants, M. Balsera, Y. Oono, and K. Schulten. (1997) “Molecular dynamics study of unbinding of the avidin-biotin complex.” *Biophys. J.* **72:**1568-1581.

Jungi, T. W. (1985) “A rapid and sensitive method allowing photometric determination of erythrophagocytosis by mononuclear phagocytes.” *J. Immunol. Methods* **82:** 141-153.

Kaplanski, G., C. Farnarier, O. Tissot, A. Pierres, A.-M. Benoliel, M.-C. Alessi, S. Kaplanski, and P. Bongrad. (1993) “Granulocyte-endothelium initial adhesion. Analysis of transient binding events mediated by E-selectin in a laminar shear flow.” *Biophys. J.* **64:**1922-1933.

Kimberly, R. P., Ahlstrom, J. W., Click, M. E., and Edberg, J. C. (1990) “The glycosyl phosphatidylinositol-linked Fc gamma RIIIPMN mediates transmembrane signaling events distinct from Fc gamma RII.” *J. Exp. Med.* **171:** 1239-1255.

King, M. R., and D. A. Hammer. (2001) “Multiparticle adhesive dynamics. Interactions between stably rolling cells.” *Biophys J.* **81**:799-813.

Klaassen, R. J., Ouwehand, W. H., Huizinga, T. W., Engelfriet, C. P., and von dem Borne, A. E. (1990) “The Fc-receptor III of cultured human monocytes. Structural similarity with FcRIII of natural killer cells and role in the extracellular lysis of sensitized erythrocytes” *J. Immunol.* **144:** 599-606.

Klausner, R. D., and Sitia, R. (1990) “Protein degradation in the endoplasmic reticulum.” *Cell* **62**: 611-614.

Kofler, R., and Wick, G. (1977) “Some methodologic aspects of the chromium chloride method for coupling antigen to erythrocytes.” *J. Immunol. Methods* **16**: 201–209.

Kuo, S. C., D. A. Hammer, and D. A. Lauffenburger. (1997) “Simulation of detachment of specifically bound particles from surfaces by shear flow.” *Biophys J.* **73:** 517-31.

Kukulansky, T., Abramovitch, S., and Hollander, N. (1999) “Cleavage of the Glycosylphosphatidylinositol Anchor Affects the Reactivity of Thy-1 with Antibodies**”** *J. Immunol.* **162**: 5993-5997.

Kurosaki, T., and Ravetch, J. V. (1989) “A single amino acid in the glycosyl phosphatidylinositol attachment domain determines the membrane topology of Fc gamma RIII.” *Nature* **342**: 805-807.

Kwong, D., D. F. J. Tees, and H. L. Goldsmith. (1996) “Kinetics and locus of failure of receptor-ligand-mediated adhesion between latex spheres. II. Protein-protein bond” *Biophys. J.* **71**:1115-1122.

Lanier, L. L., Yu, G., and Phillips, J. H. (1990) “Analysis of Fc gamma RIII (CD16) membrane expression and association with CD3 zeta and Fc epsilon RI-gamma by site-directed mutation.” *J. Immunol.* **146**: 1571-1576.

Lanier, L. L., Phillips, J. H., and Testi, R. (1989) “Membrane anchoring and spontaneous release of CD16 (FcR III) by natural killer cells and granulocytes.” *Eur. J. Immunol.* **19:** 775-778.

Lanier, L. L., Ruitenberg, J. J., and Phillips, J. H. (1988) ”Functional and biochemical analysis of CD16 antigen on natural killer cells and granulocytes**”** *J. Immunol.* **141:** 3478-3485.

Laurenzi, I. J., and S. L. Diamond. (1999) “Monte Carlo simulation of the heterotypic aggregation kinetics of platelets and neutrophils.” *Biophys J.* **77**:1733-46.

Lawrence, M. B., and T. A. Springer. (1991) "Leukocytes roll on a selectin at physiological flow rates: distinction from and prerequisite for adhesion through integrins." *Cell.* **65**:859-873.

Le Bouteiller, P. P., Mishal, Z., Lemonnier, F. A., and Kourilsky, F. M. (1983) "Quantification by flow cytofluorimetry of HLA class I molecules at the surface of murine cells transformed by cloned HLA" *J. Immunol. Methods* **61**: 301-315.

Leckband, D. E., F. J. Schmitt, J. N. Israelachvili, and W. Knoll. (1994) "Direct force measurements of specific and nonspecific protein interactions." *Biochemistry.* **33**:4611-4624.

Lee, G. U., D. A. Kidwell, and C. R. J. (1994) "Sensing discrete streptavidin-biotin interactions with atomic force microscopy." *Langmuir.* 10:354-357.

Lennartz, M. R., Lefkowith, J. B., Bromley, F. A., and Brown, E. J. (1993) "Immunoglobulin G-mediated phagocytosis activates a calcium-independent, phosphatidylethanolamine-specific phospholipase" *J. Leukocyte Biol.* **54:** 389-398.

Li, S. H., Burns, D. K., Rumberger, J. M., Presky, D. H., Wilkinson, V. L., Anostario, Jr. M., Wolitzky, B. A., Norton, C. R., Familletti, P. C., Kim, K. J., Goldstein, A.L., Cox, D. C., and Huang, K. S. (1994) "Consensus repeat domains of E-selectin enhance ligand binding" *J. Biol. Chem.* **269**: 4431-4437.

Lin, C. T., Shen, Z., Boros, P., and Unkeless, J. C. (1994) "Fc receptor-mediated signal transduction." *J. Clin. Immunol.* **14,** 1-13.

Long, M., H. L. Goldsmith, D. F. Tees, and C. Zhu.(1999) "Probabilistic modeling of shear-induced formation and breakage of doublets cross-linked by receptor-ligand bonds." *Biophys J.* **76**:1112-28.

Long, M., H. Zhao, K.-S. Huang, and C. Zhu. (2001) "Kinetic measurements of cell surface E-selectin/carbohydrate ligand interactions." *Annals Biomedical Engineering*. **29**(11):935-46.

Low, M. G. (1987) "Biochemistry of the glycosyl-phosphatidylinositol membrane protein anchors." *Biochem. J.* **244:** 1-13.

Lyles, M., Norrild, B., and Bock, E. (1984) "Biosynthesis of the D2 cell adhesion molecule: pulse-chase studies in cultured fetal rat neuronal cells." *J. Cell Biol.* **98**, 2077-2081.

Masuda, M., and Roos, D. (1993) "Association of all three types of Fc gamma R (CD64, CD32, and CD16) with a gamma-chain homodimer in cultured human monocytes" *J. Immunol.* **151:** 7188-7195.

McQuarrie, D. A. (1963) "Kinetics of small systems. I." *J. Chem. Phys.* **38**:433-436.

McEver, R.P. (2001) "Adhesive interactions of leukocytes, platelets, and the vessel wall during hemostasis and inflammation." *Thromb. Haemost.* **86:** 746-756.

McEver, R.P. (2002) "Selectins: lectins that initiate cell adhesion under flow." *Curr. Opin. Cell Biol.* **14:** 581-586.

Mehta, P., Cummings, R. D., and McEver, R. P. (1998) "Affinity and kinetic analysis of P-selectin binding to P-selectin glycoprotein ligand-1." *J. Biol. Chem.* **273**: 32506-32513.

Mehta, P., Patel, K. D., Laue, T. M., Erickson, H. P., and McEver, R. P. (1997) "Soluble monomeric P-selectin containing only the lectin and epidermal growth factor domains binds to P-selectin glycoprotein ligand-1 on leukocytes." *Blood* **90**: 2381-2389.

Merkel, R., P. Nassoy, A. Leung, K. Ritchie, and E. Evans. (1999) "Energy landscapes of receptor-ligand bonds explored with dynamic force spectroscopy." *Nature.* **397:**50-53.

Michael, K.E., Vernakar, V. N., Keselowsky, B. G., Meredith, J. C., Latour, R. A., and arcía, A. J. (2003) *Langmuir* **19:** 8033-8040.

Miller, K. L., Duchemin, A. M., and Anderson, C. L. (1996) "A novel role for the Fc receptor gamma subunit: enhancement of Fc gamma R ligand affinity." *J. Exp. Med.* **183**: 2227-2233.

Miyata, H., R. Yasuda, and K. Kinosita. (1996) "Strength and lifetime fo bonds between actin and skeletal muscle alpha-actinin studied with an optical trapping technique." *Biochim. Biophys. Acta.* **1290**: 83-88.

Moore, K. L., Patel, K. D., Bruehl, R. E., Li, F., Johnson, D. A., Lichenstein, H. S., Cummings, R. D., Bainton, D. F., and McEver, R. P. (1995) "P-selectin glycoprotein ligand-1 mediates rolling of human neutrophils on P-selectin." *J. Cell Biol.* **128:** 661-671.

Moy, P., Lobb, R., Tizard, R., Olson, D., and Hession, C. (1993) "Cloning of an inflammation-specific phosphatidyl inositol-linked form of murine vascular cell adhesion molecule-1." *J. Biol. Chem.* **268**: 8835-8841.

Nagarajan, S., Chesla, S. E., Cobern, L., Anderson, P., Zhu, C., and Selvaraj, P. (1995) "Ligand binding and phagocytosis by CD16 (Fc gamma receptor III) isoforms. Phagocytic signaling by associated zeta and gamma subunits in Chinese hamster ovary cells." *J. Biol. Chem.* **270:** 1-9.

Naziruddin, B., Duffy, B., Tucker, J., and Mohankumar, T. (1992) “Evidence for cross-regulation of Fc gamma RIIIB (CD16) receptor- mediated signaling by Fc gamma RII (CD32) expressed on polymorphonuclear neutrophils**”** *J. Immunol.* **149,** 3702-3709

Nishikiori, N., Koyama, M., Kikuchi, T., Kimura, T., Ozaki, M., Harada, S., Saji, F., and Tanizawa, O. (1993) *Am. J. Reprod. Immunol.* **29,** 17-25

Odin, J. A., Edberg, J. C., Painter, C. J., Kimberly, R. P., and Unkeless, J. C. (1991) “Regulation of phagocytosis and [Ca2+]i flux by distinct regions of an Fc receptor.” *Science* **254,** 1785-1788

O'Shea, J. J., Weissman, A. M., Kennedy, I. C. S., and Ortaldo, J. R. (1991) “Engagement of the natural killer cell IgG Fc receptor results in tyrosine phosphorylation of the zeta chain.” *Proc. Natl. Acad. Sci. U. S. A.* **88,** 350-354.

Park, J. G., Murray, R. K., Chien, P., Darby, C., and Schreiber, A. D. (1993) “Conserved cytoplasmic tyrosine residues of the gamma subunit are required for a phagocytic signal mediated by Fc gamma RIIIA.” *J. Clin. Invest.* **92,** 2073-2079

Patel, K. D., Nollert, M. U., and McEver, R. P. (1995) “P-selectin must extend a sufficient length from the plasma membrane to mediate rolling of neutrophils.” *J. Cell Biol.* **131**,1893-1902

Patel, K. D., Moore, K. L., Nollert, M. U., and McEver, R. P. (1995) “Neutrophils use both shared and distinct mechanisms to adhere to selectins under static and flow conditions.” *J Clin Invest.* **96:** 1887-1896.

Perussia, B., Cassatella, M. A., Anegon, I., and Trinchieri, G. (1989) in *Leukocyte Typing* (Knapp, W. , Dorken, B. , Gilks, W. R. , Rieber, E. P. , Schmidt, R. E. , Stein, H. , and von dem Borne, A. E. G. J., eds), Vol. 4 , pp. 590-595, Oxford University Press, New York

Perussia, B., and Ravetch, J. V. (1991) “Fc gamma RIII (CD16) on human macrophages is a functional product of the Fc gamma RIII-2 gene.” *Eur. J. Immunol.* **21:** 425-429.

Pierres, A., A. M. Benoliel, and P. Bongrand. (1995) “Measuring the lifetime of bonds made between surface-linked molecules.” *J Biol Chem.* **270:** 26586-92.

Pierres, A., A.-M. Benoliel, and P. Bongrand. (1994) “Initial steps of cell-substrate adhesion. *In* Cell mechanics and cellular engineering.” V. C. Mow, F. Guilak, R. Tran-Son-Tay, and R. M. Hochmuth, editors. Springer Verlag, New York. 145-159.

Pierres, A., O. Tissot, and P. Bongrand. (1994) “Analysis of the motion of cells driven along an adhesive surface by a laminar shear flow.” *In* Studying Cell Adhesion. P. Bongrand, P. Claesson, and A. Curtis, editors. Springer Verlag, Heidelberg. 157-174.

Piper, J. W., R. A. Swerlick, and C. Zhu. (1998) “Determining force dependence of two-dimensional receptor-ligand binding affinity by centrifugation.” *Biophys. J.* **74**:492-513.

Piper, J. W. (1997) “Force dependence of cell bound E-selectin/carbohydrate ligand binding characteristics.” Ph.D. thesis. Georgia Institute of Technology, Atlanta.

Poo, H., Krauss, J. C., Mayo-Bond, L., Todd, R. F. I., and Petty, H. R. (1995) “Interaction of Fc gamma receptor type IIIB with complement receptor type 3 in fibroblast transfectants: evidence from lateral diffusion and resonance energy transfer studies.” *J. Mol. Biol.* **247**, 597-603.

Press, W. H., B. P. Flannery, S. A. Teukolsky, and W. T. Vetterling. (1989) Numerical Recipes in FORTRAN: The Art of Scientific Computing. Cambridge University Press, Cambridge, England.

Ra, C., Jouvin, M.-H. E., Blank, U., and Kinet, J. P. (1989) “A macrophage Fc gamma receptor and the mast cell receptor for IgE share an identical subunit.” *Nature* **341,** 752-754

Ramachandran, V., M. U. Nollert, H. Qiu, W. J. Liu, R. D. Cummings, C. Zhu, and R. P. McEver. (1999) “Tyrosine replacement in P-selectin glycoprotein ligand-1 affects distinct kinetic and mechanical properties of bonds with P- and L-selectin.” *Proc. Natl. Acad. Sci. USA.* **96:**13771-13776.

Ramachandran, V., T. Yago, T. K. Epperson, M. Kobzdej, M. U. Nollert, R. D. Cummings, C. Zhu, and R. P. McEver. (2001) “Dimerization of a selectin and its ligand stabilizes cell rolling and enhances tether strength in shear flow.” *Proc Natl Acad Sci U S A.* **98**:10166–10171.

Ravetch, J. V., and Perussia, B. (1989) “Alternative membrane forms of Fc gamma RIII(CD16) on human natural killer cells and neutrophils. Cell type-specific expression of two genes that differ in single nucleotide substitutions.” *J. Exp. Med.* **170**:481-497.

Ravetch, J. V., and Kinet, J.-P. (1991) “Fc receptors.” *Annu. Rev. Immunol.* **9:** 457-492.

Reissner E., (1946), *J. Math. Phys*., **25**, 274-300.

Rosales, C., and Brown, E. J. (1991) "Signal transduction by neutrophil immunoglobulin G Fc receptors. Dissociation of intracytoplasmic calcium concentration rise from inositol 1,4,5-trisphosphate." *J. Immunol.* **146:** 3937-3944.

Salmon, J. E., Brogle, N. L., Edberg, J. C., and Kimberly, R. P. (1991) "Fc gamma receptor III induces actin polymerization in human neutrophils and primes phagocytosis mediated by Fc gamma receptor II" *J. Immunol.* **146:** 997-1004.

Samelson, L. E., Patel, M. D., Weissman, A. M., Harford, J. B., and Klausner, R. D. (1986) "Antigen activation of murine T cells induces tyrosine phosphorylation of a polypeptide associated with the T cell antigen receptor." *Cell* **46:** 1083-1090.

Sanchez-Mateos, P., Cabanas, C., and Sanchez-Madrid, F. (1996) "Regulation of integrin function." *Semin. Cancer Biol.* **7**: 99-109.

Sandor, M., and Lynch, R. G. (1993) "The biology and pathology of Fc receptors." *J. Clin. Immunol.* **13:** 237-246.

Scallon, B. J., Scigliano, E., Freedman, V. H., Miedel, M. C., Pan, Y.-C. E., Unkeless, J. C., and Kochan, J. P. (1989) "A human immunoglobulin G receptor exists in both polypeptide-anchored and phosphatidylinositol-glycan-anchored forms." *Proc. Natl. Acad. Sci. U. S. A.* **86:** 5079-5083.

Scatchard, G. (1949) *Ann. N. Y. Acad. Sci.* **51**, 660–672.

Schreiber, A. D., Rossman, M. D., and Levinson, A. I. (1992) "The immunobiology of human Fc gamma receptors on hematopoietic cells and tissue macrophages." *Clin. Immunol. Immunopathol.* **62:** S66-S72.

Serke, S., van Lessen, A., and Huhn, D. (1998) "Quantitative fluorescence flow cytometry: a comparison of the three techniques for direct and indirect immunofluorescence" *Cytometry* **33:** 179-187.

Selvaraj, P., Rosse, W. F., Silber, R., and Springer, T. A. (1988) "The major Fc receptor in blood has a phosphatidylinositol anchor and is deficient in paroxysmal nocturnal haemoglobinuria" *Nature* **333:** 565-567.

Selvaraj, P., Carpen, O., Hibbs, M. L., and Springer, T. A. (1989) "Natural killer cell and granulocyte Fc gamma receptor III (CD16) differ in membrane anchor and signal transduction." *J. Immunol.* **143**: 3283-3288.

Selvaraj, P., Dustin, M. L., Silber, R., Low, M. G., and Springer, T. A. (1987) "Deficiency of lymphocyte function-associated antigen 3 (LFA-3) in paroxysmal nocturnal hemoglobinuria. Functional correlates and evidence for a phosphatidylinositol membrane anchor." *J. Exp. Med.* **166:** 1011-1025.

Selvaraj, P., Plunkett, M. L., Dustin, M., Sanders, M. E., Shaw, S., and Springer, T. A. (1987) "The T lymphocyte glycoprotein CD2 binds the cell surface ligand LFA-3." *Nature* **326:** 400-403.

Selvaraj, P., Hibbs, M. L., Carpen, O., and Springer, T. A. (1989) in *Leukocyte Typing* (Knapp, W. , Dorken, B. , Gilks, W. R. , Rieber, E. P. , Schmidt, R. E. , Stein, H. , and von dem Borne, A. E. G. J., eds), Vol. 4 , pp. 595-597, Oxford University Press, New York.

Setiadi, H., S. L. Erlandsen, and R. P. McEver. (1998) "Interactions of the cytoplasmic domain of P-selectin with clathrin-coated pits enhance neutrophil adhesion under flow." *J. Cell Biol.* **142**(3):859-71.

Shao, J. Y., and R. M. Hochmuth. (1996) "Micropipette suction for measuring piconewton forces of adhesion and tether formation from neutrophil membranes." *Biophys J.* **71**:2892-901.

Shao, J. Y., and R. M. Hochmuth. (1999) "Mechanical anchoring strength of L-selectin, beta2 integrins, and CD45 to neutrophil cytoskeleton and membrane." *Biophys J.* **77**:587-96.

Shen, L., Guyre, P. M., and Fanger, M. W. (1987) "Polymorphonuclear leukocyte function triggered through the high affinity Fc receptor for monomeric IgG." *J. Immunol.* **139:**534-538.

Shenoy-Scaria, A. M., Kwong, J., Fujita, T., Olszowy, M. W., Shaw, A. S., and Lublin, D. M. (1992) "Signal transduction through decay-accelerating factor. Interaction of glycosyl-phosphatidylinositol anchor and protein tyrosine kinases p56lck and p59fyn 1." *J Immunol.* **149:** 3535-3541.

Simmons, D., and Seed, B. (1988) "The Fcγ receptor of natural killer cells is a phospholipid-linked membrane protein"*Nature* **333:** 568-570.

Smith, M. J., E. L. Berg, and M. B. Lawrence. (1999) "A direct comparison of selectin-mediated transient, adhesive events using high temporal resolution." *Biophys. J.* **77**:3371-3383.

Spiegelberg, H. L., Perlmann, H., and Perlmann, P. (1976) "Interaction of K lymphocytes with myeloma proteins of different IgG subclasses." *J. Immunol.* **117,** 1464-1470

Springer, T. A. (1994) "Traffic signals for lymphocyte recirculation and leukocyte emigration: the multistep paradigm." *Cell* **76**, 301-314.

Stefeanova, I., Horejsi, V., Ansotegui, I. J., Knapp, W., and Stockinger, H. (1991) “GPI-anchored cell-surface molecules complexed to protein tyrosine kinases.” *Science* **254:**1016-1019.

Stefanova, I., and Horejsi, V. (1991) “Association of the CD59 and CD55 cell surface glycoproteins with other membrane molecules.” *J. Immunol.* **147:**1587-1592.

Sung, K.-L. P., L. A. Sung, M. Crimmins, S. J. Burakoff, and S. Chien. (1986) “Determination of junction avidity of cytolytic T cell and target cell.” *Science.* 234:1405-1408.

Takagi, J., Strokovich, K., Springer, T. A., and Walz, T. (2003) “Structure of integrin alpha5beta1 in complex with fibronectin.” *EMBO J.* **22:**4607-4615.

Takai, T., Li, M., Sylvestre, D., Clynes, R., and Ravetch, J. V. (1994) “FcR gamma chain deletion results in pleiotrophic effector cell defects.” *Cell* **76:**519-529.

Tamm, A., Kister, A., Nolte, K. U., Gessner, J. E., and Schmidt, R. E. (1996) “The IgG binding site of human FcgammaRIIIB receptor involves CC' and FG loops of the membrane-proximal domain.” *J. Biol. Chem.* **271:** 3659-3666.

Tamm, A., and Schmidt, R. E. (1996) “The binding epitopes of human CD16 (Fc gamma RIII) monoclonal antibodies. Implications for ligand binding” *J. Immunol.* **157:**1576-1581.

Tees, D. F., O. Coenen, and H. L. Goldsmith. (1993) “Interaction forces between red cells agglutinated by antibody. IV. Time and force dependence of break-up.” *Biophys J.* **65**:1318-34.

Tees, D.F.J., and H.L. Goldsmith**.** (1996) “Kinetics and locus of failure of receptor-ligand-mediated adhesion between latex spheres. I. Protein carbohydrate bond.” *Biophs. J.* **71**, 102-1114.

Tees, D. F. J., R. E. Waugh, and D. A. Hammer. “A microcantilever device to assess the effect of force on the lifetime of selectin-carbohydrate bonds.” (2001) *Biophys J.* **80**:668–682.

Terry, R. W., Kwee, L., Levine, J. F., and Labow, M. A. (1993) “Cytokine induction of an alternatively spliced murine vascular cell adhesion molecule (VCAM) mRNA encoding a glycosylphosphatidylinositol-anchored VCAM protein.” *Proc. Natl. Acad. Sci. U. S. A.* **90**:5919-5923.

Tha, S. P., J. Shuster, and H. L. Goldsmith. (1986) “Interaction forces between red cells agglutinated by antibody. II. Measurement of hydrodynamic force of breakup.” *Biophys J.* **50:**1117-26.

Thoumine, O., P. Kocian, A. Kottelat, and J. J. Meister. (2000) "Short-term binding of fibroblasts to fibronectin: optical tweezers experiments and probabilistic analysis." *Eur Biophys J.* **29:**398-408.

Tözeren, A., Sung, K. L., Sung, L. A., Dustin, M. L., Chan, P. Y., Springer, T. A., and Chien, S. (1992) "Micromanipulation of adhesion of a Jurkat cell to a planar bilayer membrane containing lymphocyte function-associated antigen 3 molecules." *J. Cell Biol.* **116:** 997-1006.

Tuijnman, W. B., Wijngaard, P. L. J., Van Wichen, D., Van de Winkel, J. G. J., Capel, P. J. A., and Schuurman, H.-J. (1992) "Presence of CD16 on endothelial cells in heart transplant rejection: an immunohistochemical study." *Scand. J. Immunol.* **35:** 569-573.

Ueda, E., Kinoshita, T., Nojima, J., Inoue, K., and Kitani, T. (1989) "Different membrane anchors of Fc gamma RIII (CD16) on K/NK-lymphocytes and neutrophils. Protein- vs lipid-anchor." *J. Immunol.* **143:** 1274-1277.

Unanue, E. R. (1984) "Antigen-presenting function of the macrophage." *Annu. Rev. Immunol.* **2**:395-428.

Ushiyama, S., Laue, T. M., Moore, K. L., Erickon, H. P., and McEver, R. P. (1993) "Structural and functional characterization of monomeric soluble P-selectin and comparison with membrane P-selectin." *J. Biol. Chem.* **268**: 15229–15237.

Vance, B. A., Huizinga, T. W., Wardwell, K., and Guyre, P. M. (1993) "Binding of monomeric human IgG defines an expression polymorphism of Fc gamma RIII on large granular lymphocyte/natural killer cells." *J. Immunol.* **151**, 6429-6439

van de Winkel, J. G. J., and Capel, P. J. A. (eds) (1996) *Human IgG Fc Receptors* , R. G. Landes, Austin, TX

van de Winkel, J. G., and Capel, P. J. (1993) "Human IgG Fc receptor heterogeneity: molecular aspects and clinical implications." *Immunol. Today.* **14**, 215–221

van Kooyk, Y., P. Weder, K. Heije, and C. G. Figdor.(1994) "Extracellular calcium modulates leukocyte function-associated antigen-1 cell surface distribution on T lymphocytes and consequently affects cell adhesion." *J. Cell Biol.* **124**:1061–1070.

Vestweber, D., and Blanks, J. E. (1999) "Mechanisms that regulate the function of the selectins and their ligands." *Physiol. Rev.* **79:** 181-213.

Vijayendran, R., D. Hammer, and D. Leckband. (1998) "Simulations of the adhesion between molecularly bonded surfaces in direct force measurements." *J. Chem. Phys.* **108:**7783–7793.

Vivier, E., Morin, P., O'Brien, C., Drunker, B., Schlossman, S. F., and Anderson, P. (1991) ' Tyrosine phosphorylation of the Fc gamma RIII(CD16): zeta complex in human natural killer cells. Induction by antibody-dependent cytotoxicity but not by natural killing." *J. Immunol.* **146:** 206-210.

Vivier, E., Rochet, N., Kochan, J. P., Presky, D. H., Schlossman, S. F., and Anderson, P. (1991) "Structural similarity between Fc receptors and T cell receptors. Expression of the gamma-subunit of Fc epsilon RI in human T cells, natural killer cells and thymocytes." *J. Immunol.* **147:** 4263-4270.

Vivier, E., Rochet, N., Ackerly, M., Petrini, J., Levine, H., Daley, J., and Anderson, P. (1992) "Signaling function of reconstituted CD16: zeta: gamma receptor complex isoforms." *Int. Immunol.* **4:**1313-1323.

von Andrian, U. H., S. R. Hasslen, R. D. Nelson, S. L. Erlandsen, and E. C. Butcher. (1995) "A central role for microvillous receptor presentation in leukocyte adhesion under flow." *Cell* **82:**989–999.

Werner, G., Von dem Borne, A. E. G., Bos, M. J. E., Tromp, J. E., van der Plas-van Dalen, C. M., Visser, F. J., Engelfriet, C. P., and Tetteroo, P. A. T. (1986) in *Leukocyte Typing II* (Reinherz, E. L., Haynes, B. F., Nadler, L. M., and Bernstein, I. D., eds) 109-121, Springer-Verlag, New York

Williams, J. M., T. Han, and T. P. J. Beebe. (1996) "Determination of single-bond forces from contact force variances in atomic force microscopy." *Langmuir.* **12**:1291-1295.

Williams, T. E., S. Nagarajan, P. Selvaraj, and C. Zhu. (2000) "Concurrent binding to multiple receptors: Kinetic rates of CD16b and CD32a for IgG." *Biophys. J.* **79**:1867-1875.

Williams, T. E., S. Nagarajan, P. Selvaraj, and C. Zhu. (2001) "Quantifying the impact of membrane microtopology on effective two- dimensional affinity." *J Biol Chem.* **276**:13283-13288.

Williams, T. E., and C. Zhu. (2000) "Concurrent binding to multiple ligands: Kinetic rates of CD16b for membrane-bound IgG1 and IgG2." *Biophys. J.* **79**:1858-1866.

Winkel, J. G. J. N. D., and Anderson, C. L. (1991) "Biology of human immunoglobulin G Fc receptors." *J. Leukocyte Biol.* **49:** 511-524.

Wirthmueller, U., Kurosaki, T., Murakami, M. S., and Ravetch, J. V. (1992) "Signal transduction by Fc gamma RIII (CD16) is mediated through the gamma chain." *J. Exp. Med.* **175:** 1381-1390.

Wright, D. A. (1997) "The adherence of tumor cells to endothelial cells and of neutrophils to IgG, under flow." M.S. thesis. Georgia Institute of Technology, Atlanta.

Wong, J. Y., Kuhl, T. L., Israelachvili, J. N., Mullah, N., and Zalipsky, S. (1997) "Direct measurement of a tethered ligand-receptor interaction potential" *Science* **275**: 820-822.

Wu, J., Edberg, J. C., Redecha, P. B., Bansal, V., Guyre, P. M., Coleman, K., Salmon, J. E., and Kimberly, R. P. (1997) "A novel polymorphism of FcgammaRIIIa (CD16) alters receptor function and predisposes to autoimmune disease." *J. Clin. Invest.* **100:** 1059-1070.

Yago, T., Leppänen, A., Qiu,H. Y. , Marcus, W. D., Nollert, M. U., Zhu, C., Cummings, R. D., and McEver, R. P. (2002) "Distinct molecular and cellular contributions to stabilizing selectin-mediated rolling under flow." *J. Cell Biol.* **158**: 787–799.

Yap, A. S., W. M. Brieher, M. Priushy, and B. M. Gumbiner. (1997) "Lateral clustering of the adhesive ectodomain: a fundamental determinant of cadherin function." *Curr. Biol.* **7**:308–315.

Yeung, A., (1994) Ph.D. Thesis, Department of Physics, University of British Columbia.

Zhang, F., Crise, B., Su, B., Hou, Y., Rose, J. K., Bothwell, A., and Jacobson, K. (1991) "Lateral diffusion of membrane-spanning and glycosylphosphatidylinositol-linked proteins: toward establishing rules governing the lateral mobility of membrane proteins." *J. Cell Biol.* **115:** 75-84.

Zhou, M. J., Poo, H., Todd, R. F., III, and Petty, H. R. (1992) "Surface-bound immune complexes trigger transmembrane proximity between complement receptor type 3 and the neutrophil's cortical microfilaments." *J. Immunol.* **148:** 3550-3553.

Zhou, M., and Brown, E. J. (1994) " Distinct tyrosine kinase activation and Triton X-100 insolubility upon Fc gamma RII or Fc gamma RIIIB ligation in human polymorphonuclear leukocytes. Implications for immune complex activation of the respiratory burst." *J. Cell Biol.* **125:** 1407-1416.

Zhu, C., G. Bao, and N. Wang. (2000) "Cell mechanics: Mechanical response, cell adhesion, and molecular deformation." *Annu. Rev. Biomed. Eng.* **2**:189-226.

Zhu, C., and Williams, T. E. (2000) "Modeling concurrent binding of multiple molecular species in cell adhesion." *Biophys. J.* **79:** 1850-1857.

Zhu, C., and S. E. Chesla. (1997) "Dissociation of individual molecular bonds under force." Advances in Bioengineering, B.E.D. **36**:177-178.

Zhu, C., J. W. Piper, and R. A. Swerlick. (1998) "A centrifugation method for measurement of two-dimensional binding characteristics of receptor-ligand interaction." *In* Bioadhesion in Drug Delivery: Issues in Fundamentals, Novel Approaches, and Development. E. Mathiowitz, C. M. Lehr, and D. Chickering, editors. Marcel Dekker, New York.

Zhu, C., Williams, T. E., Delobel, J., and Offermann, M. K. (1994) in *Cell Mechanics and Cellular Engineering* (Mow, V. C., Guilak, F., Tran-Son-Tay, R., and Hochmuth, R., eds) 160-181, Springer-Verlag, New York

VITA

Scott E. Chesla was born October 7, 1964 in Evansville, Indiana to Edward and Irene Chesla. He graduated from high school in Jacksonville, North Carolina in 1982. He received a BA in Mechanical Engineering from North Carolina State University in 1987. Upon graduation he began work for Pratt & Whitney as a propulsion systems engineer. During his five years there his major assignments were a thrust upgrade to one of the oldest Naval turbojet models and lead analysis engineer for an advanced expander cycle rocket intended for a Mars mission under contract with NASA. In this time he also earned an MS in mechanical engineering from the University of Florida. He entered graduate school at Georgia Tech in 1992. In 1998 he began work at Immucor, Inc in the Research and Development department. His major assignments were an Internet based antibody identification and resolution program intended for blood banks and a 96 well test assay platform allowing for selected cell testing antibody resolution in the blood bank.